

A MULTIRESOLUTION RESTORATION METHOD FOR CARDIAC SPECT

By

JUAN M. FRANQUIZ

A DISSERTATION PRESENTED TO THE GRADUATE SCHOOL OF THE UNIVERSITY OF
FLORIDA IN PARTIAL FULFILLMENT OF THE REQUIREMENTS FOR THE DEGREE OF
DOCTOR OF PHILOSOPHY

UNIVERSITY OF FLORIDA

1997

ACKNOWLEDGMENTS

The author expresses special thanks to Dr. Mario Ariet for his support and for providing access to the computer facilities at the Division of Computer Sciences of the College of Medicine, University of Florida, for this research work. The author also thanks Mr. Stefan Lupkiewicz for providing technical help in installing and using part of the software employed in this research.

The author is grateful to his academic advisor, Dr. Shailendra Shukla, for the support, criticisms, technical advice and assistance offered throughout this research. The author also would like to express his gratitude to the staff of the Department of Nuclear Medicine at the Veterans Administration Medical Center in Gainesville, for supporting the experimental part and providing access to their nuclear instruments and radioactive sources. The author is specially grateful to Dr. Michael Fagein for his comments and Mr. Morris Thompson for preparing the radioactive sources used in this research and his general help in the experimental work.

The author thanks Dr. Nils Diaz and Dr. David Hintenlang for their support in the beginning of the graduate course work at the University of Florida. The author also thanks Dr. Andrew Laine of the Department of Computer and Information Science and Engineering for his initial comments and revision of the proposal of this research and for providing part of the software used in this work. Finally, the author wishes to thank

supervisory committee members Dr. Wesley Bolch, Dr. Walter Drane, Dr. Janice Honeymann and Dr. William Properzio for their assistance and the time dedicated to the revision, comments, criticisms and recommendations throughout this research.

TABLE OF CONTENTS

	Page
ACKNOWLEDGMENTS	ii
LIST OF TABLES	vi
LIST OF FIGURES	viii
ABSTRACT	xi
CHAPTERS	
1 INTRODUCTION	1
The Problem	3
Hypothesis and Objectives	8
Content of Chapters	9
2 CARDIAC SPECT	11
Radiopharmaceuticals	11
SPECT Data Acquisition	14
SPECT Reconstruction	19
Myocardial Tomographic Slices	25
Degrading Factors in SPECT	28
Artifacts in the Inferior Myocardial Wall	45
3 THE RESTORATION PROBLEM IN SPECT	48
Degradation Models in SPECT	49
Restoration Filters	64
Computer Implementation of the Metz Filter	72
4 MULTIRESOLUTION RESTORATION ALGORITHM	87
Wavelet Multiresolution Representation	89
Multiresolution Restoration	99
5 RESTORATION IN A REALISTIC CARDIAC CHEST PHANTOM	111
Material and Methods	112
Results and Discussion	119
Conclusions	156

6 CONCLUSIONS AND FUTURE WORK	159
Other Potential Applications	161
Future Developments	163
APPENDIXES	
A COMPUTER IMPLEMENTATION OF A METZ FILTER	170
A1 Calculation of MTF Parameters	170
A2 Simulation of a Cardiac-Liver Projection	175
A3 Metz Filtering	177
B MULTIRESOLUTION DECOMPOSITION AND RESTORATION ALGORITHM	179
B1 Multiresolution Decomposition	179
B2 Multiresolution Restoration	181
C MULTIRESOLUTION RESTORATION OF SPECT PROJECTIONS	184
C1 Restoration of SPECT Projections	184
C2 Analysis Programs	187
REFERENCES	192
BIOGRAPHICAL SKETCH	202

LIST OF TABLES

Table	Page
2.1 Contribution of out-of-plane scattered photons per voxel as a function of the activity ratio of out-of-plane to emission voxels (ROE) for different neighboring planes	42
3.1 Restoration Models in SPECT and their approximate solutions.....	53
3.2 Line spread function (LSF) and point spread function (PSF) parameters fitted to experimental data from line sources	75
3.3 Analytical expressions of fitted modulation transfer functions ..	77
3.4 Normalized mean square error (NMSE) as a function of the power factor X in image restoration using the Metz filter	83
5.1 Quantitative analysis of myocardial bull's eye polar maps	123
5.2 Quantitative analysis of a midventricular short-axis slice	125
5.3 Normalized chi-square of bull's eye polar maps as a function of the attenuation coefficient and liver-to-heart activity ratio (LHAR)	129
5.4 Uniformity of bull's eye polar maps as a function of the attenuation coefficient and liver-to-heart activity ratio (LHAR) for the cardiac-liver phantom in water	130
5.5 Normalized chi-square calculated with different reconstruction protocols as a function of the liver-to-heart activity ratio	135
5.6 Uniformity of bull's eye polar maps calculated using different reconstruction protocols	137
5.7 Quantitative analysis of a midventricular short-axis slice of the cardiac insert in water without liver activity	141
5.8 Quantitative analysis of bull's eye polar maps of the cardiac liver insert in water	142

5.9 Quantitative analysis of the effect of multiresolution restoration on the normalized chi-square of bull's eye polar maps for different liver-to-heart activity ratio (LHAR) and reconstruction protocols	143
5.10 Quantitative analysis of the effect of multiresolution restoration on uniformity of bull's eye polar maps as a function of the liver-to-heart activity ratio for different reconstruction protocols	146
5.11 Contrast of myocardial defect measured in a short-axis slice for different reconstruction protocols	148
5.12 Results of geometric calculation of true defect size on the bull's eye polar map	150
5.13 Defect size in percent of the polar map area calculated from the histogram of counts of bull's eye polar maps as a function of the threshold level	150
5.14 Threshold values for calculating defect size in cardiac SPECT.....	154
6.1 Data of the three patients included in a preliminary evaluation of the multiresolution restoration algorithm in attenuation-corrected cardiac SPECT scans	165

LIST OF FIGURES

Figure	Page
2-1 Density function $g(x,y)$ in the transaxial plane XY and its projection $P_\theta[r]$ at an angle θ	20
2-2 Filtered backprojection technique	21
2-3 SPECT reconstruction convolution kernels and their frequency response	26
2-4 Myocardial tomographic slices	27
2-5 Detection geometry of unscattered and out-of-plane scattered photons.....	38
2-6 Plot of the relative number of out-of-plane scattered photons per voxel as a function of scattering angle	41
3-1 Coordinates for source distribution and detection planeD	57
3-2 Line spread function (LSF) as a function of the distance from the face of the collimator (depth) in air and in a water tank of 20 cm in diameter	63
3-3 Plots of modulation transfer function (MTF) at three different distances from the face of the collimator	65
3-4 Plots of Metz filter for power factors of 10, 4 and 2	70
3-5 Fitted line spread functions and experimental counts	76
3-6 Plots of modulation transfer functions calculated from fitted line spread functions	79
3-7 Simulated cardiac-liver projection	81
3-8 Plots of normalized mean square error (NMSE) as a function of Metz power factor X for projections with different noise levels.....	84

4-1 The "mexican hat" function and its translations and dilatations (wavelets)	93
4-2 Frequency response of analyzing functions and MTF	101
4-3 Multiresolution decomposition of a high resolution MRI brain image into 5 resolution levels	102
4-4 Multiresolution decomposition of a low clinical brain SPECT projection into 5 resolution levels	103
4-5 Square 12 norm expressed in percent as a function of the sub-band image m	107
4-6 Count profiles through the simulated projection	110
5-1 Decomposition of a projection into 5 images or resolution levels.....	115
5-2 Bull's eye polar maps of the cardiac phantom without defects and LHAR = 0	120
5-3 Histograms of polar map counts for the cardiac insert without liveractivity.....	122
5-4 Horizontal profile lines through the center of a midventricular short-axis slice.....	126
5-5 Graphs depicting the effect of variation in the attenuation coefficient value upon the uniformity of reconstructed bull's eye polar maps	131
5-6 Graphs depicting the effect of variation in the attenuation coefficient value upon the normalized chi-square of polar maps ...	132
5-7 Normalized chi-square of bull's eye polar maps as a function of the liver-to-heart activity ratio (LHAR) and cutoff frequency for four different reconstruction protocols	136
5-8 Bull's eye polar maps of the cardiac liver insert (LHAR = 3.5) in water	138
5-9 Graphs depicting the effect of restoration on uniformity of bull's eye polar maps as a function of the liver-to-heart activity ratio (LHAR)	144
5-10 Effect of restoration on bull's eye polar maps	145
5-11 Myocardial tomographic slices for the cardiac insert in water with apical and infero-apical defects	149

5-12 Graphs depicting the calculated defect size as a function of the threshold level	151
6-1 Bull's eye polar maps of patient number 3	166

Abstract of Dissertation Presented to the Graduate School of the
University of Florida in Partial Fulfillment of the Requirements for the
Degree of Doctor of Philosophy

A MULTIRESOLUTION RESTORATION METHOD FOR CARDIAC SPECT

By

Juan M Franquiz

December, 1997

Chairman: Shailendra Shukla, Ph.D.

Major Department: Nuclear and Radiological Engineering

Single-photon emission computed tomography (SPECT) is affected by photon attenuation and image blurring due to Compton scatter and geometric detector response. Attenuation correction is important to increase diagnostic accuracy of cardiac SPECT. However, in attenuation-corrected scans, scattered photons from radioactivity in the liver could produce a spillover of counts into the inferior myocardial wall. In the clinical setting, blurring effects could be compensated by restoration with Wiener and Metz filters. Inconveniences of these procedures are that the Wiener filter depends upon the power spectra of the object image and noise, which are unknown, while Metz parameters have to be optimized by trial and error.

This research develops an alternative restoration procedure based on a multiresolution denoising and regularization algorithm. It was hypothesized that this representation leads to a more straightforward and

automatic restoration than conventional filters. The main objective of the research was the development and assessment of the multiresolution algorithm for compensating the liver spillover artifact.

The multiresolution algorithm decomposes original SPECT projections into a set of sub-band frequency images. This allows a simple denoising and regularization procedure by discarding high frequency channels and performing inversion only in low and intermediate frequencies. The method was assessed in bull's eye polar maps and short-axis attenuation-corrected reconstructions of a realistic cardiac-chest phantom with a custom-made liver insert and different ^{99m}Tc liver-to-heart activity ratios. Inferior myocardial defects were simulated in some experiments. The cardiac phantom in free air was considered as the gold standard reference. Quantitative analysis was performed by calculating contrast of short-axis slices and the normalized chi-square measure, defect size and mean and standard deviation of polar map counts. The performance of the multiresolution method was also assessed in ^{201}Tl clinical SPECT studies. Phantom results demonstrated that the multiresolution algorithm compensated the liver spillover artifact, yielded uniform polar maps and improved significantly the accuracy in calculating myocardial defect size. The procedure does not require operator intervention and can be easily implemented in the clinical setting by using Fourier transform techniques. Finally, the extension of the multiresolution method to other SPECT procedures is discussed and recommended.

CHAPTER 1

INTRODUCTION

Single-photon emission computed tomography (SPECT) is the clinical procedure most commonly used in nuclear medicine. The objective of SPECT is the quantitation of the three-dimensional (3-D) distribution of a radiopharmaceutical in an organ or region of interest. This is accomplished by calculating, from a set of images (projections) about the human body, the radioactivity concentration in two-dimensional (2-D) transaxial slices. Radiopharmaceuticals are usually labeled with gamma emitters with emissions between 80 keV and 300 keV. The projection images are acquired with one or more rotating scintillation or gamma cameras.

Quantitation in SPECT studies includes two broad categories of experimental procedures. The first is absolute quantitation, which means the accurate and precise measurement of certain quantities in absolute units. Examples are measurements of organ volumes and concentration of the radiotracer expressed in units of activity per unit of volume or mass. Absolute quantitations are needed in absorbed dose calculations for target and normal tissues when radionuclides are administered with therapeutic purposes (Zanzonico et al., 1989; Qian and Clarke, 1996). The other category is relative quantitation, in which relative comparisons of the radiotracer uptake in two regions or at different times are needed. This is the type of quantitation used in diagnostic studies. Examples are the assessment of brain SPECT where the radiotracer uptake in regions of the

left and right hemispheres are compared, or myocardial SPECT where the radiotracer uptake in the cardiac muscle with the patient at rest is compared with the uptake during a physical or pharmacological stress (Berman et al., 1991; Leppo, 1996).

Absolute quantitation could be an ideal goal in SPECT studies and has demonstrated great utility in physiological research (Maddahi and Czernin, 1996) and dosimetry calculations (Zanzonico et al., 1989). However, experience has demonstrated that absolute quantitation in SPECT is not required for clinical studies. The major use of SPECT in nuclear medicine is for diagnostic purposes. Thus, relative quantitation is a much more relevant problem in SPECT than absolute quantitation. In addition, the particular problem studied in this research is related to myocardial SPECT in which absolute measurements are not needed (Maddahi and Czernin, 1996). Therefore, absolute quantitation problems in SPECT will not be treated in this research. In all the material that follows, SPECT quantitation means relative quantitation.

The 3-D reconstruction problem in SPECT has been approached using iterative algorithms based on parameter estimation techniques (Shepp and Vardi, 1982; Tsui et al., 1994a; 1994b) and noniterative Fourier transform based methods (Larssen, 1980). Iterative algorithms have the potential advantage that accurate quantitative corrections for the three major degrading factors in SPECT (photon attenuation, Compton scatter and finite detector geometric resolution) can be included into the reconstruction process (Buvat et al., 1994; Tsui et al., 1994a). However, these corrections are done at the expense of such large hardware and computational requirements, that iterative algorithms have remained

unsuitable for routine clinical use. Recently, some commercial systems (Case et al., 1996; Cullom et al., 1996; McCartney et al., 1996) have included iterative algorithms but only for attenuation correction with results which are simpler than that obtained with scatter and geometric detector response compensations. Fourier transform based methods are computationally efficient but they have the limitation that accurate corrections can not be included into the reconstruction process (Larssen, 1980). Any correction for SPECT degrading factors has to be performed before or after reconstruction (Chang, 1978; Gullberg and Budinger, 1981; King et al., 1987; Buvat et al., 1994). Among these methods, the filtered backprojection algorithm (Larssen, 1980) is the most easily implemented and so far it is the only SPECT reconstruction technique used routinely in clinical studies. Therefore, because this research is focused on the analysis and solution of a particular clinical problem, only reconstruction and correction methods based on the filtered backprojection technique are considered.

The Problem

SPECT quantitation is significantly affected by photon attenuation and Compton scatter. Both effects can induce inaccuracies in clinical diagnosis, mostly in myocardial SPECT studies (Nuyts et al., 1995; O'Connor et al., 1995a; Ficaro et al., 1996; Maniawski et al., 1996). Because tissue attenuation is not uniform, the attenuation of photons in some regions produces a larger reduction in the number of counts than in other regions (Tsui et al., 1994a; 1994b). It is known that in ^{99m}Tc SPECT studies, the attenuation effect in some regions can reduce the detected

counts to 25% of the unattenuated counts (Tsui et al., 1994a). This artifactual reduction of counts can be interpreted as heterogeneous or pathological uptake distributions. A low clinical specificity (high number of false positive studies) could be obtained if apparent uptake defects due to attenuation are attributed to a true reduced radiotracer uptake. Similarly, a reduced clinical sensitivity (low number of true positive studies) could be obtained if true radiotracer uptake defects are attributed to attenuation. Another important degrading effect is Compton scatter (O'Connor et al., 1995a; Welch et al., 1995) which produces blurred images and degradation of lesion contrast (Buvat et al., 1994). Consequently, radiotracer defect severity and extent can be obscured or can appear within normal limits because of the scattered radiation that reduces clinical sensitivity. An additional and very important blurring effect is due to the limited spatial resolution of the detector (Tsui et al., 1994a).

Photon attenuation as well as Compton scattering depends on the photon energy, the body size of the patient and its composition. This is why they are considered patient-dependent effects (Tsui et al., 1994a). In addition, the physiological distribution of the radiotracer also influences the magnitude of the scatter effect. This is because the scatter contribution depends on the source distribution (Buvat et al., 1994). Finally, Compton scattering is also dependent on the width and offset of the energy window, the energy resolution of the imaging system and the acceptance solid angle of the detector collimator (O'Connor et al., 1995a; 1995b).

It is a widely recognized fact that photon attenuation is the major factor that affects the accuracy of quantitations in SPECT (Tsui et al., 1994a; Ficaro et al., 1996). This effect has been an important source of false positive studies of coronary artery disease in myocardial SPECT studies (Ficaro et al., 1996). Although myocardial SPECT without attenuation and scatter corrections has demonstrated high sensitivity in detecting coronary heart disease (Leppo, 1996), its specificity in assessing the absence of disease has been reported as sub-optimal in some groups of patients (Ficaro et al., 1996). This has been attributed to the photon attenuation in the thorax which produces false uptake defects in patients with normal myocardial perfusion (Tsui et al., 1994a; Ficaro et al., 1996; McCartney et al., 1996). As a result of intensive investigative efforts during the last decade, the new commercial SPECT systems includes hardware and software for correcting attenuation in myocardial studies (Case et al., 1996; Cullom et al., 1996; Ficaro et al., 1996; McCartney et al., 1996). Although these systems are in the process of clinical validation, preliminary data have demonstrated a significant improvement in specificity when myocardial SPECT is attenuation-corrected (Ficaro et al., 1996; McCartney et al., 1996). However, the spillover of activity from nearby organs into the inferior myocardial wall resulting from photon scatter has become a significant problem in attenuation-corrected cardiac SPECT (Ljunberg et al., 1994; King et al., 1995; Nuyts et al., 1995; Cullom et al., 1996; Ficaro et al., 1996; McCartney et al., 1996). This effect could obscure myocardial defects in the inferior wall yielding false negative results (lower sensitivity).

The main source of scattered photons in myocardial SPECT is the radiotracer uptake in liver and bowel (Case et al., 1996; King et al., 1995; Nuyts et al., 1995). The effect of photon scatter from the liver has been a recognized problem in the assessment of inferior myocardial wall perfusion in some patients, even without attenuation correction (Beller and Watson, 1991; Heo et al., 1992; Johnson, 1994). However, this undesirable effect is more severe in attenuation-corrected studies (Ljunberg et al., 1994; King et al., 1995; Nuyts et al., 1995). The reason is that attenuation correction methods can not distinguish between unscattered and scattered photons. Therefore, scattered photons are artificially amplified with attenuation correction. Although the spillover effect has been reported in ^{201}Tl myocardial SPECT (Case et al., 1996; McCartney et al., 1996), the effect is particularly important in studies with $^{99\text{m}}\text{Tc}$ -labeled compounds which have a higher liver and gall bladder uptake (Beller and Watson, 1991; Heo et al., 1992; Johnson et al., 1994).

The general consensus is that some scatter compensation has to be used in conjunction with attenuation correction in order to solve the liver spillover artifact. Different methods have been proposed to compensate for scatter in SPECT (Buvat et al., 1994), but only the simplest approaches can be used in the clinical setting because of constraints in computer capacity and processing time. Although there is not a completely satisfactory solution to the scatter problem, even the simplest methods could provide adequate compensation, at least for the accuracy required in most clinical studies (King et al., 1987; Frey and Tsui, 1995).

One common approach for compensating blurring due to both scatter and detector geometric response is restoration by deconvolution of SPECT data with a representative point spread function of the imaging system (King et al., 1983; 1987; Frey and Tsui, 1995). Assuming a linear and shift-invariant imaging system, the restoration operation is usually performed in the spatial frequency domain, where the deconvolution operator is the inverse modulation transfer function of the imaging system (King et al., 1987). However, due to the singularity of the inverse modulation transfer function and the ill-conditioned nature of the restoration problem, the presence of even small amounts of noise can lead to unacceptable restorations (Andrew and Hunt, 1977, p.114). Regularization approaches which overcome this drawback have led to the Wiener and Metz restoration filters in nuclear medicine (King et al., 1983; 1987; 1991a). The Wiener filter depends on the power spectra of the object image and noise, which are unknown (King et al., 1987; Penney et al., 1990). The Metz filter is easier to implement but there is not a general and consistent methodology for determining its optimal parameters (King et al., 1987; 1991). In addition, both types of filters are image dependent. Therefore, the problem of SPECT restoration can be summarized as the optimal design of a low-pass frequency filter for denoising and regularization operations. Optimal filter design is important because the trade-off between blurring and noise suppression depends critically on filter parameters (King et al., 1987; 1991). This is a common problem in single scale representations where it is difficult to completely separate noise from significant image features (Laine et al., 1994).

An alternative and relatively new restoration procedure based on multiresolution analysis by wavelet expansion (Daubechies, 1992, p. 7 - 11) is proposed in this research. The advantage of multiresolution representation is that it provides a general space-frequency framework in which significant image features are more easily identified and segmented from noise (Laine et al., 1994). Projections can be decomposed into a set of sub-band images corresponding to frequency channels of different bandwidth which allow a combined space-frequency representation of images. In the case of SPECT projections, high frequency or noisy sub-bands can be eliminated while restoration is performed only in those sub-band images where significant image features are present. This approach has been previously proposed by Wang et al. (1995) for general image restoration and Qian and Clarke (1996) for restoration of bremsstrahlung images of beta emitters.

In this research, a multiresolution restoration algorithm is developed for deblurring cardiac SPECT images. The practical contribution of this new approach is that denoising and regularization operations can be performed in a more straightforward and automatic way, without trial-and-error optimization (Metz restoration) or power spectra estimation (Wiener filtering). An automatic and general restoration methodology, which does not require operator intervention, would greatly help its practical implementation and application in the clinical setting.

Hypothesis and Objectives

The ultimate goal of this research is the development and critical assessment of a multiresolution regularization and denoising algorithm for compensation of the liver spillover artifact in attenuation-corrected

cardiac SPECT. The investigation is based on the hypothesis that a multiresolution restoration algorithm can compensate scatter and geometric detector response in noniterative cardiac SPECT reconstructions and with sufficient accuracy to be used in clinical studies. The demonstration of this hypothesis and the assessment of the multiresolution restoration algorithm were performed using a realistic cardiac-chest phantom in which a custom-made liver insert was included. The methods, algorithms and experimental results are presented in the chapters that follows. All the source code of the software written specifically for this research is included in appendixes.

Content of Chapters

Chapter 2 describes in detail the methodology of cardiac SPECT reconstructions, correction methods usually employed in the clinical setting and the physical degrading effects that could produce clinical artifacts. Special emphasis is dedicated to those artifacts that are due to the scattering of photons emitted within the liver in attenuation-corrected SPECT scans. Chapter 3 discusses the restoration problem in SPECT and the mathematical models in which restoration is based. The discussion starts with the most realistic and complete approach, which is the non-linear shift-variant model. Then, it is demonstrated how practical limitations in the clinical implementation of complex models have led to approximate solutions in which the imaging system is represented by a linear and shift-invariant model. This chapter also includes a discussion on restoration filters, the implementation and validation of the Metz filter, and the methodology and results of the experimental determination of the modulation transfer functions used in this research. Chapter 4

briefly presents the theory behind multiresolution wavelet representations and discusses its application in restoration of SPECT projections. This Chapter also describes the algorithms used in this research for multiresolution decomposition and restoration, the criteria for denoising and restoration and their validation in a computer simulated cardiac projection. Chapter 5 presents the experimental results obtained with the application of multiresolution restoration to attenuation-corrected SPECT reconstructions of a realistic cardiac-chest phantom with different ^{99m}Tc liver-to-heart activity ratios. Experiments simulated the liver spillover artifact with myocardial homogeneous distribution of the radiotracer (normal subject) and with the inclusion of inferior myocardial defects in the cardiac phantom (pathologic lesions). The performance of the multiresolution algorithm was compared with that of the conventional Metz restoration. Finally, Chapter 6 summarizes the conclusions of this research, discusses a preliminary application of the multiresolution restoration method to clinical studies and makes recommendations for future clinical and physical work. Special emphasis is dedicated to the extension of the multiresolution restoration method to PET and SPECT using a linear shift-variant restoration model.

CHAPTER 2 CARDIAC SPECT

The objective of cardiac SPECT is the relative quantitation and 3-D display of the distribution of a radiopharmaceutical in the cardiac muscle. Myocardial radiopharmaceuticals reach the viable myocardium by a blood flow dependent process and tomographic slices provide an accurate indication of the amount of tissue perfusion from the coronary arteries. This information plays an important role in the diagnosis, follow-up and risk stratification of patients with suspected or known coronary artery disease (CAD), which constitutes the single most common cause of death in the United States (Cullom, 1995).

In the last decade, major improvements have been made in radiopharmaceuticals, instrumentation and processing methods in order to improve accuracy in cardiac SPECT (Galt, 1994). Nevertheless, some inaccuracies persist as a consequence of the photon absorption and scatter in tissue. This chapter reviews the basic principles of cardiac SPECT, the newest systems, the physical degrading factors and the correction methods mostly used in routine clinical settings. Specific artifacts encountered in the inferior myocardial wall are discussed in more detail.

Radiopharmaceuticals

Cardiac SPECT has been performed using ^{201}Tl for almost 15 years. This is a monovalent cation which is taken up by the viable myocardium by

a blood flow and passive transport process (Beller, 1994). The myocardial uptake of ^{201}TL starts immediately after its intravenous administration and also begins to redistribute into other tissues and the myocardium itself. Significant change in distribution is observed after more than four hours (Garcia et al., 1985). An initial cardiac SPECT depicts the myocardial perfusion at the time of radiotracer injection. A later cardiac SPECT reflects the initial perfusion and the rate of regional radiotracer loss. This biokinetics behavior has been used in the study of transient changes in myocardial perfusion. Clinical protocols usually include two cardiac SPECT scans for each patient (Mahmalian et al., 1993; Matsunari et al., 1996a). In the first study, the radiotracer is administered at the peak of a pharmacologic or exercise stress. The second one is performed at rest and after redistribution has occurred. If both stress and rest cardiac SPECT scans show homogeneous distribution of the radiotracer, they are interpreted as normal studies. Regions with significant decreased activity (regional defects) are considered abnormal. If the regional defect is present at rest, this is interpreted as suggestive of myocardial infarction. If the regional defect is present after stress but is either not present or less apparent at rest, then it is considered as indicative of regional ischemia.

Unfortunately, the physical properties of ^{201}TL are less than ideal for cardiac SPECT imaging. Thallium-201 decays by electron capture to ^{201}Hg emitting characteristic x-rays in the 60 keV to 83 keV range. This low energy produces low quality images. Therefore, accurate quantitations are very difficult to make because of photon absorption and scatter in tissue. In addition, the relatively long half-life of ^{201}TL (73 hours) does not

allow the administration to the patient of high activities, resulting in noisy SPECT images. On the contrary, ^{99m}Tc , the most widely used radionuclide in nuclear medicine, has a monoenergetic gamma emission of 140 keV which is ideal for gamma camera imaging. The shorter half-life (6 hours) of ^{99m}Tc allows the administration of activities that are up to 10 times higher than those of ^{201}Tl . This yields higher quality images in a shorter time period. Another advantage is that ^{99m}Tc is available from a $^{99}\text{Mo}-^{99m}\text{Tc}$ generator 24 hours a day, while ^{201}Tl is cyclotron-generated and requires off-site delivery. These superior properties of ^{99m}Tc motivated in past decades the search for different compounds to be used as ^{99m}Tc -labeled cardiac perfusion agents. In December 1990, the Food and Drug Administration approved the clinical use of two of those compounds: ^{99m}Tc -sestamibi (DuPont Nemours, Inc.) and ^{99m}Tc -teboroxime (Squibb Diagnostic, now Bracco Diagnostics). Both have shown successful results in clinical trials (Beller and Watson, 1991; Berman et al., 1991; Johnson, 1991; Van Train et al., 1994). More recently, a new compound, ^{99m}Tc -tetrofosmin (Amersham International, plc), has also been approved and is used commercially (Braat et al., 1994; Matsunari et al., 1996a).

The compound ^{99m}Tc -sestamibi is a monovalent cation that is taken by the viable myocardium by a passive transport process, similar to the uptake of ^{201}Tl (Beller and Watson, 1991). This compound has a long myocardial residence time (approximately 5 hours) and little redistribution (Berman et al., 1991). In contrast, ^{99m}Tc -teboroxime is a neutral lipophilic compound that diffuses rapidly across phospholipid membranes in a manner similar to freely diffusible radiotracers such as

^{133}Xe (Johnson, 1991). Its myocardial washout is flow dependent and shows a rapid bi-exponential clearance with half-times of 3 to 6 minutes and 60 minutes for the early and late components, respectively (Johnson, 1994). The myocardial agent $^{99\text{m}}\text{Tc}$ -tetrofosmin is a lipophilic cationic compound with a rapid heart uptake and relatively slow clearance (Braat et al., 1994). These different redistribution properties have required different clinical protocols from those used for ^{201}Tl SPECT (Berman et al., 1991; Braat et al., 1994; Johnson, 1994; Matsunari et al., 1996a).

One adverse aspect of $^{99\text{m}}\text{Tc}$ -labeled myocardial agents is the hepatobiliary excretion of these compounds. Photon scatter from hepatic activity up into the heart can interfere with interpretation and quantitation of inferoapical segments, specially in obese patients or in individuals with high diaphragms (Johnson, 1991). Artifacts in the inferior myocardial wall due to liver and abdominal background have been reported in clinical studies with $^{99\text{m}}\text{Tc}$ -sestamibi (Middleton and Williams, 1993; DePuey, 1994), $^{99\text{m}}\text{Tc}$ -teboroxime (Johnson, 1991; 1994; Chua et al., 1993) and $^{99\text{m}}\text{Tc}$ -tetrofosmin (Braat et al., 1994; Matsunari et al., 1996b).

In spite of their physical advantages, $^{99\text{m}}\text{Tc}$ compounds have not replaced ^{201}Tl in clinical studies. Both radionuclides are currently used in cardiac SPECT.

SPECT Data Acquisition

The first step in SPECT studies is the acquisition of a set of planar images or projections about the human body using one or more rotating gamma cameras. Typical SPECT studies acquire 60 projections at intervals of 6 degrees. The gamma camera orbits the patient in a step-and-

shoot motion mode. This means that there is no data acquisition during the time in which the detector is moving between two positions. Projections are converted and stored as computer files with formats of 64 x 64, 128 x 128 or 256 x 256 pixels. The most common format in cardiac SPECT is 128 x 128 pixels.

Gamma Camera

The gamma camera is an image formation device that uses a scintillator detector with a large NaI(Tl) crystal coupled to an array of photomultiplier tubes (Cho et al., 1993, p. 165). The NaI(Tl) crystal can be either circular, with diameter of 40 cm, or rectangular, with dimensions of 40 cm x 20 cm. The thickness of the crystal is approximately 1.25 cm. The number of photomultiplier tubes depends on the manufacturer, but present-day gamma cameras use from 37 to 101 tubes arranged in an hexagonal pattern. A multihole collimator, made of a high atomic number substance, is attached to the external surface of the crystal and confines the direction of the incident photons to an extremely small acceptance solid angle. Thus, the crystal receives gamma-rays only from sources directly in front of it, making a projection from the 3-D source distribution onto the 2-D face of the scintillation crystal. When a gamma photon is absorbed within the crystal, the photomultiplier tubes closest to the interaction position receive an amount of light proportional to their distance to the event. The output signals of the photomultiplier tubes are processed by an analog or digital circuitry to calculate a pair of coordinates (x,y) representing the 2-D position of the interaction on the crystal. Finally, the output from each tube is summed to obtain a signal proportional to the total energy absorbed within the crystal. A

pulse-height analyzer retains only those events whose signal amplitude lies within a selected small window ($\pm 10\%$) around the amplitude of the photopeak. This energy discrimination excludes a high percent of Compton scattering events that occur in the patient, the collimator or in the crystal itself.

Spatial Resolution and Sensitivity

Two important variables that characterize the performance of a gamma camera are spatial resolution and sensitivity. Spatial resolution indicates the ability of the system to identify the exact location at which a photon has been emitted. This variable is commonly measured in terms of the full width at half-maximum (FWHM) of the line spread function (LSF) obtained from the count profile recorded across the image of a line source. The FWHM value critically depends on the energy resolution of the detector, the energy window, the source-to-detector distance, the geometric response of the collimator and the presence of a scattering medium. The best spatial resolution is nearest the collimator. By increasing the distance from the detector to the source, the spatial resolution is significantly degraded. The FWHM in air at most typical organ depths (≈ 10 cm) for low-energy high resolution (LEHR) and low-energy general purpose (LEGP) collimators are approximately 7 mm and 9 mm, respectively (Tsui et al., 1994a). In SPECT studies, at the typical distance from the collimator to the center of rotation (≈ 18 cm), the FWHM is approximately 14.5 cm. The presence of a scattering medium (e.g., the patient) should increase the FWHM up to 16.5 mm.

Sensitivity is defined for a point source and expressed in terms of counts per minute per unit of activity per meter from the center of the

camera detector (Nichols and Galt, 1995). Unlike spatial resolution, sensitivity decreases only slightly with distance. When distance increases, the number of photons per unit of area decreases by the inverse square of the distance, but then the area of the crystal exposed to the source increases by the square of distance. This is valid only in the absence of an attenuating medium. Conventional parallel-hole collimators used in SPECT permit only about 0.015% of the emitted photons to interact with the scintillation crystal. For most SPECT studies, the average count rate is on the order of 10^4 counts per second. Because of the limited number of counts per pixel, projections can be severely corrupted by random noise.

Sensitivity could be improved by increasing the size of collimator holes or by using more holes of smaller diameter but thinner septal thickness. Unfortunately, there is an inverse relationship between spatial resolution and sensitivity. Both solutions to increase sensitivity allow undesirable photons to penetrate the collimator with the subsequent degradation in spatial resolution. The possibility of increasing the number of counts by increasing the acquisition time is not technically viable. Long acquisition times increase the probability of patient involuntary motion which can give rise to image artifacts. On the other hand, the biokinetics of some radiotracers commonly used in cardiac SPECT do not allow long acquisition times. Increasing the amount of radiotracer also is limited by dosimetry considerations and the dead time of SPECT systems ($< 1 \mu s$).

Practical solutions to increase the number of counts in cardiac SPECT while preserving spatial resolution have been proposed by modifying

acquisition modes (Galt, 1994; Galt and Germano, 1995). The most common modalities have been the following: a) The introduction of elliptical orbits to minimize the distance from the camera to the body throughout all the acquisition is one modality. b) Acquisition of projections in an orbit of 180 degrees instead of the full 360 degrees rotation is another (this method excludes those projections which are severely distorted by photon attenuation and scatter. The acquisition time is then confined to count acquisitions for the most reliable projections). c) The third modality is rotation of the gamma camera and data acquisition in continuous mode rather than the conventional step-and-shoot. In this mode, counts are not wasted during the time the gamma camera is moving. In the step-and-shoot mode the waste of counts can be significant because detectors take 2 to 4 seconds to move between two positions (Galt and Germano, 1995).

Multi-Detector SPECT Systems

The most important advance for improving sensitivity has been the development of multi-detector SPECT systems: the higher the number of detectors, the larger the number of counts that are acquired in the same period of time. The higher sensitivity of these systems has also improved spatial resolution by allowing the use of high resolution collimators (Galt and Germano, 1995). Two opposed detector systems have been used for many years. They were developed for acquiring simultaneous anterior and posterior projections in body skeleton imaging. Three-detector rotating SPECT systems were introduced by Trionix Research Laboratory (Twinsburg, OH) and Picker International (Cleveland, OH) in the late 1980s (Galt, 1994). Today, almost every manufacturer produces three-headed SPECT systems which are mostly used for cardiac and brain studies. Other systems

designed specifically for cardiac SPECT are those with two rectangular gamma cameras mounted at 90 degrees, for example, the Optima gamma camera from General Electric Medical Systems (Milwaukee, WI), the Cardial from Elscint (Hackensack, NJ), and others (Galt, 1994; Case et al., 1996; Cullom et al., 1996).

SPECT Reconstruction

The Inverse Problem in SPECT

The 3-D reconstruction or inverse problem in SPECT can be stated as follows: Given a set of collimated projections $\{P_\theta[r]\}$ around a transaxial plane t of constant thickness and along an axis r at right angles to the axis of rotation, calculate the density function of the radioactivity concentration $g(x,y)$ in the transaxial plane t that produces $\{P_\theta[r]\}$ (Figure 2-1).

This problem has been extensively investigated using iterative algorithms and Fourier transform based methods. However, currently only the filtered backprojection (FBP) technique has been routinely used in clinical studies and universally incorporated in commercial SPECT systems.

The Filtered Backprojection Technique

The FBP is a Fourier transform method based on the application of two mathematical operators to projection data. The first one filters projections using a reconstruction band-pass frequency filter. The second operator, which is the backprojector or backprojection operator, assigns each projection filtered pixel values to all pixels along a perpendicular corresponding line through the reconstructed transaxial image plane. This is done for all the pixels in the projection and over all projection

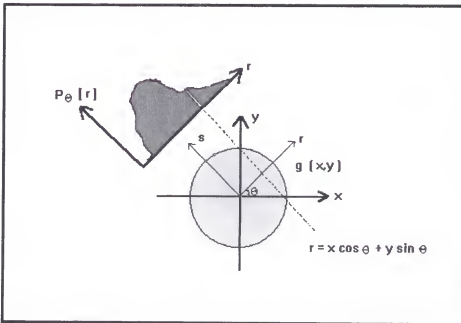


Figure 2-1. Density function $g(x,y)$ in the transaxial plane XY and its projection $P_\theta[r]$ at an angle θ .

angles. The reconstruction is achieved by the superposition of the filtered projection values for all angles (Figure 2-2).

Briefly, the method can be explained as follows: For a narrow ray, assuming ideal detector response, no photon attenuation and no photon scatter, the relationship between $g(x,y)$ and the set $\{P_\theta[r]\}$ (Figure 2-1) is given by the Radon transform (Tretiak and Metz, 1980):

$$P_\theta[r] = R[g(x,y)] = \iint g(x,y) \cdot \delta(x \cdot \cos\theta + y \cdot \sin\theta - r) dx dy ,$$

where R is the Radon operator. The $x-y$ coordinate system is stationary and defines the transaxial image plane. The $r-s$ system is rotating and gives

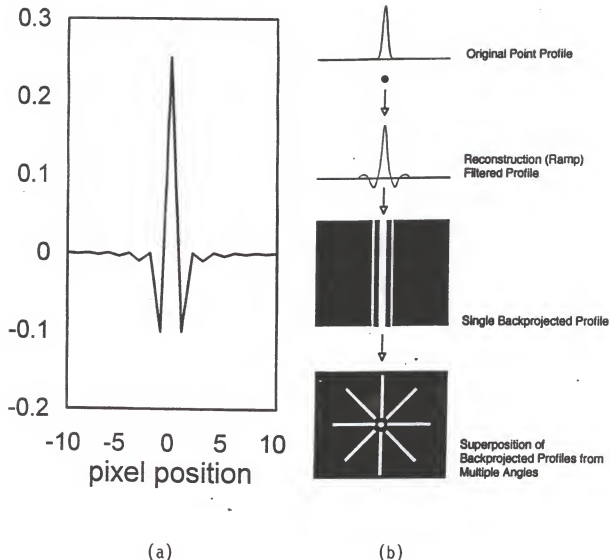


Figure 2-2. Filtered backprojection technique. (a) Convolution kernel or reconstruction filter in the spatial domain; (b) Filtering, backprojection operation and reconstructed transaxial image plane of a central point source.

the reference for the projection $P_\theta[r]$ (Figure 2-1). Equations for coordinate transformation between the two systems are given by

$$r = x \cdot \cos\theta + y \cdot \sin\theta$$

$$s = -x \cdot \sin\theta + y \cdot \cos\theta.$$

From the Radon transform and equations for coordinate transformation, it can be demonstrated (Rogers and Clinthorne, 1987) that the one-dimensional (1-D) Fourier transform (FT) of the projection $P_\theta[r]$ is equal to the FT of $g(x,y)$ along a radial line in the frequency domain at the same angle as the projection. This is the "Central Slice" theorem, which constitutes the basis of Fourier reconstruction methods. Mathematically, it can be expressed as

$$FT[P_\theta[r]] = \iint g(x,y) \cdot \exp[-2\pi j(w_x \cdot x + w_y \cdot y)] \cdot dx dy ,$$

where $w_x = w \cdot \cos\theta$ and $w_y = w \cdot \sin\theta$. Then, the above equation can be expressed as

$$FT[P_\theta[r]] = FT[g(x,y)]_\theta = G(w, \theta) ,$$

where this equation indicates that $g(x,y)$ in the frequency domain $G(w_x, w_y)$ can be synthesized from the radial samples $G(w, \theta)$, so that:

$$g(x,y) = FT^{-1}[G(w_x, w_y)] .$$

Expressing w_x and w_y in polar coordinates (w, θ) , the above equation becomes

$$g(x, y) = \iint G(w, \theta) \cdot |w| \cdot \exp[2\pi j w(x \cdot \cos\theta + y \cdot \sin\theta)] \cdot dw d\theta ,$$

where $|w|$ is the Jacobian of the coordinate transformation. The above integral can be arranged as

$$g(x, y) = \int P_{f\theta}[x \cdot \cos\theta + y \cdot \sin\theta] \cdot d\theta , \quad (2.1)$$

where

$$P_{f\theta}[r] = FT^{-1}[FT[P_\theta[r]] \cdot |w|] . \quad (2.2)$$

Equations (2.1) and (2.2) indicate that $g(x, y)$ is calculated by applying two operators to the projection data. Equation (2.2) corresponds to a filter operator, where $P_{f\theta}[r]$ is the filtered projection and $|w|$ is the ramp filter (Larssen, 1980). Equation (2.1) represents the backprojection operator and indicates the backprojection of $P_{f\theta}[r]$ onto the plane x-y.

Because of the divergent nature of $|w|$, the integral (2.2) can not be evaluated. Ramachandran and Lakshminaryanan (1971) solved this problem by considering that $FT[P_\theta[r]]$ is band limited and then $|w|$ can be truncated at some value $|w_{MAX}|$. Therefore, the ramp filter was modified according to

$$L(w) = |w| \quad \text{if } |w| < 2\pi f_N$$

$$L(w) = 0 \quad \text{Otherwise,}$$

where f_N is the Nyquist frequency (Gonzalez and Wintz, 1977, p. 70) defined by

$$f_N = \frac{1}{2\Delta x},$$

and Δx is the one-dimensional pixel size.

The filtering operation in the frequency domain is equivalent to the convolution of $P_\theta[r]$ with the ramp filter in the spatial domain (Gonzalez and Wintz, 1977, p. 61). The convolution kernel $L(r) = FT^{-1}[L(w)]$ is a symmetrical function with negative sidelobes (Figure 2-2a) that introduces negative or null values in the filtered projection. These negative values compensate the blurring and star effects produced by the backprojection operation (Figure 2-2b).

Smoothing Window Functions

There are two practical limitations in the use of the ramp filter. First, $L(w)$ is a high-pass band filter. This is an ideal function to reconstruct noise-free data, but not real SPECT projections which are degraded by statistical noise. Second, the truncated ramp filter introduces rim and overshoot artifacts (Gibbs phenomenon) into the image. This is because the hard cutoff of the ramp filter produces ripples in the filter response to image edges (Algazi et al., 1995). Both drawbacks are overcome by multiplying $L(w)$ by a low-pass frequency filter or smoothing window function. Thus, the high-pass frequency ramp filter becomes a band-pass frequency filter which gradually rolls off the high frequencies rather than cutting off sharply at f_N . The most commonly used window functions in clinical SPECT are the Butterworth, Hann, Hamming and Parzen

low-pass frequency filters (Larssen, 1980). Figure 2-3 shows examples of some convolution kernels used in SPECT and their frequency response. The exact form of the convolution kernel depends upon how much low-pass filtering is acceptable in order to reduce the noise in the images while preserving the resolution. The width of the central positive peak determines the amount of smoothing and the negative sidelobes determines the amount that is subtracted from the neighboring backprojected rays.

In practical reconstruction algorithms, the window function is a 2-D radially symmetric low-pass frequency filter that is applied to projection images before reconstruction. Then, the ramp filter is applied one-dimensionally to the transaxial projection data, row by row. The objective of the first operation is to avoid streaking artifacts in sagittal and coronal slices, which are calculated from transaxial data (Larssen, 1980). These artifacts appear when projection data are smoothed in just one direction. The 2-D prereconstruction smoothing avoids streaking artifacts but increases blurring in both transaxial and axial directions.

Myocardial Tomographic Slices

Coronal and sagittal slices are calculated from transaxial slices for further evaluation of the 3-D distribution of the radiotracer (Larssen, 1980). They are displayed in three perpendicular axes parallel to the natural vertical long, horizontal long and short axes of the heart (Figure 2-4). Axes reorientation is performed by two successive image rotations through angles selected by the operator (Borello et al., 1981; Garcia et al., 1985). The most important slices from the clinical point of view, are those in the short axis. These slices are normal to the left ventricular long axis and provide a set of cross-sectional slices of the

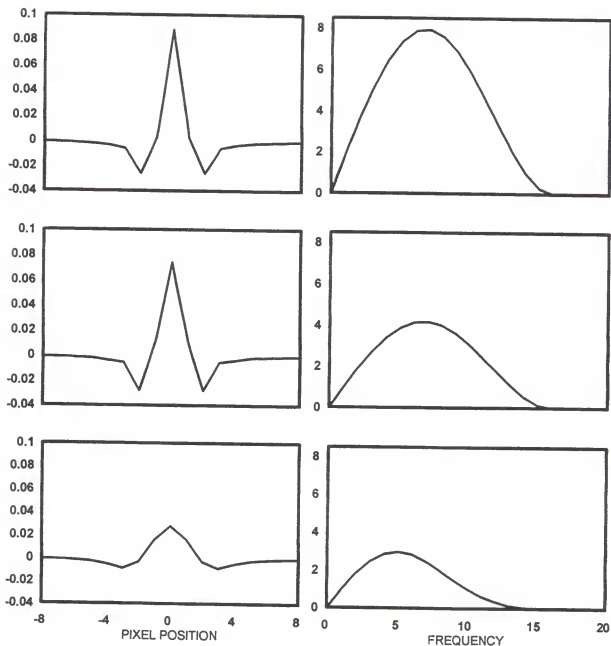


Figure 2-3. SPECT reconstruction convolution kernels (left) and their frequency response (right). From top to bottom: Hamming, Hann and Parzen filters.

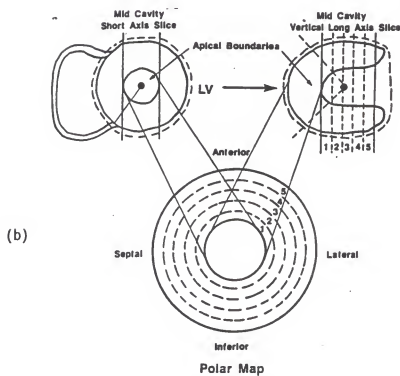
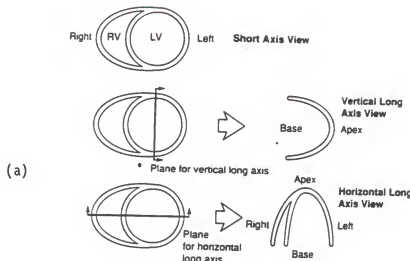


Figure 2-4. Myocardial tomographic slices. (a) Standardized display according to the natural axes of the heart (Berman et al., 1991); (b) Computer-generated bull's eye polar map display of circumferential maximal count profiles of short axis slices. Apex is derived from both short and vertical long axis slices (Matsunari et al., 1996b).

cardiac muscle. This reorientation standardizes the cardiac image display and facilitates qualitative and quantitative analysis by exploiting the symmetry of normal left ventricles in the short axis (Berman et al., 1991).

Quantitative Analysis

Quantitative estimates of the radiotracer distribution are commonly performed using circumferential maximal count profiles of short-axis slices (Berman et al., 1991). An alternative semiquantitative method is the bull's-eye plot or display of SPECT data in the form of a polar map (Garcia et al., 1985). This procedure converts the circumferential maximal count profiles of short axis slices into polar coordinates profiles. Slices are displayed as a series of concentric circles, with the apex at the center, the inferior wall at the bottom, the anterior wall at the top, the septum at the left and the lateral wall at the right (Figure 2-4). Pixel counts inside all rings are normalized to the maximum pixel counts and expressed in percent of this value. This representation results in a simple 2-D display of the 3-D data and allows the comparison of patients's bull's-eye with reference normal standards (Ficaro et al., 1996; Matsunari et al., 1996b).

Degrading Factors in SPECT

The FBP method provides accurate 3-D reconstruction for idealized projections free of the degrading effects due to the geometric response of the detector, photon attenuation and Compton scatter. When the method is applied to real projections the reconstruction is significantly limited in terms of accurate quantitation, spatial resolution and contrast (Tsui et al., 1994a; 1994b). Therefore, a number of pre- and postreconstruction

semiquantitative techniques have been proposed for compensating distortions when the FBP technique is used in SPECT reconstructions (Chang, 1978; Larsson, 1980; King et al., 1991; Buvat et al., 1994; Tsui et al., 1994a; Case et al., 1996). The discussion that follows, describes the three main degrading factors and the correction methods mostly used in experimental and clinical cardiac SPECT studies.

Geometric Response of the Detector

The geometric response of the detector is the main cause of blurring and loss of spatial resolution in SPECT studies (Tsui et al., 1994a). This degrading factor critically depends on the geometric response of the collimator and the intrinsic resolution of the scintillator crystal. However, the major contributor to the detector response is the collimator. The number of collimator holes and their acceptance solid angle are the determining factors in the spatial resolution of a SPECT system. The geometric response of the detector is experimentally characterized by the point spread function (PSF), which fully represents the blurring characteristics of the SPECT system. This is a spatially variant function, which rapidly broadens as the distance from the collimator increases.

Photon Attenuation

Photon attenuation is the most important source of inaccuracy in SPECT quantitations (Tsui et al., 1994a; 1994b) and is considered the major cause of false-positive cardiac SPECT studies (King et al., 1996). The attenuation effect can reduce the detected counts to 25 % and 40 % of the unattenuated counts for ^{99m}Tc and ^{201}Tl , respectively (Tsui et al., 1994a). Because photon attenuation is a function of the thickness and composition of the absorbing medium, the attenuation effect is not uniform

for an imaged organ. This is specially important in cardiac SPECT due to the geometric position of the heart and because surrounding tissues (lung, muscle, adipose tissue, bone) have very different attenuation coefficients. When cardiac SPECT is performed in supine position, there is a significant decrease in myocardial inferior wall counts as a result of attenuation by the left hemidiaphragm (Segall and Davis, 1989; Wallis et al., 1995) and the overlaying right ventricle and right ventricular blood pool (DePuey and Garcia, 1989). However, the problem is not limited to the reduction of counts in the inferior wall. Significant artifacts are induced in the anterior wall due to attenuation from the breast tissue in females (DePuey and Garcia, 1989). Also, in obese patients the accumulation of adipose tissue in the lateral chest wall may result in an apparent perfusion defect in the lateral wall (Wallis et al., 1995).

Attenuation Correction. The attenuation problem in SPECT can be mathematically described by the inclusion of a negative exponential term in the Radon transform (Tretiak and Metz, 1980). The resultant projection is known as the attenuated Radon transform (Gullberg and Budinger, 1981). So far, an analytical solution to the attenuated Radon transform has not been found. Different attenuation correction numerical algorithms have been proposed, but a complete solution to the problem has not as yet been proposed (Gullberg and Budinger, 1981; Tanaka et al., 1984; Tsui et al., 1994a; King et al., 1996). However, considerable progress has been achieved in the last decade due to improvements in correction algorithms, hardware of SPECT systems and increased computing power available in current SPECT computers.

Depending on their application before, during or after reconstruction, there are three broad approaches for attenuation correction: a) preprocessing correction; b) intrinsic correction; and c) postprocessing correction. Preprocessing methods are based on the assumptions of a uniform concentration of activity and a constant attenuation coefficient in the absorbing medium. One method corrects by hyperbolic functions the arithmetic or geometric mean of conjugate opposing projections ($P_\theta[r]$ and $P_{\theta+n}[r]$) before filtering and backprojection (Keyes, 1976; Larssen, 1980; Tsui et al, 1994a). A practical inconvenience is that the body contour is needed. The simplest and easiest prereconstruction correction makes the reconstruction for 180° with the arithmetic or geometric mean of the conjugate opposing projections which were taken over 360°. This correction is employed in commercially available SPECT systems.

Intrinsic compensation methods include attenuation correction directly into the reconstruction process. They can be divided into two categories: a) analytical and b) numerical. The first group is based on an approximate solution of the attenuated Radon transform with uniform attenuation coefficient (Gullberg and Budinger, 1981; Tanaka et al, 1984). Analytical intrinsic methods use a first correction for the body outline. This is accomplished by multiplying each projection pixel by the inverse of the attenuation along a ray from the projection pixel to the center of rotation. After that, a second correction compensates for the actual attenuation distance. This can be performed in various ways, but the best known method is the Gullberg and Budinger (1981) attenuation-weighted backprojection technique. This method uses window functions which depend

on a uniform attenuation coefficient (Gullberg and Budinger, 1981). Filtering is performed with a modified ramp filter in which its value is zero in the frequency range below $\mu/2\pi$ (Gullberg and Budinger, 1981). Then, filtered projections are backprojected and multiplied by an attenuation weighting factor which depends on the position of the pixel in the reconstruction matrix. One important limitation is that these algorithms amplify noise and introduce artifacts in low-count images.

Bellini et al. (1979) have proposed an analytical solution for the attenuated Radon transform, which relates the non-attenuated and attenuated projection sinograms in the frequency domain. The sinogram is an image which represents the projection data as a function of projection angles. The sinogram is formed by taken the same row of data from all projection images and creating a new image in which the x-coordinate values are those of the projection and the y-values are determined by the projection angle. The image is called "the sinogram" because a single point should follow a sine curve in this type of representation. Thus, the relationship described by Bellini is given by

$$P'(\nu, \theta) = P(\nu, \theta) \cdot [(\nu^2 + \mu^2)^{1/2}, \theta + i \sinh^{-1}(\mu/\nu)] ,$$

where P' and P represent the attenuation-compensated and original frequency domain sinograms, respectively.

The Bellini's method requires the interpolation of the sinogram in the frequency domain to evaluate $P(\nu, \theta)$ at the frequency value $(\nu^2 + \mu^2)^{1/2}$ and at complex angle $\theta + i \sinh^{-1}(\nu/\mu)$. After interpolation in the ν and θ directions, the Fourier inverse-transform of the sinogram is performed to obtain the attenuation-compensated sinogram. The advantages of this

method are its speed and that can be used with the FBP technique. Disadvantages are that corrections are only valid for convex regions of uniform attenuation around the center of rotation and ignores the problem of distance-dependent resolution. In addition, the Bellini's method has not been tested extensively as other methods and its robustness in clinical studies is unknown (King et al., 1995).

Intrinsic numerical methods incorporate a non-uniform attenuation coefficient map into an iterative statistical estimation algorithm such as the maximum likelihood-expectation maximization (ML-EM) or the weighted least squares-conjugate gradient (WLS-CG) (Tsui et al., 1994b). The ML-EM method assumes a Poisson distribution in the projection counts and determines the source distribution that most likely reproduces the projection data (Shepp and Vardi, 1982). Briefly, the ML-EM method works as follows. An initial estimate of the transaxial source distribution is performed, e.g., using the FBP technique. Next, each transaxial pixel is updated according to the iteration scheme given by

$$g^i(x,y) = g^{i-1}(x,y) \cdot B \left[\frac{P_\theta[r]}{P_\theta^{i-1}[r]} \right],$$

where B is the backprojection operator and the index i enumerates the iteration. The previous transaxial source distribution $g^{i-1}(x,y)$ is corrected by the backprojection of the ratio of the actual projection counts $P_\theta[r]$ over the projection counts $P_\theta^{i-1}[r]$ which were calculated assuming a source distribution given by $g^{i-1}(x,y)$. In this scheme, the backprojection operator B weights the projection counts by the likelihood that they actually contribute to the source distribution. The 3-D

implementation of this iterative scheme is straightforward. In theory, the major advantage of this method is that the physical image formation process (attenuation, geometric collimator response and even scatter) can be modeled into the projector and backprojector operators. The inclusion of degrading effects into the reconstruction scheme allows more accurate corrections and source distribution quantitation (Tsui et al., 1994a; 1994b). This method have two major disadvantages. The first is the processing time which can be excessive for clinical studies, specially if 3-D collimator geometric response corrections are included. The second is the slow and image dependent convergence, in which the noise increases as the number of iterations increases. Other iterative reconstruction algorithms (Tsui et al., 1995) have been proposed to speed the convergence and reduces noise, but so far the ML-EM algorithm is the most widely used and the standard for accurate quantitation comparations with other reconstruction methods.

When only attenuation correction is included in the ML-EM reconstruction algorithm, proper compensation may be achieved after a limited number of iterations. Recently, several commercial system (Vantage system from ADAC Laboratories, Optima L-shaped Cardiac Camera from General Electric Medical Systems, and PRISM 3000 SPECT Camera from Picker Inc.) have included the ML-EM reconstruction algorithm in conjunction with transaxial attenuation maps for performing accurate non-uniform attenuation corrections. Attenuation coefficient maps have been simultaneously determined using point or line sources in multi-detector SPECT systems. At the present time, these systems are in process of clinical validation (Case et al., 1996; Cullom et al., 1996).

Chang Attenuation Correction Algorithm

Postprocessing techniques are based on the original Chang attenuation correction algorithm (Chang, 1978). This is the best known attenuation correction procedure and was specifically designed to work in conjunction with the FBP method. Most commercial SPECT systems have incorporated this correction technique. The algorithm is implemented by dividing each reconstructed pixel value by the average attenuation factor for that pixel (Chang, 1978). The average attenuation factor is calculated as the average attenuation along all rays from the pixel to the boundary of the attenuating medium. Therefore, the correction factor for attenuation at a point (x,y) is given by

$$c(x,y) = \frac{M}{\sum_{k=1}^M \exp(-\mu \cdot l_k)} ,$$

where M is the total number of projections and l_k is the distance between point (x,y) and the boundary point of the medium at projection k . When the source is extensively distributed, the above correction factor over- or under-corrects some parts of the image, depending on the source distribution. Next, a second correction is needed. This correction is performed by projecting the corrected data to form a new set of projections. A set of error projections is obtained by subtracting each corrected projection from its corresponding original projection. Error transaxial slices are reconstructed by using the FBP method and corrected for attenuation again. These slices are added to the initially corrected slices to form the final attenuation-corrected image. This correction can

be repeated using more than one iterative step. Experimental studies have demonstrated that the Chang algorithm gives the best results after only one or two iterations (Tsui et al., 1989). For nonuniform attenuation, the attenuation coefficient distribution can be calculated from an attenuation map (Tsui et al., 1989; Manglos et al., 1987). This method provides a significant improvement in image quality and acceptable quantitation for practical purposes (Manglos et al., 1987; Tsui et al., 1989; 1994b).

Photon Scattering

Compton scattering is the dominant interaction in tissue for the energy range (50 keV to 300 keV) used in nuclear medicine (Evans, 1985, p. 714). In addition, small scattering angles are more probable than large deflections for the emission energies of ^{201}Tl and $^{99\text{m}}\text{Tc}$. Hence, a relatively high number of forward deflections can pass through the collimator holes. In theory, scattered photons should be separated from those unscattered using the pulse height analyzer of the detector. However, because the finite energy resolution and small sensitivity of SPECT detectors, a certain number of scattered photons has to be counted in order to detect the largest possible number of unscattered events (O'Connor et al., 1995a; Welch et al., 1995). Photon scatter accounts for approximately 40 % and 60 % of the total counts for $^{99\text{m}}\text{Tc}$ and ^{201}Tl cardiac SPECT studies, respectively (O'Connor et al., 1995a; 1995b). This undesirable effect degrades the reconstructed slices by blurring fine details and lowering contrast, and leads to inaccuracies in the quantitative estimate of perfusion defect size (O'Connor et al., 1995a; 1995b; Case et al., 1996; Cullom et al., 1996; McCartney et al., 1996).

For projections acquired with parallel hole collimators, photons emitted in a given transaxial plane can be detected as emitted in other transaxial plane due to Compton scattering and the finite detector resolution. This effect could be significant in cardiac SPECT where the out-of-plane scattered liver photons are detected in the inferior myocardial planes (Smith, 1994; King et al., 1995).

A simple scatter model based on the Klein-Nishina (Evans, 1982, p. 683) differential probability for a scatter angle and incident energy can give an estimate of the contribution and importance of out-of-plane scattered photons on a given transaxial plane. It is known (Evans, 1982, p. 675) that the relation between the initial energy E_o and final energy E_f of a photon experiencing Compton interaction is given by

$$E_f = \frac{E_o}{1 + \alpha \cdot (1 - \cos\varphi)} ,$$

where φ is the angle between the initial and final direction of the photon and α is the ratio of the incident photon energy and the electron rest mass. Assuming that the detector has perfect energy resolution and that a rectangular energy window ΔE is centered at E_o , the maximum allowable first order scatter angle within this energy window is calculated by

$$\varphi_{\max} = \cos^{-1} [1 - \frac{\Delta E}{\alpha \cdot (2E_o - \Delta E)}] ,$$

where for ^{99m}Tc : $E_o = 140$ keV, $\alpha = 0.274$ and $\varphi_{\max} = 54^\circ$.

In this simple model, a photon is allowed to be scattered only once and photon paths are only traced from each voxel containing activity towards the detection plane (Figure 2-5). The incident photon flux

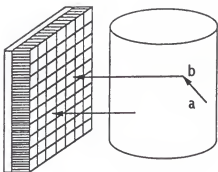


Figure 2-5. Detection geometry of unscattered and out-of-plane scattered photons. It is assumed a perfect geometry resolution and only perpendicular photons to the plane of detection are registered. The out-of-plane voxel is represented by "a". Voxel "b" belongs to the emission plane. Photons emitted by "a" and scattered at voxel "b" becomes an additional effective source of activity at b (Smith et al., 1993).

density Φ (photons/cm²-voxel) emitted by an out-of-plane voxel "a" which can reach a voxel "b" in the emission transaxial plane (Figure 2-5) can be expressed as

$$\Phi = \frac{A_a}{4\pi d^2} \cdot \exp(-\mu \cdot d) ,$$

where A_a is the activity of the out-of-plane voxel, d (cm) is the distance from the out-of-plane voxel "a" to the emission voxel "b" and μ (cm⁻¹) is the narrow-beam attenuation coefficient of the uniform medium. It is supposed that the flux arriving to the emission voxel is scattered and becomes in an additional source of activity. From the simple geometry of Figure 2-5, once-scattered photons will be detected only when the

scattered angle is given by: $\varphi = \sin^{-1}(\Delta t/d) \leq 54^\circ$, where Δt is the distance between the out-of-plane and emission plane. Assuming a pixel size of 0.356 cm, $\Delta t = 0.356 \times n$, where n is the number of transaxial planes between the voxel "a" and the emission voxel "b" (Figure 2-5). Then, the above equation can be represented by

$$\phi = \frac{A_a \cdot \sin^2 \varphi}{1.593 n^2} \cdot \exp(-0.0534 n / \sin \varphi),$$

Notice that the scatter angle has been chosen such that scattered photons propagate only along a perpendicular projection ray accepted by the detector (Figure 2-5). Therefore, the total number of out-of-plane photons which are scattered by the voxel "b" and registered by the detector, is calculated by adding the contributions of all out-of-plane source voxels multiplied by the probability of scattering at the corresponding angle

$$N_g = \sum_i \phi(\varphi_i) \cdot \left(\frac{\Delta \sigma_v}{\Delta \varphi_i} \right) \cdot \Delta \varphi_i,$$

where $\Delta \sigma_v / \Delta \varphi_i$ is the differential cross section for photon scattering at angle φ_i per unit of scattering angle and per voxel. This is calculated from (Evans, 1982, p. 690)

$$\left(\frac{\Delta \sigma_v}{\Delta \varphi_i} \right) = \rho_e \cdot m_v \cdot \left(\frac{\Delta_e \sigma}{\Delta \Omega} \right) \cdot \left(\frac{\Delta \Omega}{\Delta \varphi_i} \right),$$

where, $\rho_e = 3.343 \times 10^{23}$ electrons/g is the electron density of water (Attix 1986, p. 531), $m_v = 1 \text{ g/cm}^3 \times (0.356 \text{ cm})^3$ is the mass of a voxel,

$\Delta\Omega/\Delta\varphi_i = 2\pi \sin\varphi_i$ is the differential solid angle per unit of scattering angle (Evans, 1982, p. 690). Finally, $\Delta_e\sigma/\Delta\Omega$ is the differential scattering cross section at angle φ_i per unit solid angle and per electron and is calculated from (Evans, 1982, p. 683)

$$\left(\frac{\Delta_e\sigma}{\Delta\Omega}\right) = \frac{r_o^2}{2} \cdot \frac{(1+\cos_2\varphi)(1+\alpha(1-\cos\varphi)) + \alpha^2(1-\cos\varphi)^2}{(1+\alpha(1-\cos\varphi))^4},$$

where $r_o = 2.8179 \times 10^{-13}$ cm is the classical electron radius (Attix, 1986, p. 525).

Figure 2-6 shows the relative contribution of out-of-plane scattered photons per voxel as a function of the scattering angle for different out-of-plane distances. According to this model, the relative contribution of nearest planes to the out-of-plane detected scattered photons at the voxel "b" are 73%, 16.6%, 6.63% and 3.53% for the first, second, third and fourth neighboring planes, respectively.

Table 2.1 illustrates the contribution of out-of-plane scattered photons per voxel as a function of the activity ratio of out-of-plane and emission voxel. The number of photons actually emitted by the emission voxel (unscattered photons) and registered by the detector was calculated as: $A_b/4\pi$, where A_b is the activity of the emission voxel "b" (Figure 2-5). When the emission voxel has the same activity as out-of-plane neighboring voxels, the total contribution of scattered photons can be 20.1%. If the activity of out-of-plane voxels increase, then their contribution can reach more than 50% (Table 5.1). Notice that this model does not include attenuation along the path between the emission voxel "b" (Figure 2-5) and the detector. This is because it is assumed that attenuation along this

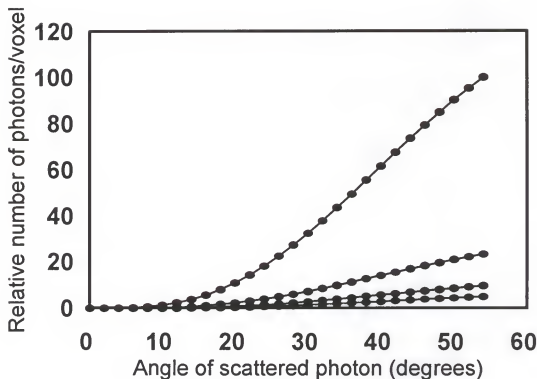


Figure 2-6. Plot of the relative number of out-of-plane scattered photons per voxel as a function of scattering angle. The contributions of the first, second, third and fourth neighbouring planes are represented from the highest to lowest curves, respectively.

Table 2.1

Contribution of out-of-plane scattered photons per voxel as a function of the activity ratio of out-of-plane to emission voxels (ROE) for different neighboring planes. Distance between planes: 0.356 cm.

	ROE = 0.5	ROE = 1.0	ROE = 1.5	ROE = 2.5	ROE = 3.5
First Plane	7.2%	14.3%	21.5%	35.8%	50.1%
Second plane	1.8%	3.6%	5.4%	9.0%	12.6%
Third plane	0.75%	1.8%	2.3%	3.8%	5.3%
Fourth plane	0.35%	0.71%	1.1%	1.8%	2.5%
Total	10.1%	20.1%	30.3%	50.4%	70.5%

path is corrected by the reconstruction process. However, photon attenuation along the path between voxels "a" and "b" (Figure 2-5) is included, because correction methods in SPECT only compensate attenuation along those projection rays which are perpendicular to the detector.

In this model, it was assumed that all out-of-plane neighboring voxels have the same activity A_n . It is obvious that this assumption increases the number of scattered photons in the calculations. However, this approximation could be valid in those situations in which high activity is taken by large organs nearby to the region or organ to be imaged (e.g., the high liver uptake of ^{99m}Tc -labeled radiotracers that is observed in cardiac SPECT studies). Data derived (Table 2.1) from this simple scatter model confirm the significant contribution of out-of-plane

scattered photons and illustrate the need of scatter compensation methods for improving accuracy in SPECT.

Scatter Correction Methods

The main benefit of any scatter correction method is to improve quantitation accuracy by removing those events with inaccurate positional information. Over the last several years a number of technological advances in instrumentation have occurred that reduce scatter (O'Connor et al., 1995a; Case et al., 1996). Major advances have been the improved detector energy resolution, with some systems achieving values of 8% to 10% at 140 KeV (O'Connor et al., 1995a) and the implementation of scatter correction hardware/software on some of the newer SPECT systems (Buvat et al., 1994; Case et al., 1996; Cullom et al., 1996; McCartney et al., 1996).

Scattering correction techniques can be broadly considered into two groups: energy window based methods and restoration based corrections. Energy window based methods estimate the scatter component by using the data of one or more energy windows abutted to the photopeak window. This approach to scatter correction uses the data acquired with energy windows located on the Compton portion of the spectrum to estimate the scatter contribution to the photopeak region. There is a number of procedures for acquiring and processing energy spectral information, but in general the compensation consists of subtracting the estimated scatter component from the photopeak data (Jaszczak et al., 1985; Hademenos et al., 1993). The method was originally proposed by Jaszczak et al. (1985) who reconstructed transaxial slices from a second window on the Compton region (92 to 125 keV for ^{99m}Tc). Next, a fraction of the Compton image (I_s) is subtracted

from the photopeak image (I_{pp}) to obtain the corrected image (I_c)

$$I_c = I_{pp} - k \cdot I_s ,$$

where the factor k is empirically determined for each system and radionuclide. Although the subtraction process could increase the noise, these methods have demonstrated good clinical performance and have been incorporated into many commercial SPECT systems (Case et al., 1996; Cullom et al., 1996; McCartney et al., 1996).

Restoration-based methods attempt to return scattered photons to their original emission sites. They can be divided into two categories: scatter operator based corrections and filtering restoration. The first category is based on modeling the scattering process by a mathematical operator and including it into an iterative reconstruction algorithm (Buvat et al., 1994). Since Compton scattering is a 3-D effect that depends on the position within the medium and the source distribution, exact scatter response functions can be only derived from Monte Carlo calculations (Frey and Tsui, 1991; Buvat et al., 1994). The large memory and extensive computation required for Monte Carlo simulations on each patient make these methods impractical for clinical use. Filtering restoration methods are more easily implemented and do not require extra memory or time for acquiring and processing SPECT data. They compensate the degrading effects of both scatter and detector geometric response, while also decreasing noise (King et al., 1991; Boulfelfel et al., 1992). These methods are based on the deconvolution of SPECT data with a representative point source response function of the imaging system.

Because the ill-conditioned nature of the restoration problem (Andrew & Hunt, 1977, p. 114), a number of different regularization approaches has been developed (Madsen and Park, 1985; King et al., 1991; Boulfelfel et al., 1992). So far, the simplest and most effective methods in SPECT are those that filter the data using the Metz or Wiener filters (King et al., 1991; Boulfelfel et al., 1992). Restoration based methods are discussed in detail in Chapter 3.

Artifacts in the Inferior Myocardial Wall

Two main types of artifacts have been observed in the inferior myocardial wall as consequence of the photon attenuation, scatter, geometric collimator response and high background in abdominal organs. First, the high liver activity in ^{99m}Tc cardiac SPECT studies produces a hypoperfusion artifact in some patients (Johnson et al., 1991; 1994; Matsunari et al., 1996b). The origin of this artifact has been associated with the photon attenuation (King et al., 1995; Nuyts et al., 1995) and the spatial domain negative sidelobes of reconstruction filters (Figure 2-2) (Ljunberg et al., 1994; Zeng et al., 1995). On the other hand, experimental studies (Ljunberg et al., 1994; King et al., 1995) have demonstrated that when photon attenuation is compensated, the hypoperfusion artifact changes to an overcounting artifact in the inferior myocardial wall. This second type of artifact has also been observed in ^{201}Tl studies with high liver uptake of the radiotracer (Case et al., 1996; McCartney et al., 1996).

The Hypoperfusion Myocardial Artifact

This type of artifact is typical of the FBP method when the structure to image is close to a very high activity region. A similar artifact has been observed in SPECT studies of the skeleton where high bladder activity produces very low counts in the hips (Bunker et al., 1990). This is due to the convolution of the very high pixel values with the negative sidelobes of the convolution kernel (Figure 2-2). In theory, a convolution kernel with very narrow sidelobes could solve the problem (Zeng et al., 1995). However, when the negative sidelobes are reduced, blurring is increased. The hypoperfusion artifact can then be eliminated, but an artificial increase of the counts will appear as a consequence of the blurring of the image.

Taking a different point of view, Nuyts et al. (1995) based the origin of the hypoperfusion artifact on the fact that attenuated projection data are inconsistent. According to Chang (1978), inconsistent projection data means that there does not exist any realistic object able to produce such a set of projections in the absence of attenuation. Nuyts et al. (1995) demonstrated that the FBP method does not introduce significant negative values for consistent projections, because the backprojection operator compensates the negative convolved values. They concluded that the main cause of the artifact is the lack of attenuation correction.

The Overcounting or Spillover Artifact

The conclusion of Nuyts et al (1995) have been confirmed by King et al. (1995) in a 3-D simulated anthropomorphic phantom. However, when the projections are corrected for attenuation, a spurious increase or

spillover effect in the number of counts appears in the inferior myocardial wall (Ljunjberg et al., 1994; King et al., 1995). This effect has been mostly attributed to the scattered photons from radioactivity in nearby organs, such as liver and stomach (Case et al., 1996; Maniawski et al., 1996; McCartney et al., 1996). It is known that in cardiac SPECT the most important source of scattered photons is the liver, while the most affected region is the inferior myocardial wall. Also, the position of the lungs make the scatter effect higher around the inferior myocardial wall than in superior regions (McCartney et al., 1996). These observations have indicated that optimal and accurate quantitation of cardiac SPECT requires scatter compensation in addition to attenuation correction. Furthermore, the practical availability of transmission-emission methodologies for accurate nonhomogeneous attenuation correction (Case et al., 1996; Maniawski et al., 1996; McCartney et al., 1996), has signified the overcounting or spillover artifact and renewed the interest for scatter compensation techniques in cardiac SPECT.

CHAPTER 3 THE RESTORATION PROBLEM IN SPECT

Image formation is the process in which an energy source distribution $s(x',y',z')$ is mapped onto a 2-D function $f(x,y)$ which is proportional to the intensity of a physical magnitude, such as density, activity or brightness. The source distribution is called the object or input image, while the resultant function is referred as the degraded or output image. Any image formation system imposes some degrading effects upon the output image, e.g., blurring, sampling artifacts or noise addition. Image restoration attempts to recover the input image from the degraded image by using a priori knowledge of degrading effects. Therefore, restoration methods are based on modeling the image formation system by a degradation operator H which operates on the object $s(x',y',z')$ to produce the output $f(x,y)$

$$f(x,y) = H[s(x',y',z')] , \quad (3.1)$$

where the input image should be recovered by applying an inverse operator.

In deterministic models, the degradation operator H is represented by the point spread function (PSF) of the imaging system. This function describes the response of the system to a point source in the object of interest. The PSF usually is a spatially shift-variant function. This means that the function depends on the position of the point source inside the object. When the source is embedded in a scattering medium, the PSF is

also object dependent (Andrews & Hunt, 1977, p.62). Hence, the PSF can be written as:

$$PSF = h(x', y', z', x, y, s(x', y', z')) . \quad (3.2)$$

Since the resultant image is the superposition of all the individual point source responses, Equation (3.1) becomes:

$$f(x, y) = \iiint h(x', y', z', x, y, s(x', y', z')) dx' dy' dz' .$$

This integral equation represents a nonlinear model with respect to the source distribution. There is no analytical solution for this type of model and it must be approximated to a linear representation in which the inversion process can be performed by using concepts of linear systems theory.

This chapter first introduces the restoration problem in SPECT in the most general and realistic way by using a nonlinear spatially shift-variant degradation model. Next, the assumptions required to approximate this model to a linear spatially shift-variant or invariant representation are described and justified. Also, different practical and experimental approaches to the restoration problem in SPECT are discussed. Finally, the design of the restoration filter and the experimental determination of the representative PSF of the SPECT system used in this work are described.

Degradation Models in SPECT

Nonlinear Shift-Variant Model

In contrast to attenuation that is independent of the source distribution, scattering is affected by the spatial density of the source

(Buvat et al., 1994). No pointwise scattering correction exists because the scatter at one position (x', y', z') depends upon the source distribution at all other positions. The scatter correction has to involve an integral operator rather than a multiplicative operation as those used in attenuation correction (e.g.: Chang's method). Therefore, a realistic degradation model in SPECT has to be nonlinear with respect to the source distribution. In this model, projections $p_\theta(x, y)$ at an angle θ can be represented by

$$p_\theta(x, y) = \iiint h_\theta(x', y', z', x, y, s) \cdot s(x', y', z') dx' dy' dz' + n_\theta(x, y),$$

where $h_\theta(x', y', z', x, y, s)$ is the source dependent PSF of the system at the projection angle θ and $n_\theta(x, y)$ is a Poisson noise component added to the projection data to model the statistical nature of the radioactive disintegration. This integral equation represents a continuous-continuous model because both the projection and the source distribution are continuous functions. However, projections and source distributions in SPECT are sampled and discretized in pixels and voxels, respectively. For practical purposes the continuous-continuous model has to be converted into a discrete-discrete representation

$$P_\theta, x, y = \sum_{x'=1}^{X'} \sum_{y'=1}^{Y'} \sum_{z'=1}^{Z'} h_{\theta, x', y', z', x, y}(s_{x', y', z'}) \cdot s_{x', y', z'} + n_{\theta, x, y},$$

where: $x = 1, 2, \dots, X$ and $y = 1, 2, \dots, Y$, and the number of projection pixels in axis x and y , are X and Y , respectively. The number of pixels of the source distribution in axis x' , y' and z' are X' , Y' and Z' , respectively.

To simplify the notation, the voxel (x', y', z') will be represented by a voxel index r' and the projection pixel (x, y) by a projection index t . Then, the discrete-discrete representation for each projection angle becomes

$$P_{\theta, t} = \sum_{r'=1}^{X'Y'Z'} h_{\theta, r', t}(S_{r'}) \cdot S_{r'} + N_{\theta, t},$$

and the description of the SPECT problem is given by a system of M equations of this type, where M is the number of projection angles. The complete system of equations can be expressed in matricial notation as

$$P = H(S) \cdot S + N,$$

where P is the vector of all projection data measurements with MXY elements. $H(S)$ is a huge ($MXYX'Y'Z'$ elements), nonsparse transfer matrix in which each element is proportional to the probability that a photon emitted by a source voxel r' will be detected by projection pixel t . Vectors of source voxel data and noise component are S and N , respectively.

The transfer matrix $H(S)$ contains a 3-D full description of the PSFs of the system at all projection angles and includes the effects of attenuation, scattering, depth-dependent collimator response and irregular body contour. The solution of the above equation allows simultaneous SPECT reconstruction and corrections for attenuation, photon scatter and collimator geometric response. Because each element of the transfer matrix depends on the source distribution, the well known methods of linear algebra can not be applied to calculate the vector of source voxel data.

In this case, the inverse solution is a very difficult task that must be incorporated into a complex iterative reconstruction scheme. In addition, the transfer matrix consumes an excessive amount of computer memory: 64 GB is required in a typical SPECT study with 60 projections of 64 x 64 pixels, source distribution sampled by 64 x 64 x 32 voxels and 2 bytes per integer word. On the other hand, modeling the transfer matrix $H(S)$ is a very difficult problem which does not have an analytical solution. Despite considerable effort by several investigators (Buvat et al., 1994), a complete and practical solution has not as yet been obtained. The only theoretical possible approach is to simulate by Monte Carlo the transfer matrix for each projection. This requires an extraordinary amount of computer time, that has been estimated at 190 days with the present SPECT computer technology (Frey & Tsui, 1994). Because PSFs are object dependent, the simulation must be repeated for each patient.

The impracticability of the nonlinear model has lead to some approximate assumptions in which the PSF is object independent and spatially shift-variant or invariant (King et al., 1991; Frey & Tsui, 1990; Smith, 1994). These more conventional representations allow one to solve the restoration problem using linear algebra and iterative statistical estimation techniques. Table 3-1 shows the main three different approaches to the restoration problem in SPECT.

Linear Shift-Variant Model

This model assumes that scattering is independent of the source distribution. The physical meaning of this assumption is that the system response to any arbitrary source distribution is equivalent to the linear combination of the response to individual point sources. This

TABLE 3.1

Restoration models in SPECT and their approximate solutions.

Model	Assumptions	Solution
Nonlinear and spatially shift-variant.	PSF is object and position dependent.	There is no practical solution.
Linear and spatially shift-variant.	The PSF is object independent. Source is uniformly distributed or can be approximated by a slowly varying function.	The PSF is parameterized and incorporated into an iterative reconstruction algorithm. The model has only been used in simulated and physical phantoms.
Linear and spatially shift-invariant.	The imaging system is described by a representative PSF. Source is uniformly distributed in a uniform attenuating medium.	Pre- or post- reconstruction filtering restoration with the FBP technique. Applicable in clinical studies.

PSF: Point spread function; FBP: Filtered backprojection

approximation is justified when the source is uniformly distributed, or at least it is a very slowly spatial variant function (Andrews & Hunt, 1977, p. 63) in an isotropic homogeneous medium. The model can be represented by a matrix formulation of the projection of the source onto detection planes (Frey et al., 1993; Frey and Tsui, 1994; Smith, 1994) or in terms of the photon transport theory (Egbert and May, 1980).

Matricial Formulation. In this model the transfer matrix H does not depend on the source distribution. The nonlinear problem has been solved but not the large memory required to store the degrading operator in matricial form. Also, it is necessary to know the PSF for every point and for every projection angle. PSFs have been calculated using Monte Carlo techniques (Floyd et al., 1985) and the results stored in computer memory for use during the reconstruction process. Due to computational limitations, this method have been only applied to very simple geometries and source distributions. This method is impractical for the complex geometries and source distributions found in clinical studies. To reduce the computational burden, Frey and Tsui (1990; 1991) introduced the concept of a parameterized scatter response function. Then, the elements of the transfer matrix can be calculated from analytical functions. These functions were determined for different source locations by fitting Monte Carlo simulated data or experimental measurements to empirical functions composed of a Gaussian plus a pair of half Gaussians with different widths (Frey & Tsui, 1990; 1991; Beckman et al., 1994). They demonstrated that the fitting parameters vary in a systematic manner with the source position in a cylindrical water filled phantom. They also developed a functional description of the scatter response function by parameterizing

the Gaussian functions (Frey & Tsui, 1991). The addition of the parameterized scatter response function to a projector/backprojector iterative reconstruction scheme has demonstrated superior absolute quantitative accuracy compared to compensation for only uniform attenuation and geometric collimator response in simulated cylindrical phantoms (Frey & Tsui, 1993; Frey et al., 1993). The concept of a parameterized scatter response function has been recently extended to nonuniform attenuators by using water equivalent distances instead of geometric distances (Frey & Tsui, 1994).

The use of parameterized scatter response functions eliminates the need for Monte Carlo simulations to determine the transfer matrix and large memory required to store it. One inconvenience of this method is that the parameterized functions have to be determined for each SPECT system, collimator and photon energy. An additional drawback is that direct solution of the model by matrix inversion is not practical due to the large number of matrix elements. The solution requires a projector/backprojector iterative reconstruction technique with its inherent limitations such as the dependence of accuracy on the number of iterations and its lack of application in the clinical routine due to the slow convergence and relatively long processing time.

Smith (1994) proposed an alternative procedure in which scattered photons were compensated using the dual window energy subtraction technique (Chapter 2, p. 44). In this approach, the 3-D problem is approximated by series of coupled 2-D transaxial reconstructions. The source distribution in each transaxial plane is calculated iteratively using a small transfer matrix which only contains the contribution of the

unscattered photons from a small number of nearby planes. Therefore, the size of the transfer matrix and memory requirements are significantly reduced. In each iterative step, the source distribution is estimated by subtracting the contribution of the out-of-plane unscattered photons from the projection data (Smith, 1994). The increase in noise level due to subtraction corrections makes this method unapplicable to the count-limited clinical SPECT data (Smith, 1994).

Photon Transport Theory. In terms of the photon transport theory the problem can be represented as follows: let us assume a stationary process given by a monoenergetic gamma ray isotropic source distributed in a homogeneous and isotropic medium of volume V (Figure 3-1). Then, the integral transport equation can be expressed as the one speed approximation (Duderstadt and Hamilton, 1976, p. 128) given by

$$\phi(r) = \int_V S(r') \cdot K(r, r') \cdot d^3r' + \mu_s \int_V \phi(r') \cdot K(r, r') \cdot d^3r',$$

where $\phi(r)$ is the particle flux (photons/cm².s) at r , μ_s (cm⁻¹) is the Compton attenuation coefficient (Attix, 1986, p. 132) of the medium and $K(r, r')$ is the kernel of the integral which represents the particle flux at r due to a unit strength, monoenergetic, steady and isotropic point source at r' . The above integral equation is a homogeneous Fredholm linear equation of the second kind whose solution is given by the Neumann expansion (Zwillinger, 1996, p. 430)

$$\phi(r) = \int_V S(r') \cdot K(r, r') \cdot d^3r' + \sum_{n=1}^{\infty} \mu_s^n \int_V k_n(r, r') \cdot S(r') \cdot d^3r',$$

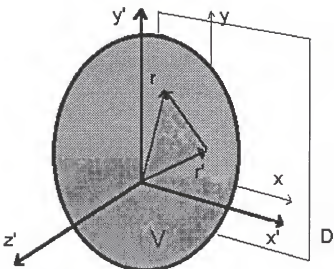


Figure 3-1. Coordinates for source distribution and detection plane D. Shaded area represents the volume V in which the source is distributed.

where

$$K_n(x, x') = \int_V K_{n-1}(x, x') \cdot K(x', x'') \cdot d^3x''$$

for $n = 2, 3, 4, \dots$

and where

$$K_1(x, x') = K(x, x') .$$

The physical meaning of each n -th term is the contribution of the n -times collided photons to the total flux. The first term ($n = 0$) represents the uncollided flux, the second one ($n = 1$) represents the once-scattered photons and so forth. In SPECT studies the narrow energy window around the photopeak ($\pm 10\%$) and the small acceptance angle of the

collimator holes exclude significantly the contribution of more than once-scattered photons. It has been calculated that once-scattered photons constitute more than 90 % of the scattered detected gamma-rays in ^{99m}Tc SPECT studies (Welch et al., 1995). Hence, in the analysis that follows, only first order collisions ($n = 1$) will be considered. Then, the solution of the integral transport equation becomes

$$\Phi(x) = \int_V S(x') \cdot K(x, x') d^3x' + \mu_s \iint_V K(x, x'') \cdot K(x'', x') \cdot S(x') d^3x' d^3x'' ,$$

where the projection $p(x, y)$ of the source distribution onto the detection plane D (Figure 3-1) is obtained from the line integral of the flux along a projection ray normal to the detection plane. If photon attenuation is included, the line integral is the attenuated Radon transform of the flux (Tretiak and Metz, 1980). Expressing the above equation and the attenuated Radon transform in operator notation

$$p(x, y) = RU[S] + RC[S] ,$$

where R is the attenuated Radon transform operator, U and C are integral operators representing the uncollided and once collided flux, respectively. An approximative solution S' can be proposed as

$$S' = GRU[S] ,$$

where G is a pseudoinverse operator which represents the reconstruction process and includes attenuation correction, the Radon inverse transform and collimator geometric response correction. Then, by applying G to the

projection $p(x,y)$

$$S' = G[p(x,y)] - GRU[S]$$

where the first term is the source distribution estimated without scatter correction, while the second term contains the exact source distribution that is unknown. The solution can be approximated by an iterative scheme such that

$$S^0 = 0 ,$$

$$S^1 = G[p(x,y)] ,$$

$$S^2 = G[p(x,y)] - GRC[S^1] ,$$

.....

$$S^j = G[p(x,y)] - GRC[S^{j-1}] ,$$

where S^1 is the reconstruction obtained with the FBP method and corrected for attenuation (e.g., Chang's method), S^2 includes a first order correction for once-scattered photons and so forth. Now, the problem is how to estimate the combined operator GRC and the large computer memory required to store it as an array of elements for each projection angle θ . Any practical solution implies an oversimplification of the model, such as the operator representation by a bi-exponential empirical function (Egbert and May, 1980). This simple model has given good results but only for a small source in the center of a simulated cylindrical water tank.

Linear Shift-Invariant Model

In order to avoid iterative methods and adapt restoration to the clinical setting by using the FBP technique, the PSF has been considered as a 2-D shift-invariant function (Boulfelfel et al., 1992; King et al., 1991). Then, if the axis z' is normal to the detection plane D (Figure 3-1), the discrete-discrete representation for each projection angle becomes:

$$p_{\theta,x,y} = \sum_{x'=1}^{x'} \sum_{y'=1}^{y'} \sum_{z'=1}^{z'} h_{\theta,x',y',x,y} \cdot s_{x',y',z'} + n_{\theta,x,y}$$

Notice that in this model, $h_{\theta,x',y',x,y}$ is depth independent.

Therefore, the above equation can be expressed as

$$p_{\theta,x,y} = \sum_{x'=1}^{x'} \sum_{y'=1}^{y'} h_{\theta,x',y',x,y} \cdot Q_{x',y'} + n_{\theta,x,y}$$

where $Q_{\theta,x',y'}$ is the projection of the source distribution onto the plane x',y' . This is expressed by:

$$Q_{\theta,x',y'} = \sum_{z'=1}^{z'} s_{x',y',z'}$$

Now the PSF has a different meaning from those in the previous models. Rather than an operator representing a full 3-D physical process, the PSF is a mathematical linear operator that maps a 2-D object projection onto a degraded projection. In this model restoration must recover the undegraded or object projection $Q_{\theta,x',y'}$ from the degraded projection $p_{\theta,x,y}$ for each projection angle θ . After that, the source

distribution can be calculated by applying the FBP method (Chapter 2, p. 20) to restored projections $Q_{\theta,x',y'}$. Because the attenuation effect is not included in the PSF, attenuation corrections must be performed before or after reconstruction (Chapter 2, p. 30).

The condition of spatially shift-invariance of the PSF along both directions x' and y' , results in the following property (Andrews and Hunt, 1977, p.70)

$$h_{\theta,x',y',x,y} = h_{\theta,x-x',y-y'} ,$$

where the physical meaning of this relation is that the PSF response at any point in the object depends only on the value at this point and not on the position of the point (Gonzalez and Wintz, 1977, p. 185). Then, the distorted projection becomes:

$$P_{\theta,x,y} = \sum_{x'=1}^{X'} \sum_{y'=1}^{Y'} h_{\theta,x-x',y-y'} \cdot Q_{\theta,x',y'} + n_{\theta,x,y} .$$

It can be assumed that projections are discrete periodic functions with periods X' and Y' in the axis x' and y' , respectively. Then, the double summation in the above equation is the expression of the 2-D discrete convolution of the PSF with the object projection (Andrews and Hunt, 1977, p. 66). The advantage of this representation is that in the Fourier frequency domain, the convolution operation becomes a simple multiplicative operation (Gonzalez and Wintz, 1977, p. 65). By applying the discrete Fourier transform (DFT) and the convolution theorem (Gonzalez and Wintz, 1977, p. 65), the above equation can be expressed in the

frequency domain as

$$P(v_x, v_y) = MTF(v_x, v_y) \cdot Q(v_x, v_y) + N(v_x, v_y) ,$$

where capital letters indicate functions in the frequency domain, v_x and v_y are frequency variables. The function MTF is the modulation transfer function of the imaging system and represents the normalized amplitude of the frequency components of the PSF. This is the representation of the PSF in the spatial frequency domain and is experimentally calculated as the normalized discrete Fourier transform of the PSF (King et al., 1991). In order to simplify the notation, one-dimensional continuous variables will be used in the discussion that follows. The conversion to two-dimensional discrete indices is straightforward.

The main limitation of this model is that no single PSF or $MTF(v)$ can describe the image formation process. The PSF depends on the source-detector distance and the depth of the source in the attenuating medium. However, the assumption of shift-invariance has been experimentally supported by the fact that PSFs, and their corresponding $MTFs(v)$, resulting from either the arithmetic or the geometric mean of conjugate opposing projections are approximately invariant in an uniformly attenuating medium, except near the boundaries of the medium (Larssen, 1980; King et al., 1983; 1987; 1991). King et al. (1991) have shown an experimental procedure for calculating the representative $MTF(v)$ of an imaging system from combined conjugate opposing projections in a uniformly attenuating medium and demonstrated that the function provides a reasonable approximation to a shift-invariant system (King et al., 1991). Figure 3-2 depicts the variations of the PSF with the source-detector

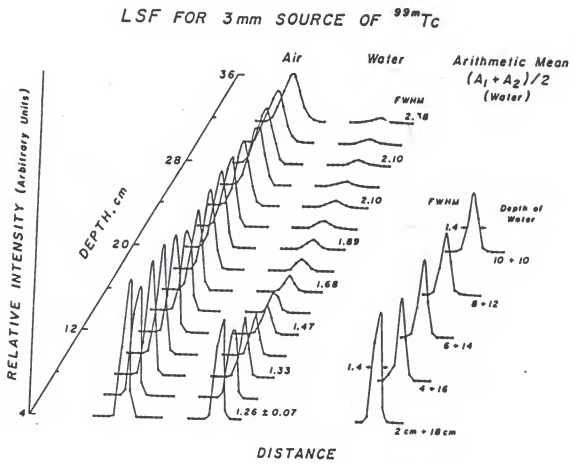


Figure 3-2. Line spread functions (LSF) as a function of the distance from the face of the collimator (depth) in air and in a water tank of 20 cm in diameter. Line spread functions at right correspond to the arithmetic means of conjugate opposed projections with the source in water. Notice that the arithmetic mean of conjugate line spread functions is approximately depth independent (from Cho et al., 1993, p. 175).

distance, the effect of an attenuating medium and the spatial invariance when the PSF is calculated as the arithmetic mean of conjugate opposing projections.

Restoration Filters

In a linear shift-invariant model the restoration problem can formally be expressed in the frequency domain as: given a degraded projection $P(\nu)$, a linear spatially shift-invariant degradation operator $MTF(\nu)$ and the additive noise $N(\nu)$, calculate the original undegraded projection $Q(\nu)$. This problem can only be solved if there exists an unique non-singular inverse operator $MTF^{-1}(\nu)$ such that:

$$MTF^{-1}(\nu) \cdot P(\nu) \approx Q(\nu) .$$

In SPECT systems the PSF can be approximated by the linear combination of two 2-D Gaussians (Nuyts et al., 1993). Consequently, by the properties of the Fourier transform, the $MTF(\nu)$ has a 2-D Gaussian shape and is equivalent to a low-pass frequency filter (Figure 3-3). Since the inverse $MTF^{-1}(\nu)$ is a singular function (for high frequencies $MTF(\nu) \rightarrow 0$ and $MTF^{-1}(\nu) \rightarrow \infty$), there is no solution for the above equation. The physical meaning of this singularity and the absence of an accurate solution is that the power spectrum of the degraded image is restricted by the $MTF(\nu)$ of the image formation system. The higher frequency components of the object were eliminated during the image formation process and then they can not be recovered by restoration of the degraded image. In addition, because of even small amounts of noise, restoration is an ill-conditioned problem. This means that trivial perturbations in $P(\nu)$ (i.e.,

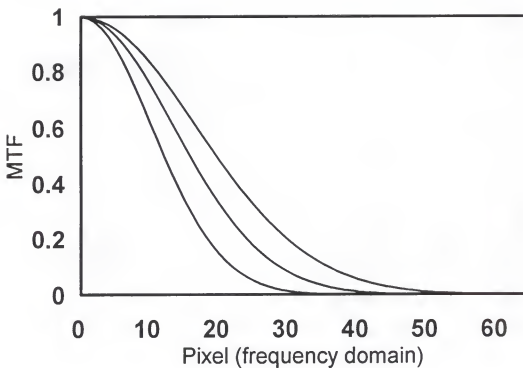


Figure 3-3. Plots of modulation transfer function (MTF) at three different distances from the face of the collimator. Distances are 18 cm, 24 cm and 30 cm from the highest to the lowest plot, respectively.

noise) can produce nontrivial perturbations in the solution (Andrews and Hunt, 1977, p. 114). Also, the presence of noise does not allow an unique solution. If the noise component is non-zero, there is not an unique association between $P(\nu)$ and $Q(\nu)$. Therefore, the object $Q(\nu)$ can only be approximated by a solution $Q'(\nu)$ which satisfies some criterion defined a priori.

A number of restoration approaches has been developed to obtain practical satisfactory solutions (Andrew and Hunt, 1977, p. 114 - 117). So far, the simplest and most effective methods in SPECT are those that use restoration filters instead of the inverse MTF (King et al., 1991; Boulfelfel et al., 1992). The filtering is carried out by multiplying the Fourier transform of the degraded image by a filter function and then Fourier inverse-transforming the result. Restoration filters are band-pass frequency filters which combines the inverse of the representative $MTF(\nu)$ for restoring low frequencies, with a low-pass frequency filter for removing noisy high frequency components. They avoid the singularity of the inverse $MTF(\nu)$ at high frequencies (regularization). In other words, the inverse $MTF(\nu)$ is regularized by a low-pass frequency filter.

Resolution Recovery Filters

In general, any band-pass frequency filter applied to the proper frequency range, produces the amplification of some frequency components which were depressed by the $MTF(\nu)$. Therefore, resolution is partially recovered and the quality of the image improved. Some band-pass frequency filters have been defined by empirical functions such as Gaussians (Madsen and Park, 1985) or their combinations instead of using the inverse $MTF(\nu)$ regularized by low-pass frequency filters. The parameters of Gaussian

functions have to be optimized for each image by means of interactive trials. Because these filters do not require knowledge of the system $MTF(\nu)$, they are considered as resolution recovery rather than restoration filters. A well known filter of this type is the Canterbury filter (Corefield et al., 1975) defined by

$$C(\nu) = G^n(\nu) - K \cdot G^m(\nu) ,$$

where $G(\nu)$ is a Gaussian function and n , m and K filter parameters that must be varied interactively to optimize the resolution recovery. A proper choice of these parameters can improve significantly image resolution. This method was used by Franquiz et al. (1982a; 1982b; 1983) to improve resolution and calculate right ventricular ejection fraction (RVEF) in equilibrium gated radionuclide ventriculography studies (Franquiz et al., 1983). In these studies, the finite detector resolution blurs cardiac structures producing the overlapping of the pulmonary outflow tract with the right ventricle. This is the main difficulty in calculating the RVEF using the equilibrium gated technique (Winzelberg, 1981; Franquiz et al., 1982a). Canterbury filter significantly improved resolution allowing a more accurate calculation of RVEF (Franquiz et al., 1982b). Major disadvantages of this method are the optimization process of filter parameters, that has to be performed by trial-and-error, and the increase in the noise level due to the subtraction operation.

Wiener Filter

Wiener filter is a restoration filter derived from the constrained least-squares regularization approach to the restoration problem (Gonzalez and Wintz, 1977, p. 197). This is a well known and effective method for

obtaining approximate solutions to restoration problems. This method estimates a solution $Q'(\nu)$ which satisfies a criterion of goodness given by the minimization of a quadratic functional defined by

$$J(\nu) = \|P(\nu) - MTF(\nu) \cdot Q'(\nu)\|^2 - \|N(\nu)\|^2 + \lambda \cdot \|C(\nu) \cdot Q'(\nu)\|^2,$$

where $\|\cdot\|$ is the norm, λ is a regularization parameter and $C(\nu)$ is a regularization operator (Galatsanos and Katsaggelos, 1992). By differentiating $J(\nu)$ with respect to $Q'(\nu)$ and setting the result equal to zero, the approximate solution can be calculated from:

$$Q'(\nu) = \frac{MTF(\nu) \cdot P(\nu)}{MTF^2(\nu) + \lambda \cdot C^2(\nu)}.$$

The operator $C(\nu)$ is an increasing function that avoids the singularity of the filter. For high frequencies, $\lambda \cdot C^2(\nu) \gg MTF^2(\nu)$, the filter goes to zero and the noise is suppressed. For low frequencies, when $\nu \rightarrow 0$, then $C(\nu) \rightarrow 0$ and the filter becomes the inverse $MTF(\nu)$. The compromise between inverse restoration and noise suppression is determined by the values of $C(\nu)$ and λ . Both values depend on the noise, $MTF(\nu)$ and the object and degraded images (Galatsanos and Katsaggelos, 1992). The classical Wiener filter (Andrew and Hunt, 1977, p. 151) has been defined by setting $\lambda = 1$ and $C^2(\nu) = N^2(\nu)/Q^2(\nu)$, where $N^2(\nu)$ and $Q^2(\nu)$ are the power spectrum of the noise and the object, respectively. Then, the Wiener filter $W(\nu)$ can be expressed as:

$$W(\nu) = \frac{MTF(\nu)}{MTF^2(\nu) + N^2(\nu)/Q^2(\nu)}.$$

The main inconvenience of this filter is that $N^2(\nu)$ and $Q^2(\nu)$ are unknown functions and must be estimated from the degraded image (Penney et al., 1990). In spite of this drawback, the Wiener filter has demonstrated good performance in deblurring and improving image contrast in physical phantoms and clinical studies (King et al., 1984; Yanch et al., 1988; Penney et al., 1990; Boulfelfel et al., 1992). However, the requirement of estimating the object and noise power spectra for each image, has imposed a real limitation in its practical use.

Metz Filter

The performance of the Metz filter $M(\nu)$ is equivalent to that of Wiener (King et al., 1984; Penney et al., 1990), but with the advantage that is simpler and easier to implement. It is given by the expression

$$M(\nu) = \frac{1 - (1 - MTF^2(\nu))^x}{MTF(\nu)},$$

where the exponent X is a power factor that could depend on the total number of counts in the image (King et al., 1983; 1984) and determines the frequency at which the filter goes to zero amplitude (Figure 3-4). Experimental studies (King et al., 1983; 1987; 1991) have shown that a more convenient filtering, in terms of noise and image quality, has resulted when instead of the representative $MTF(\nu)$ the following generalized exponential function is used

$$E(\nu) = \exp\left(-\frac{\nu^p}{S}\right),$$

where p and S are parameters to be optimized by the minimization of the

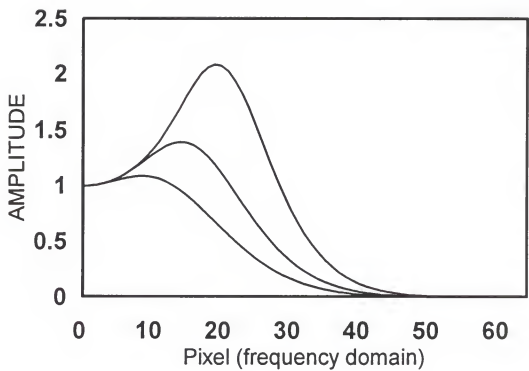


Figure 3-4. Plots of Metz filter for power factors of 10, 4 and 2, from the highest to the lowest curves, respectively.

normalized mean-square error (King et al., 1991) between the restored and object image. Another method (King et al., 1987) for determining p and S uses interactive visual feedback to allow the operator to select the optimal function from among a family of possible optimal filters.

The Metz filter, either with the $MTF(\nu)$ or with the exponential function, has been successfully used for compensating scattering and geometric collimator response in liver-spleen studies (King et al., 1991), cardiac and brain SPECT (Tsui et al., 1994a) and simulated projections of cardiac studies with high liver activity (Franquiz and Shukla, 1996). Tsui et al. (1994b) have reported improved accuracy and better separation between myocardium and the top of the liver by using Metz filter in simulated and clinical ^{201}Tl cardiac SPECT. Although the advantages of Metz filter in terms of easy implementation and favorable results, it has seldom been used in clinical studies most likely due to the lack of a consistent methodology for determining the optimal filter parameters. This is especially important because in a restoration operation results are very sensitive to the parameters of the filter function. As with the Wiener filter, the definition of the Metz filter is image dependent and somewhat arbitrary. The main theoretical inconsistency of the Metz filter is that its roll-off, which is given by the exponential factor X (Figure 3-4), only depends on total image counts (King et al., 1983; 1987; 1991). Since images with very different power spectra can have the same number of total counts, this criterion is not sufficient for determining where the filter amplitude should go to zero. For example, ^{99m}Tc -MDP bone scan and ^{99m}Tc -HMPAO brain projections can have the same number of counts but very different behavior in both the spatial and frequency domain.

Computer Implementation of the Metz Filter

For comparative purposes, conventional restoration of SPECT images was conducted with a Metz filter in this research. It was implemented with the representative $MTF(\nu)$ of the SPECT system. Since restoration filters are 2-D isotropic functions, ν represents the radial spatial frequency given by: $\nu = (\nu_x^2 + \nu_y^2)^{1/2}$, where ν_x and ν_y are the horizontal and vertical spatial frequencies, respectively. All filter algorithms and operations were programmed in MATLAB code (Appendix A). The Filter performance was validated using simulated 2-D myocardium-liver projections blurred by convolution with the experimental PSF for ^{99m}Tc and ^{201}Tl line sources.

Determination of the Modulation Transfer Function

The first step was the experimental determination of analytical expressions for the representative $MTF(\nu)$ of the SPECT system. Modulation transfer functions were determined for the energies of ^{201}Tl and ^{99m}Tc . Also, $MTFs(\nu)$ were determined with the radioactive source in water and in free air. The determination in water includes the influence of scattering and detector geometric response, while the determination in free air only includes the detector influence.

Theory. Modulation transfer functions were calculated using a double Gaussian model for the PSF. Nuyts et al. (1993) have demonstrated that the PSF of a SPECT system can be approximated by:

$$PSF(x, y) = A \cdot \exp\left(-\frac{x^2+y^2}{2S_1^2}\right) + B \cdot \exp\left(-\frac{x^2+y^2}{2S_2^2}\right).$$

In the above equation A, B, S_1 and S_2 are parameters of the Gaussian functions that fit the PSF counts. However, line sources were employed in experimental measurements because they are easier to handle and prepare than point sources. A line spread function (LSF) expression can be easily obtained from a PSF by integrating in one axis

$$LSF(x) = \int_{-\infty}^{\infty} PSF(x, y) dy ,$$

$$LSF(x) = C_1 \cdot \exp\left(-\frac{x^2}{2S_1^2}\right) + C_2 \cdot \exp\left(-\frac{x^2}{2S_2^2}\right) ,$$

where:

$$C_1 = \sqrt{2\pi} \cdot AS_1 ,$$

$$C_2 = \sqrt{2\pi} \cdot BS_2 ,$$

Since PSF and MTF(ν) are 2-D radially symmetric functions, the Fourier transform of the LSF is equivalent to the cross section of the 2-D Fourier transform of the PSF. Then, the MTF(ν) at any radial direction can be obtained from the amplitude normalized to zero frequency of the Fourier transform of LSF(x):

$$FT[LSF(x)] = \sqrt{2\pi} \cdot (C_1 S_1 \cdot \exp(-2(\pi\nu S_1)^2) + C_2 S_2 \cdot \exp(-2(\pi\nu S_2)^2)) .$$

LSF Measurements. Conjugate opposed SPECT projections (128 x 128 pixels) were acquired with capillary sources of 25 cm long filled with approximately 80 MBq of ^{99m}Tc or ^{201}Tl . Sources were positioned at the

center and in the long axis of the phantom used in experiments. This was a circular cross-section phantom of 25 cm in diameter. Acquisitions were performed with a three-headed SPECT system (Trionix Research Laboratories, Inc., Twinsburg, OH) with the high resolution parallel hole and the low energy general purpose collimator for ^{99m}Tc and ^{201}Tl sources, respectively. Line source images were acquired with the same energy window used in clinical and experimental studies. Five million counts were acquired in each image. The distance source-detector was equal to the radius of rotation (24 cm) used in experimental SPECT acquisitions. LSF numerical data were determined from the arithmetic mean of conjugate projections as the counts in a profile line in the x axis crossing the image of the capillary source. Care was taken to align the source along the y axis in the center of the detector field of view. Line spread functions were determined for each detector. The final LSFs were calculated by adding the contribution of each detector.

Curve Fitting. Fitting of LSF parameters to experimental count data was carried out using the nonlinear least squares algorithm of Levenberg-Marquardt (Appendix A.1). Line sources in water were fitted to a double Gaussian model, while sources in free air were fitted to a simple Gaussian function. The χ^2 value between experimental LSF count data and their corresponding fitted functions was calculated as a measure of the goodness of fit.

Results. Table 3.2 presents the PSF and LSF fitting results for ^{99m}Tc and ^{201}Tl line sources in free air and in water. Figure 3-5 shows the experimental LSF counts overlayed with the fitted functions. Table 3.3 gives the calculated analytical expressions for the MTFs(ν) used in this

TABLE 3.2

Line spread function (LSF) and point spread function (PSF) parameters fitted to experimental data from line sources of ^{99m}Tc and ^{201}Tl .

LSF	LFTLAI	LFTLWA	LFTCAI	LFTCWA
C_1	5695	1309	35742	10817
S_1	2.316	2.354	1.519	1.522
B	981	222	9387	2835
C_2	-	119	-	426
S_2	-	12.126	-	8.704
B	-	3.9	-	19.5
FWHM	5.60	5.91	3.62	3.71
FWTM	9.63	12.44	6.37	7.27
χ^2	3.2	3.9	3.9	4.7

LFTLAI: Line source of ^{201}Tl in free air.

LFTLWA: Line source of ^{201}Tl in water.

LFTCAI: Line source of ^{99m}Tc in free air.

LFTCWA: Line source of ^{99m}Tc in water.

A, B and C_i are expressed in relative counts and S_i in number of pixels.

FWHM: Full width at half maximum in pixels.

FWTM: Full width at tenth maximum in pixels.

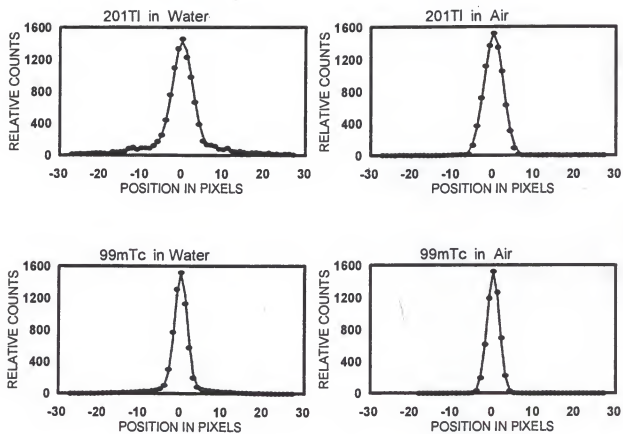


Figure 3-5. Fitted line spread functions (continuous line) and experimental counts (dots). Data obtained with the line source in water were fitted to a double Gaussian model, while data obtained with the line source in air were fitted to a simple Gaussian function.

TABLE 3.3

Analytical expressions of fitted modulation transfer functions.

	Modulation Transfer Function
TLAI	$\exp(-0.00646n^2)$
TLWA	$0.68 \exp(-0.00668n^2) + 0.32 \exp(-0.17721n^2)$
TCAI	$\exp(-0.00278n^2)$
TCWA	$0.82 \exp(-0.00279n^2) + 0.18 \exp(-0.09127n^2)$

TLAI: ^{201}Tl in free air.

TLWA: ^{201}Tl in water.

TCAI: ^{99m}Tc in free air.

TCWA: ^{99m}Tc in water.

n is the radial pixel number in the frequency domain.

research. Figure 3-6 depicts MTFs(ν) functions calculated from the fitted parameters. Results demonstrated that the experimental data were fit very well by the empirical analytical functions. Broader PSFs were observed for ^{201}Tl sources (Figure 3-5). This is due to the lower emission energy, that produces a higher scattering contribution for the source in water, and to the collimator which has lower resolution than that used with the $^{99\text{m}}\text{Tc}$ source. The effect of broader PSFs is to produce MTFs(ν) with lower cutoff frequencies (Figure 3-6), and consequently more blurred and degraded images.

Performance of the Metz Filter

The performance of the Metz filter was assessed in simulated cardiac-liver projections. The optimal power factor of the filter was determined by trial-and-error and based on the visual quality of images and minimization of the normalized mean square error (NMSE) between the filtered image and the original non-degraded object image.

Simulation of Cardiac-Liver Projections. Simulated images were equivalent to the left anterior oblique projection (LAO) at 60 degrees. Images were simulated as frames of 128 x 128 pixels in zoom mode (amplification x 2) and pixel size of 0.356 cm. Simulation included four steps. First, it was simulated the myocardium, second the liver, third the blurring due to scattering and detector geometric response, and fourth the addition of statistical noise.

The myocardium was simulated by the projection in a plane of two concentric paraboloids. The myocardial wall was described by the volume between the two paraboloids with dimensions of:

Myocardial wall : 1.068 cm (3 pixels),

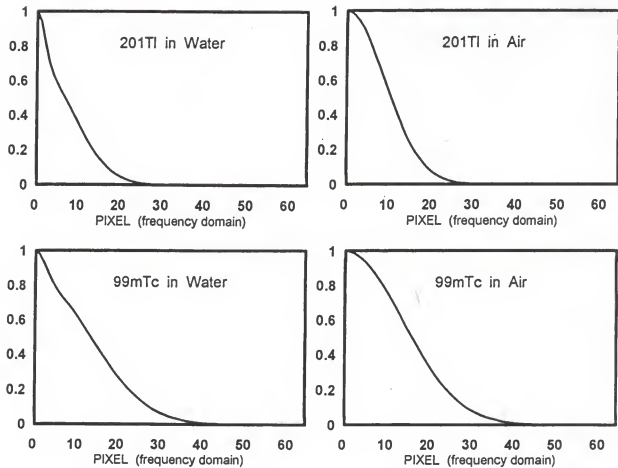


Figure 3-6. Plots of modulation transfer functions calculated from fitted line spread functions. Modulation transfer functions in water include the effects of scattering and detector geometric response, while those calculated in free air only include the effect of the detector geometric response.

Outer paraboloid, long axis (L): 8.2 cm (23 pixels),
Inner paraboloid, short axis (S): 6.05 cm (17 pixels).

The relationship between Y and X dimensions was given by:

$$Y = L - 4 \cdot L \cdot X^2 / S^2 .$$

The simulation was carried out with the MATLAB function heart.m (Appendix A.2). The background was 15% of the myocardium activity.

The liver projection was simulated by a rectangle of 10.3 cm length (29 pixels) separated from the myocardium apex by 1.068 cm (3 pixels). The liver-to-heart activity ratio was 1.5. This was simulated using the MATLAB function liver.m (Appendix A.2). The simulated heart and liver images were added to obtain the ideal projection free of scattering, spatial blurring and noise. This was considered as the object image (Figure 3-7).

The blurring due to scattering and the detector geometric response was obtained from the convolution of the object image with the 2-D PSF determined from the ^{99m}Tc or ^{201}Tl line source. Point spread functions were calculated from the parameters of Table 3.2 and using MATLAB functions psftc.m and psftl.m (Appendix A.2).

Statistical noise was added by the MATLAB function noise.m (Appendix A.2). This function adds the value $\text{RANDN}(a(x,y)^{1/2})$ to each pixel (x,y), where RANDN is a normally distributed random number and a(x,y) the pixel content before adding noise. Images were scaled to myocardial counts of 100 and 50 per pixel. This represents myocardial statistical errors of 10% and 14%, respectively. These noise levels are similar to those encountered in clinical studies.

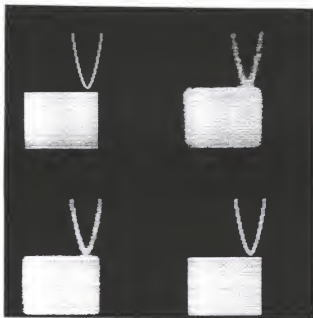


Figure 3-7. Simulated cardiac-liver projection. Top left: Object image without any degrading effect. Top right: Degraded image by convolution with the ^{201}TL point spread function and addition of noise. Bottom left: Degraded image by convolution with the ^{99m}Tc point spread function and addition of noise. Bottom right: Restored image (^{99m}Tc) after Metz filtering with the optimal power factor.

Metz Filtering. Two-dimensional Metz filters were implemented by MATLAB functions tcmetz.m and tlmetz.m (Appendix A.3). The filtering process was performed in the Fourier frequency domain. The 2-D discrete fast Fourier transform of the degraded image was multiplied by the 2-D Metz filter. The restored image was obtained by Fourier inverse-transforming the result (Appendix A.3).

The power factor was initially selected by an interactive visual feedback procedure in which the criterion was the visual quality of restored images. A second fine adjustment was performed based on the minimization of the NMSE calculated from

$$NMSE = \sum_{x=1}^n \sum_{y=1}^n [R(x,y) - O(x,y)]^2 / \sum_{x=1}^n \sum_{y=1}^n O^2(x,y),$$

where $R(x,y)$ and $O(x,y)$ are the restored and object images, respectively. The MATLAB function nmse.m (Appendix A.3) was used for calculating NMSE values.

Results and Discussion

Table 3.4 and Figure 3-8 show NMSE values as a function of the power factor X for ^{99m}Tc and ^{201}Tl projections with different noise levels. Notice that the optimal power factor value depends on the degradation operator (PSF) rather than on the number of counts (Table 3.4 and Figure 3-8). The best restoration was obtained with $X = 4$ for images degraded by the ^{99m}Tc -PSF. This value was independent on the noise level (Table 3.4 and Figure 3-8). Restored images were very blurred when the power factor was below the optimal value, while above this value there was a significant noise increase without further resolution improvement. In contrast, when

Table 3.4

Normalized Mean Square Error (NMSE) as a function of the power factor X
in image restoration using the Metz filter.

X	^{99m}Tc (r.e. = 10%)	^{99m}Tc (r.e. = 14%)	^{201}Tl (r.e. = 10%)	^{201}Tl (r.e. = 14%)
NR	7.198	10.535	8.762	12.357
1	7.583	9.395	10.637	12.920
2	6.212	7.834	8.266	10.281
3	5.928	7.538	7.539	9.430
4	5.878	7.536	7.235	9.058
5	5.901	7.635	7.087	8.876
6	5.954	7.776	7.008	8.787
7	6.020	7.936	6.963	8.748
8	6.093	8.107	6.938	8.740
9	6.168	8.282	6.925	8.752
10	6.245	8.460	6.921	8.777
11	6.323	8.639	6.923	8.811
12	6.401	8.819	6.929	8.853
13	6.480	8.999	6.939	8.900
14	6.557	9.178	6.952	8.951
15	6.634	9.357	6.966	9.006
16	6.711	9.535	6.983	9.063
17	6.786	9.712	7.000	9.123
18	6.861	9.889	7.019	9.184
19	6.935	10.064	7.039	9.246
20	7.009	10.239	7.059	9.310

NR: No restoration; r.e.: Relative statistical error per pixel.

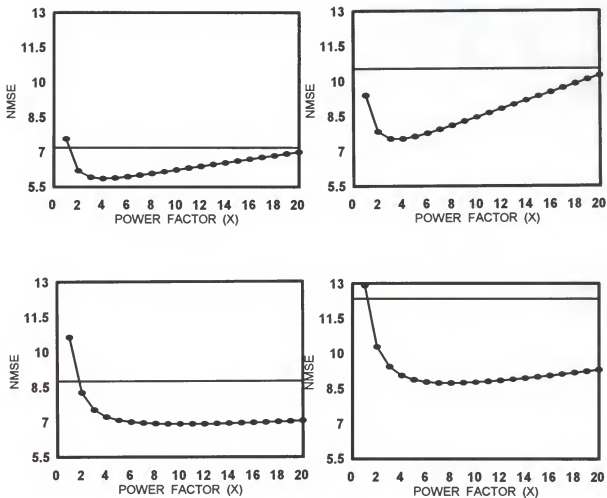


Figure 3-8. Plots of normalized mean square error (NMSE) as a function of Metz power factor X for ^{99m}Tc (top graphs) and ^{201}Tl (bottom graphs) projections with different noise levels. Left graphs correspond to relative statistical error of 10%, while right graphs to relative statistical error of 14%. The horizontal line represents the NMSE value obtained without Metz filtering.

projections were degraded by ^{201}Tl -PSF, optimal restoration was obtained for power factors of $X = 10$ (for 10% statistical error) and $X = 8$ (for 14% statistical error). In these images, power factors higher than the optimal value did not significantly increase the NMSE (Figure 3-8). This can be explained by the flat response of the power spectrum at high spatial frequencies (King et al., 1983) and because in these images most significant image features are contained in the lowest frequency region of the spectrum. It is known that in this frequency region the amplitude of the Metz filter is relatively independent on the power factor X (Figure 3-4). This behavior is significantly different from that of $^{99\text{m}}\text{Tc}$ restored projections in which NMSE values critically depend on the power factor (Figure 3-8). The explanation of this different behavior is given by the fact that $^{99\text{m}}\text{Tc}$ images contain significant features in the intermediate frequency region, where the amplitude of the Metz filter is critically dependent on the power factor (Figure 3-8).

Another important fact is that as the number of count increases more resolution recovery occurs (lower NMSE) (Figure 3-8). By increasing image counts the object can be restored from the blurred noise at higher spatial frequencies without significant amplification of statistical noise. This means that as the number of counts increases, the cutoff frequency can be moved to higher frequencies. However, this effect is not only dependent on the noise level, but also on the image structure and degradation operator (PSF).

Conclusions

Results illustrate the well known fact that Metz filter restoration is image dependent and their parameters (MTF and power factor X) establish

a critical compromise between deblurring and noise suppression. In addition, optimal restoration using Metz filtering has to be determined by trial-and-error or interactive selection of filter parameters by an experienced operator (King et al., 1983; 1987; 1991). These problems are due to the lack of a consistent and general methodology for regularization and denoising in single scale representations where it is difficult to separate noise from image features (Laine et al., 1994). An alternative restoration approach based on multiresolution analysis could overcome these drawbacks. This approach and its application to image restoration in SPECT is presented and discussed in the next Chapter.

CHAPTER 4 MULTIRESOLUTION RESTORATION ALGORITHM

The basic idea of multiresolution analysis is to decompose an image into a coarse approximation or low resolution image and the image details for successive higher spatial resolutions (Vetterli and Kovacevic, 1995, p. 75; Wornell, 1995, pp. 16 - 21). Notice that in this context (multiresolution analysis) spatial resolution means the number of samples or pixels which represent the image. Multiresolution decomposition in the frequency domain is equivalent to dividing the frequency spectrum of the image into a low-pass frequency sub-band image (the coarse approximation) and a set of band-pass sub-band images.

A particular class of multiresolution analysis uses orthonormal wavelet basis or analyzing functions defined in both the space and frequency domain to decompose images into a set of sub-band images of constant frequency bandwidth in a logarithmic scale (Daubechies, 1982, p. 7 - 11; Vetterli and Kovacevic, 1995, p. 69 - 71). Then, spatial resolution varies with frequency allowing higher sampling rates at higher frequencies (Mallat, 1989). The main advantage of this representation is that it provides orthonormal bases whose components have good localization properties in both the spatial and frequency domain. Variations in resolution for each frequency band allow one to "zoom" image details and localize them through a space-frequency representation (Daubechies, 1992, p. 2-7). In other words, this representation provides the spatial location

of the frequency components for each frequency band (Mallat, 1989).

This dual representation has been demonstrated to be a powerful methodology for image analysis and processing (Laine et al., 1994; 1995; Healy et al., 1995; Qian et al., 1995; Sahiner and Yagle, 1995). One particular application has been the denoising of images while keeping or amplifying their significant details at high frequencies (Healy et al., 1995; Laine et al., 1995; Sahiner and Yagle, 1995). It is known that the high frequency content of images is a combination of local features, such as edges, and noise. In a conventional single-scale representation, noise is reduced by using a linear, spatially invariant low-pass filter. This operation also eliminates those high frequency components which correspond to significant image features. Because in some situations high-frequency details are important, their elimination by low-pass filtering may be unacceptable. The dual space-frequency multiresolution representation provides an improved scheme for noise removal by using spatially-adaptive operations in each frequency band (Laine et al., 1995). These spatially located operators eliminate noise while preserving image details at high frequencies (Sahiner and Yagle, 1995).

Requirements for noise removal in SPECT data are much more simple than those in high resolution images, such as mammography, CT or MRI scans (Laine et al., 1995; Sahiner and Yagle, 1995). Nuclear medicine images are low resolution images in which the most significant features are in low and intermediate scale levels, while the noise is located in high frequency channels. This suggests a simple denoising and restoration procedure by simply discarding channels of high frequency and performing the deconvolution restoration in low and intermediate channels where the

inverse operator (MTF^{-1}) is nonsingular. This denoising and restoration approach has been proposed by Wang et al. (1995) and applied by Qian and Clarke (1996) for restoration of images of beta emitters (^{32}P and ^{90}Y) obtained by bremsstrahlung detection with a gamma camera.

The strategy of Wang et al. (1995) and Qian and Clarke (1996) was adopted in this research for developing a multiresolution restoration algorithm in cardiac SPECT. This chapter describes the criteria and methods used to develop the algorithm. The chapter is organized into three parts. The first part presents a concise overview of the wavelet multiresolution representation and its relationship to conventional spatial-frequency representations based on the short-time Fourier transform (STFT). The second part describes the multiresolution algorithm used in this research and the criteria employed for SPECT restoration. In the third part, the multiresolution algorithm is critically assessed in a simulated cardiac-liver projection and compared with the results derived from conventional Metz restoration (Chapter 3, p. 82). To avoid complicated notation, all theoretical analyses are performed for functions of one variable. Thus, one-dimensional functions are referred as the "image". The extension of the analysis that follows to two dimensions is straightforward.

Wavelet Multiresolution Representation

Image representation based solely on spatial variables do not provide information about the frequency spectrum. On the other hand, representations based solely on the frequency spectrum do not provide information on the spatial location of significant image features. Space-

frequency representation is an attempt to combine the advantages of representations in both domains. The conventional method for space-frequency (or time-frequency) representation is based on the STFT, which for a continuous function $f(x)$ is defined as (Daubechies, 1992, p. 2)

$$STFT(v, nb) = \int W(x-nb) \cdot f(x) \cdot \exp(-ivx) \cdot dx ,$$

where $i = (-1)^{1/2}$, v is the frequency variable, nb is the space variable ($n = 1, 2, 3, \dots$), $b > 0$ is the sampling period or translation in the spatial domain, and $W(x)$ is called the analysis filter or the analysis window. When $W(x)$ is a Gaussian function the STFT is called Gabor transform.

To calculate STFT for a given value of x , the function $f(x)$ is first windowed with a translated version of $W(x)$ and then the Fourier transform is calculated. Thus, the Fourier content of each value x is specified or determined by the position of $W(x)$ on $f(x)$. Changing n the window is shifted by steps of b allowing to explore all the space in which $f(x)$ is defined. Therefore, the STFT provides a space-frequency representation or spectrogram of $f(x)$. This representation has been used in different applications, including texture analysis and image compression (Laine et al., 1994; Sahiner and Yagle, 1995). One limitation of this method is that both spatial and frequency resolutions remain constant. Then, if the image has significant features of very different sizes there is not an optimal resolution for analyzing the whole image (Mallat, 1989). Also, the frequency information provided by STFT is not entirely local within each spatial interval. This means that in each windowed interval, $f(x)$ is

decomposed into the same cosine waves (or frequencies) and only their amplitude changes from one segment to another (Daubechies, 1992, p. 2-4). Notice that in this representation frequencies are specified by the Fourier transform. In summary, the STFT is better adequate for analyzing images where all significant features appear or can be approximated at the same scale.

The Wavelet Transform

The wavelet transform provides a similar spatial-frequency representation but with two main differences. The first is that no Fourier transform is required. Instead of infinite cosine waves, the new basis functions are small finite waves, named wavelets, which come from dilatations and translations of a function called the "mother wavelet". The second difference is that analyzing functions, or wavelets, have the spatial resolution matched with their frequency. This means that high frequency analyzing functions are very narrow (high spatial resolution), while low frequency analyzing functions are much broader (low spatial resolution). As a result, the wavelet transform is more adequate than the STFT to "zoom" into significant features of an image and represent them locally (Daubechies, 1992, p. 3; Laine et al., 1994). Similarly to the STFT, the wavelet transform (WT) is given by

$$WT[f(x)] = \langle \Psi_{m,n}(x), f(x) \rangle = |a^m|^{-1/2} \cdot \int \Psi\left(\frac{x-n.b.a^m}{a^m}\right) \cdot f(x) \cdot dx,$$

where $a > 0$, $b > 0$, m and n are integers, $|a^m|^{-1/2}\psi((x-n.b.a^m)/a^m)$ is the wavelet and $\langle \cdot, \cdot \rangle$ denotes the inner product of two functions (Mallat, 1989). Notice that a^m is a scaling factor responsible for wavelet

dilatations, while n corresponds to the spatial location of the wavelet. When $a = 2$ and $b = 1$, some special functions $\psi(x)$ constitute the "mother wavelet" of a complete orthonormal wavelet basis for the space of square integrable functions $L^2(\mathbb{R})$, where \mathbb{R} is the set of real numbers (Daubechies, 1992, p. 10). These particular functions ($a = 2$ and $b = 1$) are called dyadic wavelets and have been adopted for multiresolution analysis because some of them can produce simple orthonormal basis for decomposition of images. Dyadic wavelet coefficients are expressed as:

$$\langle \psi_{m,n}(x), f(x) \rangle = 2^{-\frac{m}{2}} \int \psi(2^{-m}x - n) f(x) dx .$$

The effect of dilatations and translations in the generation of wavelets from their mother function can be illustrated with the so-called "mexican hat" function given by: $\psi(x) = (1 - x^2) \cdot \exp(-x^2/2)$. This function, which is well localized in both space and frequency domain (Daubechies, 1992, p. 3), generates a set of dyadic wavelets given by:

$$\psi_{m,n}(x) = 2^{-\frac{m}{2}} (1 - (\frac{x}{2^m} - n)^2) \cdot \exp(-(\frac{x}{2^{m+1}} - \frac{n}{2})^2) .$$

Figure 4-1 shows the dilatations and translation of wavelets for different values of m and n . Notice that high frequency wavelets (narrower width) are obtained for $m < 0$, while low frequency wavelets (broader width) for $m > 0$. The spatial resolution of the original signal is obtained for $m = 0$. Dyadic wavelets derived from the "mexican hat" function do not constitute an orthogonal basis. However, other dyadic wavelets such as Meyer and Lemarie wavelets (Daubechies, 1992, p. 14 - 15) constitute complete orthonormal basis in $L^2(\mathbb{R})$.

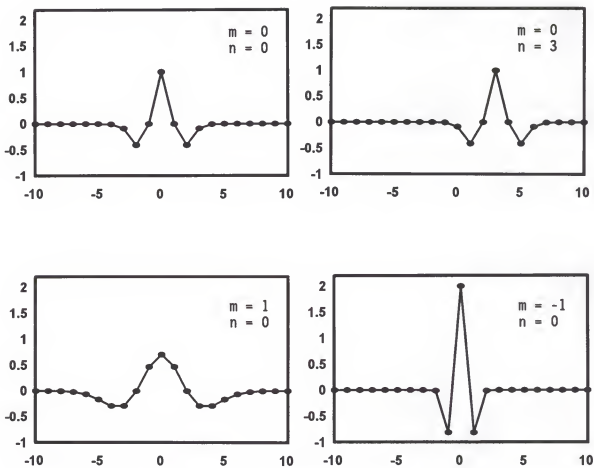


Figure 4-1. The "mexican hat" function (upper left) and its translations and dilatations (wavelets). Upper right graph shows a function translation ($m = 0$, $n = 3$). Bottom graphs show how dilatations induce low ($m = 1$) and high ($m = -1$) frequency wavelets. The resolution of the original function is obtained for $m = 0$.

Thus, any function $f(x) \in L^2(\mathbb{R})$ can be represented by the classical expansion formula of a vector into an orthonormal basis (Vetterli and Kovacevic, 1995, p. 3 - 5)

$$f(x) = \sum_{m=1}^{\infty} \sum_{n=-\infty}^{\infty} \langle \psi_{m,n}(x), f(x) \rangle \cdot \psi_{m,n}(x) , \quad (4.1)$$

where this is equivalent to the inverse wavelet transform (WT^{-1}), which is given by

$$f(x) = WT^{-1}[WT[f(x)]] = \sum_{m=1}^{\infty} \sum_{n=-\infty}^{\infty} \langle \psi_{m,n}(x), f(x) \rangle \cdot \psi_{m,n}(x) .$$

Wavelet basis induce an orthogonal decomposition of $L^2(\mathbb{R})$, such that:
 $L^2(\mathbb{R}) = \dots \oplus W_2 \oplus W_1 \oplus W_0 \oplus W_1 \oplus W_2 \oplus \dots$, where W_m is the vectorial subspace spanned by $\{\psi_{m,n}(x)\}$ and \oplus is the direct sum of subspaces (Vetterli and Kovacevic, 1995, p. 21). Notice that Equation (4.1) requires an infinite number of m terms to achieve perfect reconstruction of $f(x)$. Because this is not practical, Mallat (1989) has demonstrated that $f(x)$ can be represented by a finite number of terms when a scaling function or "father wavelet" $\phi(x)$ is introduced. The relationship between $\phi(x)$ and $\psi(x)$ has been rigorously formulated by Mallat (1989). The dyadic dilatations and translations $\phi_{m,n}(x)$ of the scaling function $\phi(x)$ constitute orthonormal basis in $L^2(\mathbb{R})$ and yield a nested chain of closed vectorial subspaces $\{V_m \mid m \in \mathbb{Z}\}$ which have the properties of containment, given by

$$\dots V_2 \subset V_1 \subset V_0 \subset V_{-1} \subset V_{-2} \dots ,$$

and completeness, expressed as

$$\bigcap_{m \in \mathbb{Z}} V_m = \{0\} \quad \bigcup_{m \in \mathbb{Z}} V_m = L^2(\mathbb{R}) ,$$

where V_m is the subspace spanned by $\{\phi_{m,n}(x)\}$. The property of containment implies that the vectorial projection of $f(x)$ into a subspace V_{m-1} contains all the necessary information to compute the vectorial projection of $f(x)$ at the subspace V_m . The scaling function $\phi(x)$ is related to the mother wavelet $\psi(x)$ such that W_m is the orthonormal complement of V_m in V_{m-1} (Mallat, 1989). This is represented as:

$$V_{m-1} = V_m \oplus W_m .$$

Since $V_m \subset V_{m-1}$ and $W_m \subset V_{m-1}$, the basis functions $\{\phi_{m,n}(x)\}$ and $\{\psi_{m,n}(x)\}$ of V_m and W_m , respectively, must be linear combinations of $\{\phi_{l,n}(x)\}$, which are the basis functions of V_{m-1} . Therefore, the vectorial projection or approximation of $f(x)$ in a subspace V_l is given by

$$f(x)|_{l-1} = A_{l-1} f(x) = \sum_{n=-\infty}^{\infty} \langle \phi_{l-1,n}(x), f(x) \rangle \cdot \phi_{l-1,n}(x) ,$$

where A_{l-1} is the approximation operator (Mallat, 1989). From the relations among V_l , V_i and W_i , the above equation can be written as

$$A_{l-1} f(x) = \sum_{n=-\infty}^{\infty} \langle \phi_{l,n}(x), f(x) \rangle \cdot \phi_{l,n}(x) + \sum_{n=-\infty}^{\infty} \langle \psi_{l,n}(x), f(x) \rangle \cdot \psi_{l,n}(x) ,$$

where in the case of a more general decomposition, the approximation of $f(x)$ in the subspace V_{l-k} is expressed as:

$$A_{l-k}f(x) = \sum_{n=-\infty}^{\infty} \langle \phi_{l,n}(x), f(x) \rangle \cdot \phi_{l,n}(x) + \sum_{m=1}^l \sum_{n=-\infty}^{\infty} \langle \psi_{m,n}(x), f(x) \rangle \cdot \psi_{m,n}(x)$$

Based on these results, the decomposition of $f(x)$ in the subspace V_0 can be represented as

$$\begin{aligned} f(x) &= \sum_{n=-\infty}^{\infty} \langle \phi_{l,n}(x), f(x) \rangle \cdot \phi_{l,n}(x) + \sum_{m=1}^l \sum_{n=-\infty}^{\infty} \langle \psi_{m,n}(x), f(x) \rangle \cdot \psi_{m,n}(x) \\ f(x) &= A_l f(x) + \sum_{m=1}^l D_m f(x), \end{aligned} \quad (4.2)$$

where $D_m f(x)$ is the approximation of $f(x)$ in the subspace W_m .

Equation (4.2) gives the mathematical description of wavelet multiresolution decomposition. Notice that each subspace V_m corresponds to the representation of the original function at a resolution 2^m . Also, the approximation $D_m f(x)$ is the vectorial projection of $f(x)$ on the orthogonal complement of V_{m-1} in V_m . This means that $D_m f(x)$ contains the difference of information between the approximations of $f(x)$ at V_{m-1} and V_m , or in other words, $D_m f(x)$ contains the difference of information between spatial resolutions 2^{m+1} and 2^m . This difference of information is called the detail image at resolution 2^{m+1} (Mallat, 1989). Consequently, Equation (4.2) represents the basic idea of multiresolution analysis (p. 87) which is to decompose an image into a coarse approximation or low resolution image ($A_l f(x)$) and the image details ($D_m f(x)$) for successive higher spatial resolutions ($m = 1, 2, \dots, l$). The coarse approximation provides the general context of the image and

concentrates most of its information while finer features are included in the detail images at higher resolutions. The number of resolution levels in the decomposition is given by l and the sequence of vector spaces V_m is called a multiresolution approximation of $L^2(\mathbb{R})$ (Mallat, 1989).

Wavelet Decomposition in Two Dimensions

The analysis described above can be easily extended from one to two dimensions. However, two-dimensional wavelets can be separable functions given by the product of two one-dimensional functions along the x and y axes, such that $\phi(x,y) = \phi(x).\phi(y)$ and $\psi(x,y) = \psi(x).\psi(y)$ (Mallat, 1989). Therefore, images can be decomposed not only in resolution levels but also in orientation levels (Laine et al., 1994). This property have been extensively exploited in image enhancement and recognition of structures (Laine et al., 1994; 1995). However, because this property is not relevant to this research, only isotropic non-separable wavelets will be considered.

The Filter Bank Interpretation

A useful and practical interpretation of wavelet multiresolution analysis is in terms of a filter bank decomposition (Daubechies, 1992, p. 156 - 166). The basic objective of filter bank decomposition is to separate the image into uncorrelated frequency sub-bands by using a cascade of analyzing pass-band filters. The output of each pass-band filter is an estimate of the frequency content of the image at the corresponding frequency band. Sub-band frequency images are recombined by a set of synthesis filters to generate an approximation of the original image (Vetterli and Kovacevic, 1995, p. 92 - 95). Analysis/synthesis filter

banks satisfy the condition of perfect reconstruction when analysis and synthesis filters are matched by equivalent operations to yield an output image identical to the input. The objective of the filter bank is not to just decompose and reconstruct images, but to do some enhancement or compression operations between the decomposition and reconstruction stages.

If in addition to sub-band filter decomposition the analysis impulse response functions are localized in space, then the sequence of filter outputs gives the spatial content of the frequency bands. In this case Mallat (1989) demonstrated the connection between wavelet multiresolution and filter bank decomposition. The "mother wavelet" $\psi(x)$ is the impulse response function of a band-pass frequency filter and its dilatations and translations $\psi_{m,n}(x)$ correspond to impulse functions of spatial localized band-pass filters. Similarly, the scaling function $\phi(x)$ is the impulse response function of a low-pass frequency filter and its dilatations and translations $\phi_{m,n}(x)$ generate a sequence of low-pass frequency filters (Mallat, 1989). Consequently, the coarse approximation corresponds to a low-pass frequency image, while detail images correspond to band-pass frequency sub-band images. This can be interpreted in terms of an analysis and synthesis filter bank (Wornell, 1995, p. 14 - 16) where the wavelet transform and its inverse correspond to the analysis and synthesis operations, respectively (Laine et al., 1994). A practical advantage of this interpretation is that multiresolution representation by wavelet expansion can be easily implemented by a filtering operation in the frequency domain instead of image decomposition by wavelet inner products (Laine et al., 1994). In this investigation the analysis/synthesis filter

bank approach was followed for multiresolution decomposition of images.

Multiresolution Restoration

Multiresolution decomposition was achieved using a formulation introduced by Laine et al. (1994) to implement the 2-D Frazier-Javerth transform (Frazier et al., 1991, p. 51 - 60) by an isotropic analysis/synthesis filter bank. This constitutes a set of equivalent analysis and synthesis filters which are radially symmetric and allow perfect reconstruction (Laine et al., 1994). Analysis functions in the frequency domain for a 1-level multiresolution decomposition are given by:

For $2 < m < 1-1$ and $2^m\nu_N \leq \nu \leq 2^{(m-2)}\nu_N$:

$$F_m(\nu) = [0.5(1-\cos(\pi\log_2(2^{m-2}\nu/\nu_N)))]^{1/2},$$

otherwise:

$$F_m(\nu) = 0,$$

for $m = 1$ (coarse approximation) and $2^1\nu_N \leq \nu \leq \nu_N$:

$$F_1(\nu) = [1-F_2^2(\nu)]^{1/2},$$

otherwise:

$$F_1(\nu) = 0,$$

for $m = 1$ and $0 \leq \nu \leq 2^{(0-2)}\nu_N$:

$$F_1(\nu) = [1-F_{l-1}^2(\nu)]^{1/2},$$

otherwise:

$$F_1(\nu) = 0,$$

where $F_m(\nu)$ is the analyzing function, ν is the radial frequency and ν_N is the Nyquist frequency of the input image. The analyzing functions satisfy

the following identity

$$\sum_{m=1}^l F_m^2(v) = 1 ,$$

which is valid for all orthonormal wavelet bases (Wornell, 1995, p. 16).

Figure 4-2 shows the amplitude of analyzing functions in the frequency domain for five resolution levels ($l = 5$). From the above equations and Figure 4-2, it is evident that frequency channels have constant bandwidth on a logarithmic scale. Also notice that broader bandwidths are in the high frequency region (higher resolution at higher frequencies). The redundancy or overlapping between bandwidths (Figure 4-2) is a requirement to avoid aliasing and rim artifacts and to allow perfect reconstruction (Wornell, 1995, p. 13). From this formulation, the wavelet coefficient of the sub-band image in the frequency domain at the m -th resolution level $f_m(v)$ can be obtained from:

$$f_m(v) = F_m(v) \cdot FT[f(x)] ,$$

where $FT[f(x)] = f(v)$ is the Fourier transform of the input image. The sub-band image in the spatial domain is simply obtained by inverse Fourier-transforming the result of the above equation. This can be easily implemented using discrete Fourier transform (DFT) techniques. Two-dimensional analyzing functions (Figure 4-2) were generated using the program mphys.c which was written by Prof. Andrew Laine from the Department of Computer and Information Sciences, University of Florida.

For illustrative and comparative purposes, Figures 4-3 and 4-4 show the multiresolution decomposition of two different clinical images.

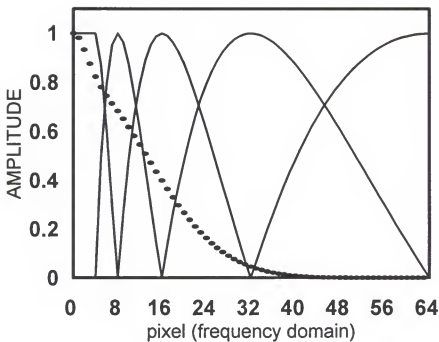


Figure 4-2. Frequency response of analyzing functions (continuous lines) and modulation transfer function (dotted line). Analyzing functions yield a multiresolution decomposition with five resolution levels. Notice that the first analyzing function is a low-pass frequency filter (coarse approximation) and the others are band-pass frequency filters.

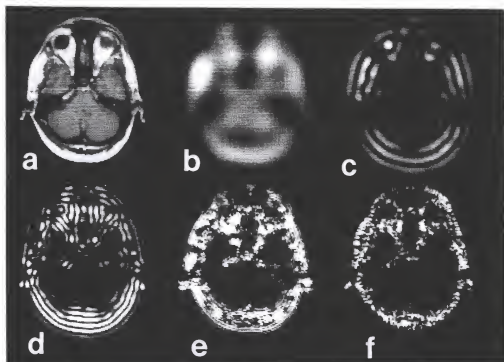


Figure 4-3. Multiresolution decomposition of a high resolution MRI brain image into 5 resolution levels. a: MRI brain image; b: Coarse approximation; c to f: Image details. Notice that all sub-band images contain image features, even the last two noisy sub-band images. Although pixels contain negative and positive values, this figure only depicts absolute values.

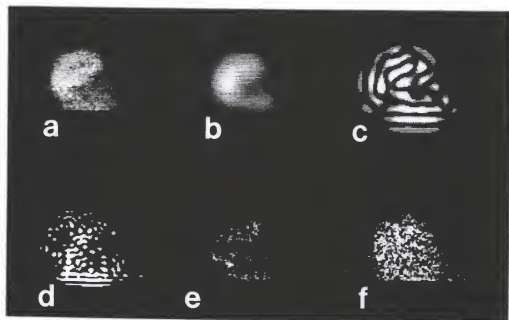


Figure 4-4. Multiresolution decomposition of a low resolution clinical brain SPECT projection into 5 resolution levels. a: Brain SPECT projection; b: Coarse approximation; c to f: Image details. Notice that significant image features are contained in the first three sub-band images. The last two sub-band images only contain noise. Although pixels contain negative and positive values, this figure only depicts absolute values.

Figure 4-3 shows the decomposition of a high resolution MRI brain image, while Figure 4-4 shows the decomposition of a low resolution brain SPECT projection. Notice that the high resolution image (Figure 4-3) contains significant details in the five sub-band images, while the low resolution image (Figure 4-4) contains significant details only in the first three sub-bands. These decompositions were performed using the program `decomp.m` (Appendix B.1).

The Restoration Algorithm

Wang et al. (1995) developed a general wavelet description of the restoration problem. This includes the relationship among wavelet representations of undegraded and blurred images, noise and a linear degrading operator. The formulation of Wang et al. (1995) uses inner products to obtain a matricial equation of the wavelet coefficients of the restored image. Since the restoration problem in SPECT can be reduced to a scalar equation in the frequency domain (Chapter 3, p. 61 - 62), a more simple representation can be achieved by using sub-band analyzing functions rather than wavelet inner products. Then, the formulation of Wang et al. (1995) can be reduced in the frequency domain to

$$P_m(\nu) = MTF(\nu) \cdot F_m(\nu) \cdot P(\nu) + F_m(\nu) \cdot N(\nu) ,$$

where $P_m(\nu)$ is the m -th sub-band image of the blurred SPECT projection, $P(\nu)$ is the undegraded SPECT projection and $N(\nu)$ is the noise. Because the analysis and synthesis functions of the filter bank are equivalent, the reconstructed blurred projection $P_B(\nu)$ (inverse wavelet transform) can be expressed as:

$$P_B(v) = \sum_{m=1}^l MTF(v) \cdot F_m^2(v) \cdot P(v) + \sum_{m=1}^l F_m^2(v) \cdot N(v) .$$

High frequency sub-bands of SPECT projections contain only noise (Figure 4-4). Therefore, high frequency sub-bands can be discarded and the restoration performed in low and intermediate channels where the inverse operator ($MTF(v)^{-1}$) is nonsingular (Figure 4-2). Then, the restored projection $P_R(v)$ is calculated from:

$$P_R(v) = MTF^{-1}(v) \cdot \sum_{m=1}^k MTF(v) \cdot F_m^2(v) \cdot P(v) ,$$

where $k < l$. The final restored projection $P_R(x)$ in the spatial domain is obtained by Fourier inverse-transforming $P_R(v)$.

Now the problem is how to identify the noisy sub-band channels from those containing significant image details. Denoising is a difficult problem that has been approached in multiresolution analysis by using different empirical criteria (Donoho, 1993; Healy et al., 1995; Laine et al., 1995; Sahiner and Yagle, 1995; Qian and Clarke, 1996). Methods based on nonlinear wavelet shrinkage and adaptive empirical thresholding have been used to segmentate noise from significant image details at high frequencies (Donoho, 1993; Laine et al., 1995). Nonlinear wavelet shrinkage, which was proposed by Donoho (1993), reduces wavelet coefficient values toward zero based on a resolution level-dependent threshold (Donoho, 1993; Laine et al., 1995). Other denoising algorithms have used gradient thresholds (Healy et al., 1995) or spatially adaptive mask based on resolution level-dependent thresholds (Sahiner and Yagle, 1995).

In the particular case of low resolution images (Figure 4-4) denoising methods can be simpler. Qian and Clarke (1996) proposed an empirical denoising criterion based on the values of the l_1 norm of sub-band images followed by a multi-channel correlation function. Those sub-band images in which these values were significantly smaller than others were considered as noise and abandoned (Qian and Clark, 1995). A similar denosing method has been used in this research. However, instead of the l_1 norm it was calculated the square l_2 norm (Vetterli and Kovacevic, 1995, p. 28) of each sub-band image of the blurred projection and the PSF of the system. Notice that the PSF is equivalent to the MTF in the spatial domain (Chapter 3, p. 62). The square l_2 norm of a discrete function $f(x_i)$ is calculated as:

$$\|f(x_i)\|_2^2 = \sum_i |f(x_i)|^2 .$$

Those sub-band channels in which the square l_2 norm of both the blurred projection and the PSF were below 2% of the total square l_2 norm of the blurred projection and PSF, respectively, were considered as noise and discarded. Also, those sub-bands in which the square l_2 norm of the PSF decomposition was below 0.2% of its total value, were discarded. These empirical criteria were derived from the observation of SPECT sub-band images (Figure 4-4) and their square l_2 values (Figure 4-5). Figure 4-5 shows the square l_2 norm values of the PSF for ^{99m}Tc and ^{201}Tl , as well as those of different types of SPECT projections.

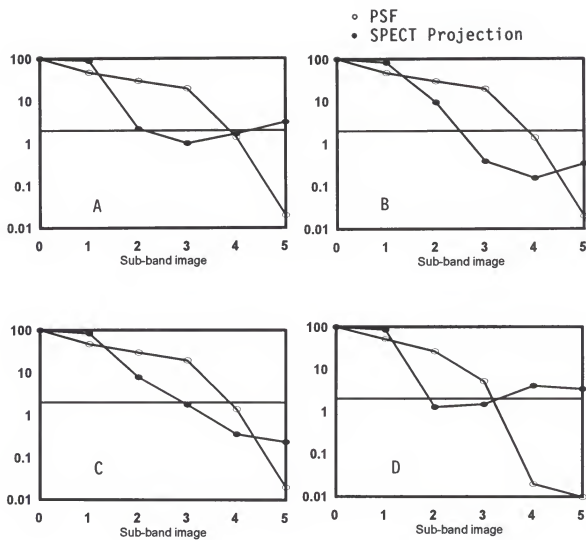


Figure 4-5. Square l_2 norm expressed in percent as a function of the sub-band image m . The input image corresponds to $m = 0$, the coarse approximation to $m = 1$ and the detail images to m values from 2 to 5. The horizontal line shows the threshold level (2%) used to segmentate noise from image details. A: Brain SPECT projection from a clinical study with ^{99m}Tc ; B: Renal phantom SPECT projection (^{99m}Tc); C: Cardiac phantom SPECT projection (^{99m}Tc); D: Myocardial SPECT projection from a clinical study with ^{201}Tl .

Notice how the empirical criterion described above is satisfied by different types of low resolution images and gamma energies. According to this criterion, only first three sub-bands are used in the restoration process (Figures 4-4 and 4-5). The last two sub-bands which correspond to noise are discarded (Figure 4-4). Notice that the number of sub-bands with significant image details depends on the analyzing filters and number of resolution levels used in the decomposition. Results obtained with this particular set of analyzing functions and number of resolution levels can not be extrapolated to other experimental conditions.

Computer Implementation

Multiresolution restoration was accomplished by using the programs invtc.m and invtl.m for ^{99m}Tc and ^{201}Tl images, respectively (Appendix B.2). All operations were performed in the Fourier domain. The final restored image was obtained by Fourier inverse-transforming the result. In order to avoid rim artifacts due to the fast decrease toward zero amplitude of the last analyzing function (Figure 4-2), a filter stability approach was included (Galatsanos et al., 1992; Wang et al., 1995; Qian and Clarke, 1996). Then, the multiresolution restoration algorithm ($MR(\nu)$) was expressed as

$$MR(\nu) = MTF(\nu) \cdot \sum_{m=1}^3 \frac{F_m^2}{MTF^2(\nu) + \lambda_m \cdot Q^2(\nu)} ,$$

where λ_m is a regularizing parameter (Galatsanos et al., 1992) and $Q(\nu)$ is a smoothness constraint operator. The best algorithm performance was obtained for $Q(\nu) = \exp(0.05\nu)$, $\lambda_1 = \lambda_2 = 0$ and $\lambda_3 = 0.005$.

Assessment in Simulated Data

The performance of the multiresolution restoration algorithm was evaluated using the simulated cardiac-liver projection described in Chapter 3 (p. 78) with the highest level of noise. It was calculated the NMSE (Chapter 3, p. 82) and the full width at half maximum (FWHM) of the myocardial wall. Results were compared with those of the blurred image and restoration by Metz filtering.

Analysis of the NMSE showed that multiresolution restoration results were comparable to those of Metz filtering. For the simulated image using the ^{99m}Tc PSF, NMSE results were 8.66 for multiresolution restoration and 7.54 for Metz filtering. When blurring was simulated using the ^{201}Tl , NMSE was 9.31 for multiresolution restoration and 8.74 for metz filtering. Similar results were found for the FWHM. For the blurred image the FWHM was 1.79 cm, while for multiresolution and Metz restored images the FWHM was 1.66 cm and 1.56 cm, respectively. The real value is 1.068 (Chapter 3, p. 80).

Figure 4-6 shows the count profiles through the simulated myocardium in the blurred image (Figure 4-6a), the restored image by Metz filtering (Figure 4-6b) and the restored image by using the multiresolution algorithm (Figure 4-6c). From Figure 4-6, it is evident the improvement after restoration, either with the multiresolution algorithm or Metz filtering. However, ringing artifacts were observed for both restoration methods (Figure 4-6). Finally, visual inspection of the restored images also demonstrated that both restoration methods perform equally well.

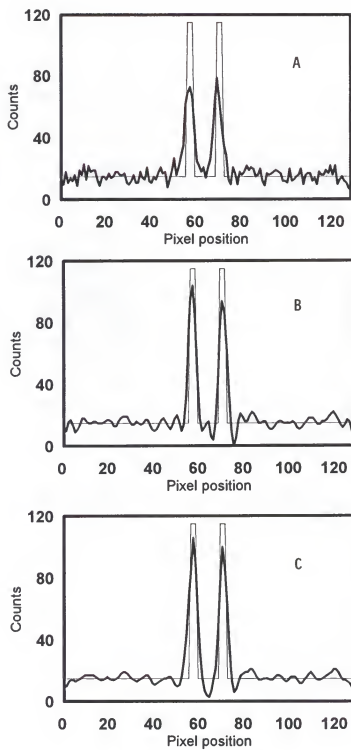


Figure 4-6. Count profiles through the simulated projection. A: Blurred image. B: Metz restoration. C: Multiresolution restoration. The fine line indicates the profile free of blurring effects.

CHAPTER 5

RESTORATION IN A REALISTIC CARDIAC CHEST PHANTOM

The multiresolution restoration algorithm was assessed in SPECT reconstructions of a realistic cardiac-chest phantom with a custom-made liver insert and different ^{99m}Tc liver-to-heart activity ratios (LHAR). Experiments were performed with and without simulated myocardial perfusion defects in apical and infero-septal regions. Multiresolution restoration was compared with conventional restoration using an optimized Metz filter. The main objective was to demonstrate the usefulness and advantages of the multiresolution algorithm for deblurring reconstructed images and minimize or even eliminate the liver spillover artifact in attenuation-corrected ^{99m}Tc myocardial SPECT.

The specific questions which were sought to be answered were: 1) For the case of a uniform attenuating medium and restored projections, what is the optimal attenuation coefficient?; 2) Does restoration need to include scatter and detector geometric response, or geometric restoration alone is sufficient to minimize or even eliminate the liver spillover artifact?; 3) For the case of inferior perfusion defects, how is the contrast and quantitation of defect size affected by the liver spillover artifact and restoration?; and finally, 4) What is the best reconstruction protocol to be used in conjunction with the multiresolution restoration method?

Material and Methods

Cardiac-Chest Phantom

Experiments were performed using a commercial cardiac-chest phantom Data Spectrum 2230 (Chapel Hill, NC) with cardiac insert 7070. The chest was simulated with a water filled cylindrical tank of diameter 24 cm and height 38 cm. The myocardium consisted of a plastic hollow cylinder 9.3 cm long with inner and outer walls of radius 2.05 cm and 3.05 cm, respectively. The apex of the heart was modeled by a hemispherical cap, also with inner and outer walls of radius 2.05 cm and 3.05 cm. The myocardial wall thickness was 1.00 cm, the total myocardial volume was 110 ml and the cardiac blood pool was 60 ml. In some experiments, two solid acrylic sectors which simulated transmural perfusion defects were inserted into the apical and infero-septal regions. Their dimensions were 1 cm thick and 2 cm and 3 cm long, respectively. The liver insert was simulated with a rectangular plastic box separated 0.5 cm from the myocardial apex. The liver was located in two different positions. The first position was parallel to the transaxial plane, such that there was no liver-myocardium superposition in any acquisition. In the second position, which only was used in experiments with myocardial defects, the liver box was tilted 30 degrees from the transaxial plane, such that in some projections there was superposition between the two organs. This last position simulated patients with high diaphragms. Myocardium activity concentration was approximately 370 kBq/ml. This concentration simulated the noise encountered in clinical studies. Chest background was 15% of the myocardium activity concentration and LHAR were 0:1, 1.5:1, 2.5:1 and 3.5:1.

SPECT Acquisition

A three-headed SPECT system (Trionix Research Laboratories, Inc., Twinsburg, OH) with a high resolution parallel hole collimator was employed. Acquisitions were carried out over 360° with a radius of rotation of 24 cm about the central axis of the chest phantom. Data were acquired into 60 projections of 128 x 64 pixels (pixel size: 0.356 cm). A primary energy window between 126 keV and 156 keV was used in all acquisitions.

Reference SPECT scans were acquired with the cardiac insert in free air with and without perfusion defects. They were considered as standard references without attenuation and tissue scattering.

SPECT Reconstruction

The standard reference was reconstructed with the same protocol used in clinical studies. This protocol uses the FBP method with the ramp filter and the Hamming window with cutoff frequency of 50% of the Nyquist. Because the cardiac phantom was in free air, attenuation and scattering corrections were not needed. However, projections were restored before reconstruction using the multiresolution method with the inverse MTF calculated in free air (multiresolution geometric restoration). In this way, restoration only included the influence of the geometric detector response. This reconstruction was compared with that with no restoration.

The SPECT scan of the cardiac phantom in water ($LHAR = 0$) was reconstructed using the same protocol, but with attenuation correction and pre-reconstruction multiresolution restoration using the inverse MTF determined in water. By using this function, restoration included the influence of both tissue scattering and geometric detector response. For

comparative purposes, a multiresolution restoration also was performed using the inverse MTF in free air. Reconstructions of the cardiac phantom in water were compared with those of the standard reference. It was expected to observe equivalent results between the reconstructed cardiac phantom in water after restoration and the standard reference. The objective of this comparison was to validate the performance of attenuation correction and multiresolution restoration methods.

Reconstructions of the cardiac-liver phantom in water were performed using the ramp filter with and without the Hamming window function. Cutoff frequencies of 25%, 50% and 100% of Nyquist were compared. Attenuation was corrected and projections were restored using multiresolution restoration including scatter and geometric corrections. The objective was to compare and select the best reconstruction protocol to be used in conjunction with attenuation correction and multiresolution restoration.

Attenuation correction was carried out with the first order Chang correction (Chapter 2, p. 35). The optimal attenuation coefficient value was determined by quantitative comparisons between reconstructions of the cardiac-liver insert in water and the standard reference using attenuation coefficient values of 0.105 cm^{-1} , 0.12 cm^{-1} , 0.135 cm^{-1} , 0.15 cm^{-1} and 0.165 cm^{-1} .

Pre-reconstruction multiresolution restoration was performed using the algorithm described in Chapter 4 (p. 99 - 108). Projections were decomposed into 5 resolution levels (Figure 5-1). In order to remove noise and apply the inverse operator only to those sub-band images with significant details the square L_2 norm of the blurred projection and representative MTF were calculated for each sub-band. Those sub-band

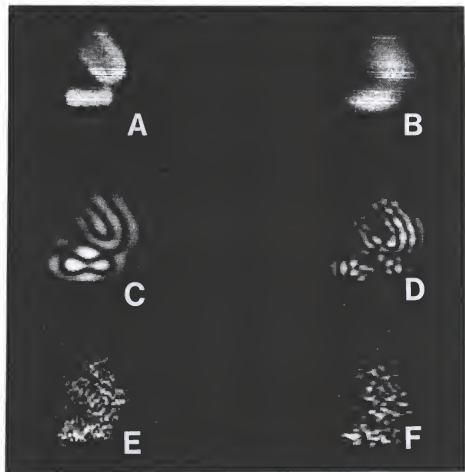


Figure 5-1. Decomposition of a projection into 5 sub-band images or resolution levels. A: Cardiac-liver projection. B: Coarse approximation (lower resolution). C and D: Intermediate resolution levels which contain significant image details. E and F: High resolution levels which only contain noise. Sub-band image pixels contain negative and positive values. This figure only depicts absolute values.

images in which the energy of the MTF and the blurred projection were less than 2% of the total MTF or projection energy, were considered as noise and discarded (Chapter 4, p. 106 - 108). According to this criterion, the last two sub-band images were discarded (Figure 5-1).

The effect of the liver spillover artifact and its compensation by multiresolution restoration was assessed in each cardiac-liver scan with and without cardiac defects by performing the following reconstructions: 1) Without any correction; 2) With restoration but without attenuation correction; 3) With attenuation correction but without restoration; and 4) With attenuation correction and restoration. Multiresolution restoration was performed both with the inverse MTF determined in free air and in water. Results of multiresolution restoration were compared with those of an optimized Metz filter. Attenuation correction and SPECT reconstructions were performed using a commercial software (Trionix Research Laboratories, Inc.). Restoration was performed with the program tomfilt.m written in MATLAB code (Appendix C.1). Utility programs trigro.c and grotri.c were written in C for conversion of image data from the SPARC 2 workstation connected to the TRIAD SPECT system to the computer in which MATLAB was installed (Appendix C.1).

Analysis Methods

Short-axis slices were reconstructed and analyzed using profile lines, and calculation of myocardial thickness, contrast and fractional standard deviation (FSD). Myocardial thickness was measured using the FWHM value of horizontal count profile lines. Contrast was calculated from regions of interest (ROI) over the myocardium (ROI(m)), defect (ROI(d)) and cardiac blood pool (ROI(bp)) in a central or near apical short-axis

slice according to

$$C = \frac{\text{Counts/pixel ROI}(m) - \text{Counts/pixel ROI}(i)}{\text{Counts/pixel ROI}(m)} \times 100 ,$$

where $i = d$ or bp for myocardial defect or cardiac blood pool, respectively. The fractional standard deviation (FSD) estimated the relative noise in reconstructions and was calculated as the ratio between the standard deviation and the average number of myocardial counts in a central or mid-ventricular short-axis slice. Myocardial counts were automatically determined as those equal to or greater than 50% of the maximum number of myocardial counts per pixel. Calculation of FSD and identification of pixels were carried out by the program fsd.c (Appendix C.2).

Bull's eye polar maps (Chapter 2, p. 25 - 28) were constructed using a software available in the TRIAD SPECT system. The normalized chi-square measure was used to determine the significance of differences between the cardiac-liver polar maps and the standard reference polar map. The normalized chi-square was calculated from

$$X^2 = \frac{1}{N} \cdot \sum_{i=1}^N \frac{(RBE(i) - OBE(i))^2}{OBE(i)} ,$$

where $RBE(i)$ is the number of counts in the i -th pixel of the restored bull's eye, $OBE(i)$ is the number of counts of the standard reference bull's eye and N is the total number of pixels included in the comparison. Those bull's eye pixels at a distance from the center larger than 85% of the polar map radius (the edge of the myocardium) were excluded from the comparison. Bull's eye polar maps were constructed as frames of 256 x 256

pixels (65536 pixels). The number of pixels included in the comparison was $N = 18621$. Calculations were carried out with the program chisqbe.c (Appendix C.2). A p value less than 0.05 was considered significant. For this significance and degrees of freedom (18620), the percentile of the normalized chi-square distribution was 0.9999 (Gibbons, 1966, Tables T-3 and T-4).

The uniformity of bull's eye polar maps was measured by calculating the mean, standard deviation (s.d.) and relative standard deviation ($r.s.d. = s.d./mean$) of bull's eye counts. Uniformity also was assessed by constructing a histogram of polar map counts. Uniformity calculations and histogram construction were carried out with the program histbe.c (Appendix C.2). Also, ratios of the mean number of counts in the anterior and inferior wall (a/i) and in the lateral and septal wall (l/s), excluding the apical region, were calculated.

Polar maps from the cardiac-liver phantom ($LHAR = 3.5$) with myocardial defects were compared to those from phantoms without defects and liver activity. Defect size was expressed in percent and estimated as the fraction of the histogram with defect which was greater than that of the without-defect histogram below a given cutoff percentage. Calculation of defect size was performed at threshold cutoff points of 45%, 50%, 55%, 60%, 65%, 70% and 75%. The true defect size as a percentage of the polar map area was calculated by weighting the dimensions of the acrylic defects by their distance from the center of the polar map. This weight takes into account the increase in the number of pixels on regions farther from the center, which have more pixels because the circumference is larger. The area of the polar map included in the histogram was calculated using the

radius given by 85% of the cardiac insert length (9.3 cm). The area of the apical defect projected onto the polar map was calculated as that of a circular surface with radius equal to 1 cm. The area of the infero-septal defect was calculated using the standard geometrical formula for the sector of an annulus (Beyer, 1984, p. 124) given by

$$A = \frac{1}{2}\theta.h.(2R + h) ,$$

where θ is the sector angle (60 degrees), h is the length of the acrylic sector (3 cm) and R is the distance from the center of the apex to the acrylic sector (2.7 ± 0.1 cm).

Results and Discussion

Validation of Attenuation Correction and Restoration Methods

Figure 5-2 shows bull's eye polar maps of the cardiac phantom (LHAR =0) without defects in free air (Figure 5-2A), in water without any correction (Figure 5-2B), in water after multiresolution restoration but without attenuation correction (Figure 5-2C) and in water after multiresolution restoration and with attenuation correction (Figure 5-2D). Multiresolution restoration included the influence of both scatter and geometric detector response.

The myocardial wall of the cardiac phantom is uniform in thickness from base to apex. Therefore, its polar map is expected to be uniform in activity distribution. The polar map of the cardiac phantom in free air approximates the ideal reconstruction without any scattering or attenuation artifact and shows the expected uniform activity distribution

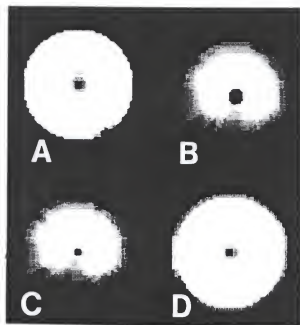


Figure 5-2. Bull's eye polar maps of the cardiac phantom without defects and LHAR = 0. A: Cardiac insert in free air. B: Cardiac insert in water without any correction. C: Cardiac insert in water after multiresolution but without attenuation correction. C: Cardiac insert in water after multiresolution restoration and with attenuation correction.

(Figure 5-2). In contrast, when the cardiac phantom is in water, the photon attenuation by the water tank produced significant nonuniformity in the polar map with decreased activity in the inferior wall (Figures 5-2B and 5-2C). Multiresolution restoration alone did not improve the image, but multiresolution restoration combined with attenuation correction restored the image and yielded the expected uniformity (Figure 5-2D).

The histogram of bull's eye counts (Figure 5-3) shows the normalized number of pixels as a function of the number of counts (maximum = 100 per pixel) in the polar map. The first class corresponds to those pixels whose number of counts is greater than 95, while the last class (class number 12) corresponds to the number of pixels whose number of counts is less than 45. The interval per class is 5 counts. Histograms have been normalized to the maximum number of pixels per class. Because the radiotracer is uniformly distributed into the myocardial wall, the standard deviation of the histogram should be zero and its mean number of counts equal to 100. However, histogram dispersion is observed due to statistical noise and algorithms used in the bull's eye polar map generation. The effect of photon attenuation is to produce significantly greater dispersion and lower mean values (Figure 5-3 and Table 5.1). These artifacts are eliminated when attenuation correction is performed, either with or without restoration.

Quantitative analysis of bull's eye polar maps (Table 5.1) showed that the ratio of the mean counts in the anterior and inferior regions improved from 1.23 without attenuation correction to 1.00 following correction. The uniformity of the polar map as measured by the r.s.d. of the counts improved from 12.7% without attenuation correction to 7.39%

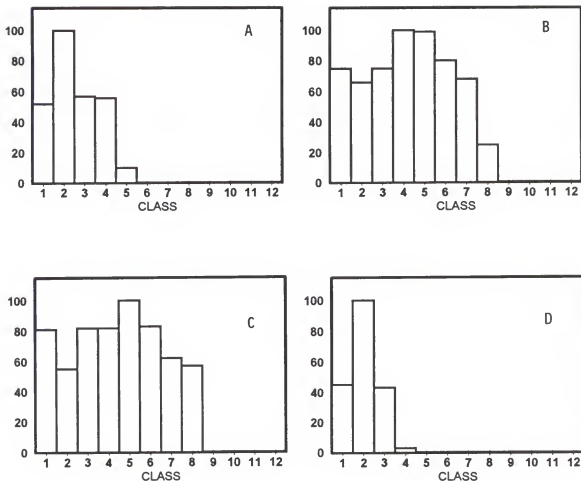


Figure 5-3. Histograms of polar map counts for the cardiac insert without liver activity. Histograms show the normalized number of pixels as a function of the number of counts (maximum = 100 per pixel) in polar maps. A: Cardiac insert in free air. B: Cardiac insert in water without any correction. C: Cardiac insert in water after multiresolution restoration but without attenuation correction. D: Cardiac insert in water with attenuation correction and multiresolution restoration.

Table 5.1

Quantitative analysis of myocardial bull's eye polar maps. Reconstructions correspond to the cardiac phantom in air and in water without liver activity.

Reconstruction	χ^2	mean	r.s.d. (%)	a/i	l/s
H in air	0.141	90.2	6.25	0.99	0.97
H in air + gMR	0.00	89.6	8.13	1.01	1.02
H in wat.	1.61*	81.8	12.7	1.29	1.01
H in wat. + gMR	2.28*	79.6	14.2	1.29	1.00
H in wat. + sgMR	1.87*	80.6	14.5	1.27	0.99
H in wat. + AC	0.141	91.9	7.39	1.00	0.99
H in wat. + AC & gMR	0.204	92.4	5.73	0.99	1.01
H in wat. + AC & sgMR	0.170	90.5	6.82	1.01	1.01

H: Cardiac phantom. wat.: Water. gMR: Multiresolution restoration including only correction for the detector geometric response. sgMR: Multiresolution restoration including corrections for both scatter and detector geometric response. AC: Attenuation correction. r.s.d.: Relative standard deviation. a/i: anterior to inferior ratio of bull's eye counts. l/s: Lateral to septal ratio of bull's eye counts. The χ^2 value was calculated taken as reference the bull's eye of the cardiac phantom in air after multiresolution restoration including only correction for the detector geometric response.

* $p < 0.05$

with correction. Without attenuation correction, normalized chi-square values demonstrated significant differences ($p < 0.05$) between the polar map of the cardiac phantom in air and in water (Table 5.1).

In addition, multiresolution restoration without attenuation correction reduces even more the number of counts in the inferior wall and makes more remarkable the photon attenuation effect (Table 5.1). This is because the repositioning of scattered photons produced by multiresolution restoration reduces the build-up effect of broad beam geometry that partially compensates attenuation (Buvat et al., 1994). In other words, without attenuation correction restoration tends to overestimate the photon attenuation effect and does not introduce any significant benefit to SPECT reconstructions. When attenuation is corrected, multiresolution restoration does not significantly improve the uniform distribution of polar map counts (Table 5.1). However, notice that these results were obtained without the interference of radioactivity from nearby organs (LHAR = 0). When high activity background is nearby the object to be imaged, restoration is necessary in order to avoid artifacts, as will be shown later in this Chapter.

Shown in Table 5.2 are the values of the FWHM of count profiles for the horizontal central line of a midventricular short-axis slice, the cardiac blood pool contrast and FSD. The midventricular slice was chosen half-way between the apical and basal slices. Results are compared among the cardiac phantom in free air, in water with and without attenuation correction and with and without multiresolution restoration. The set of FWHM values give an indication of the myocardial wall thickness. Reconstruction of the cardiac phantom in free air, with and without

Table 5.2

Quantitative analysis of a mid-ventricular short-axis slice.
 Reconstructions correspond to the cardiac phantom in air and in water
 without liver activity.

Reconstruction	FWHM (cm)	FSD (%)	Contrast	contrast/ FSD
H in air	1.85	19.85	92.6	4.66
H in air + gMR	1.70	17.41	100.0	5.74
H in wat.	1.85	17.83	82.4	4.62
H in wat. + gMR	1.63	18.62	100.0	5.37
H in wat. + sgMR	1.51	19.28	100.0	5.49
H in wat. + AC	1.85	18.93	81.9	4.33
H in wat. + AC & gMR	1.85	19.28	82.13	4.16
H in wat. + AC & sgMR	1.60	17.85	100.0	5.60

FWHM: Full width half maximum. FSD: Fractional standard deviation. H: Cardiac phantom. wat.: Water. gMR: Multiresolution restoration including only correction for the detector geometric response. sgMR: Multiresolution restoration including corrections for both scatter and detector geometric response. AC: Attenuation correction.

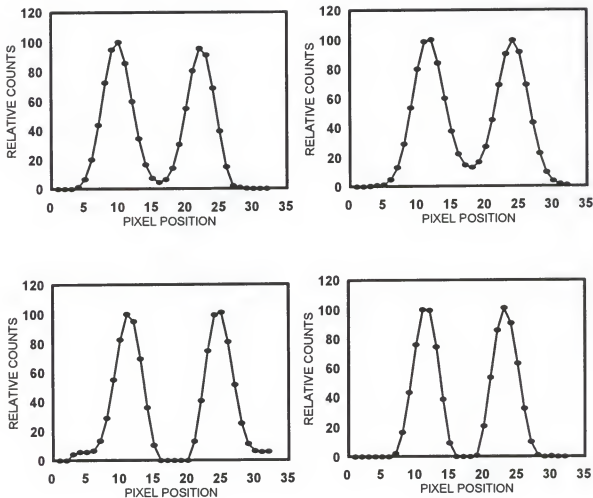


Figure 5-4. Horizontal profile lines through the center of a midventricular short-axis slice. Top left: Cardiac insert in free air, FWHM = 1.75 cm; Top right: Cardiac insert in water without any correction, FWHM = 1.89 cm; Bottom left: Cardiac insert in free air after multiresolution restoration including only geometric correction, FWHM = 1.70; Bottom right: Cardiac insert in water with attenuation correction and multiresolution restoration including scatter and geometric correction, FWHM = 1.60 cm.

multiresolution restoration including only geometric correction showed higher FWHM values (Table 5.2) and significant broadening in count profile lines (Figure 5-4). This can be explained by the lack of scattering correction. Although the cardiac phantom in free air does not have scattering due to surrounding tissue, there is a significant scatter component due to the volumetric distribution of the source into the myocardial volume (110 ml). When the phantom is within the water tank, scattering increases, count profiles become broader and FWHM values higher (Table 5.2).

In addition, attenuation correction tends to make broader count profiles. This is because attenuation correction can not distinguish between uncollided and collided photons. Therefore, scattered radiation is also multiplied by the attenuation correction factor which results in an artificial amplification of scattered counts. The importance of correcting scatter is demonstrated by the fact that multiresolution restoration of the cardiac phantom in water produced the narrowest count profiles (Figure 5-4) and lowest FWHM values (Table 5.2). When multiresolution restoration only included geometry correction, the FWHM increased 13.5% in attenuation-corrected slices. However, when multiresolution restoration also included scatter correction, the FWHM increased in just 6.0% (Table 5.2).

Results also demonstrate that multiresolution restoration including scatter and geometric correction increases contrast and contrast to FSD ratio (Table 5.2). Notice that when attenuation correction was performed in conjunction with multiresolution restoration including only geometry correction, the contrast and contrast to FSD ratio were lower than those

calculated when multiresolution restoration also included scatter compensation. This result indicates the importance of scatter compensation in SPECT quantitation. As seen in Table 5.2, FSD values were similar for all reconstructions under comparison (from 17.41% to 19.85%). This means that no significant noise increase was introduced by multiresolution restoration.

In summary, both qualitative and quantitative analysis of polar map and short-axis slices, demonstrated that the attenuation correction and multiresolution restoration used in this experiment give the closest reconstruction to that obtained with the standard reference in free air. Although multiresolution restoration did not improve uniformity in attenuation-corrected SPECT scans, contrast and blurring effects were significantly improved. This is because the construction of the polar map does not depend critically on the myocardial thickness or contrast but only on the maximum number of counts in circumferential profiles of short-axis slices (Chapter 2, p. 27 - 28).

Optimal Attenuation Coefficient

Quantitative results following the application of different attenuation coefficients are shown in Tables 5.3 and 5.4. The effect of variation in the water attenuation coefficient on the a/i ratio and r.s.d. are presented in Figure 5-5. Notice that variations in the attenuation coefficient of 57% still resulted in more uniform bull's eye polar maps than those obtained without attenuation correction.

However, the influence of the attenuation coefficient value on quantitative results depends on the level of scattered radiation in the cardiac-chest phantom. Notice that variations in the attenuation

Table 5.3

Normalized Chi-square of bull's eye polar maps as a function of the attenuation coefficient and liver-to-heart activity ratio (LHAR).

Attenuation coefficient (1/cm)	LHAR = 0 (NR)	LHAR = 0 (MR)	LHAR = 1.5 (MR)	LHAR = 3.5 (MR)
0.105	0.234	0.200	0.367	0.730
0.12	0.191	0.170	0.328	0.369
0.135	0.180	0.181	0.321	0.525
0.15	0.231	0.240	0.398	0.506
0.165	0.344	0.389	0.520	0.720

NR: No restoration. MR: Multiresolution restoration including scatter and geometric correction.

coefficient from 0.12 cm^{-1} to 0.135 cm^{-1} (14%) produced variations in the normalized chi-square of 7% for LHAR = 0, 2% for LHAR = 1.5 and 42% for LHAR = 3.5. Normalized chi-square values (Table 5.3 and Figure 5-6) demonstrate that reconstruction of SPECT scans with higher scatter background (LHAR = 3.5) are more sensitive to attenuation coefficient variations than those with lower scatter component (e.g., LHAR = 1.5).

Usually, soft tissue attenuation coefficient values employed in ^{99m}Tc SPECT reconstructions are in the range between 0.115 cm^{-1} and 0.156 cm^{-1} (Manglos et al., 1993; Wallis et al., 1995). Most common values are 0.12 cm^{-1} and 0.13 cm^{-1} (Wallis et al., 1995) for broad beams (no scatter or geometric correction). It is expected that this value includes the build-up effect of the scattered radiation. When scatter and detector geometric

Table 5.4

Uniformity of myocardial bull's eye polar maps as a function of the attenuation coefficient and liver-to-heart activity ratio (LHAR) for the cardiac-liver phantom in water.

	Attenuation coefficient (1/cm)	0.105	0.12	0.135	0.15	0.165
Mean	LHAR = 0.0	87.2	90.5	89.1	88.7	88.0
	LHAR = 1.5	88.6	90.6	90.9	92.0	93.0
	LHAR = 3.5	84.6	89.8	90.1	90.3	90.6
r.s.d.	LHAR = 0.0	6.65	6.82	5.31	6.57	7.71
	LHAR = 1.5	7.27	6.11	6.45	6.23	7.68
	LHAR = 3.5	7.41	6.22	6.04	7.53	7.82
a/i	LHAR = 0.0	1.06	1.01	0.99	0.96	0.93
	LHAR = 1.5	1.08	1.07	1.02	0.97	0.91
	LHAR = 3.5	1.08	1.06	0.98	0.94	0.87

r.s.d.: Relative standard deviation expressed in %. a/i: Anterior-to-inferior count ratio.

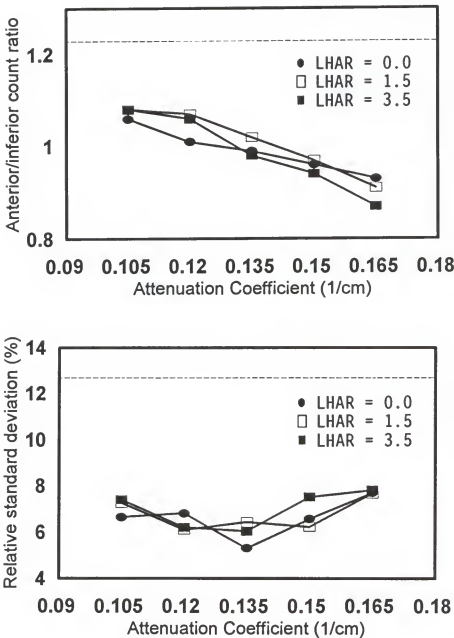


Figure 5-5. Graphs depicting the effect of variation in the attenuation coefficient value upon the uniformity of reconstructed bull's eye polar maps. Horizontal dashed lines represent the value of the anterior-to-inferior ratio (top graph) and relative standard deviation (bottom graph) for the reconstruction of the cardiac insert in water (LHAR = 0.0) without restoration and attenuation correction.

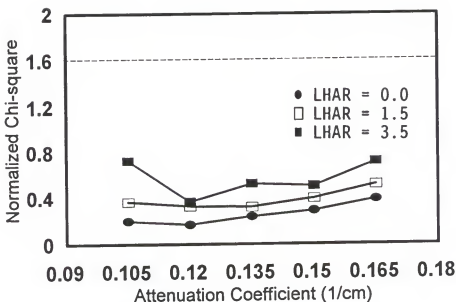


Figure 5-6. Graph depicting the effect of variation in the attenuation coefficient value upon the normalized chi-square of polar maps. The horizontal dashed line represents the normalized chi-square for the reconstruction of the cardiac insert in water (LHAR = 0.0) without restoration and attenuation correction.

response are compensated, or in phantom simulations in which scattering and geometric finite resolution are not included, the photon flux is considered as a narrow beam. Under this condition, the attenuation coefficient has been considered as 0.15 cm^{-1} (Manglos et al., 1993), 0.153 cm^{-1} (Glick et al., 1995), 0.156 cm^{-1} (Pan et al., 1996) and 0.152 cm^{-1} (Li et al., 1995). However, the narrow beam model is an approximation of reality even when high resolution collimators are employed and photon scattering and detector geometric response are compensated. This is because scattering is a complex function of the source distribution and dimensions of the object to be imaged, and current scatter and geometric

compensation methods are only approximate solutions to the problem (Buvat et al., 1994; Tsui et al., 1994a; Glick et al., 1995). Therefore, narrow beam geometry is never reached and the optimal attenuation coefficient could be different from the theoretical value of 0.15 cm^{-1} .

Wallis et al. (1995) investigated the effect of variation of the soft tissue attenuation coefficient in a cardiac chest phantom using values from 0.09 cm^{-1} to 0.17 cm^{-1} . They (Wallis et al., 1995) found that errors of 30% in the soft tissue attenuation coefficient had minimal effect on the radiotracer myocardial distribution. Finally, Wallis et al. (1995) assigned to soft tissue the attenuation coefficient value of 0.13 cm^{-1} which corresponds to that of the broad beam geometry in water. However, from the data of Wallis et al. (1995) it is evident that coefficient values between 0.12 cm^{-1} and 0.15 cm^{-1} could be appropriate for attenuation correction. The study of Wallis et al. (1995) was performed using 180 degrees of projection data (higher attenuation), no scatter or geometric compensation and without high activity background around the cardiac phantom.

The results of this research agree with those of Wallis et al. (1995) but only for relatively low liver background ($LHAR = 1.5$). When liver activity was very high (e.g., $LHAR = 3.5$) the bull's eye polar map uniformity was more dependent on the attenuation coefficient value (Table 5.4 and Figures 5-5 and 5-6). According to these results, the optimal attenuation coefficient value used in this research was 0.12 cm^{-1} . When the attenuation coefficient was lower than 0.12 cm^{-1} , the compensation was insufficient and the mean number of counts of the histogram slightly decreased while the r.s.d. increased (Table 5.4 and Figure 5-5).

Attenuation coefficient values higher than 0.15 cm^{-1} overcompensated attenuation and anterior wall counts were lower than those in the inferior wall (Figure 5-5). This effect was more pronounced when the liver activity was high. In this case ($\text{LHAR} = 3.5$), attenuation coefficients of 0.135 cm^{-1} and 0.15 cm^{-1} slightly distorted the bull's eye uniformity (Tables 5.3 and 5.4 and Figure 5-6).

Optimal Reconstruction Protocol

Table 5.5 and Figure 5-7 show the normalized chi-square values of bull's eye polar maps obtained with attenuation correction and four different reconstruction protocols. When reconstructions were performed without smoothing window, it was observed a significant nonuniform polar map for $\text{LHAR} = 3.5$ (Tables 5.5 and 5.6 and Figures 5-7 and 5-8). Reconstructions performed without restoration and smoothing window, demonstrated acceptable uniformity only when the cutoff frequency was 25% of Nyquist and LHAR less than 1.5 (Tables 5.5 and 5.6 and Figure 5-7a). This cutoff frequency provoked the liver spillover artifact when the liver activity was higher (e.g., $\text{LHAR} = 3.5$). Higher cutoff frequencies eliminated the liver spillover artifact, even for the highest LHAR, but the increase on noise significantly affected the uniformity of bull's eye polar maps (Figures 5-7a and 5-8). Reconstruction of polar maps with multiresolution restoration but without smoothing window did not demonstrate acceptable uniformity (Tables 5.5 and 5.6 and Figure 5-7b). Reconstructions with Hamming window but without restoration improved significantly the uniformity for LHAR less than 1.5 and cutoff frequency of 50% of Nyquist. For higher liver activity (e.g., $\text{LHAR} = 3.5$) the blurring of images significantly distorted the bull's eye uniformity.

Table 5.5

Normalized chi-square calculated with different reconstruction protocols as a function of the liver-to-heart activity ratio (LHAR). All reconstructions were corrected for attenuation.

Reconstruction	LHAR = 0	LHAR = 1.5	LHAR = 3.5
NR, ramp (f = 25% Nq)	0.225	0.195	2.01
NR, ramp (f = 50% Nq)	0.688	0.852	2.31
NR, ramp (f = 100% Nq)	0.708	0.840	1.09
sgMR, ramp (f = 25% Nq)	1.94	1.32	0.71
sgMR, ramp (f = 50% Nq)	2.08	1.25	2.29
sgMR, ramp (f = 100% Nq)	2.70	1.32	2.28
NR, Hamm (f = 25% Nq)	0.828	0.862	2.17
NR, Hamm (f = 50% Nq)	0.191	0.369	1.35
NR, Hamm (f = 100% Nq)	0.571	0.348	1.11
sgMR, Hamm (f = 25% Nq)	1.99	1.14	2.10
sgMR, Hamm (f = 50% Nq)	0.170	0.32	0.369
sgMR, Hamm (f = 100% Nq)	1.57	1.69	2.73

NR: No restoration. f: Cutoff frequency. Nq: Nyquist frequency. sgMR: Multiresolution restoration including corrections for scatter and detector geometric response. Hamm: Hamming window.

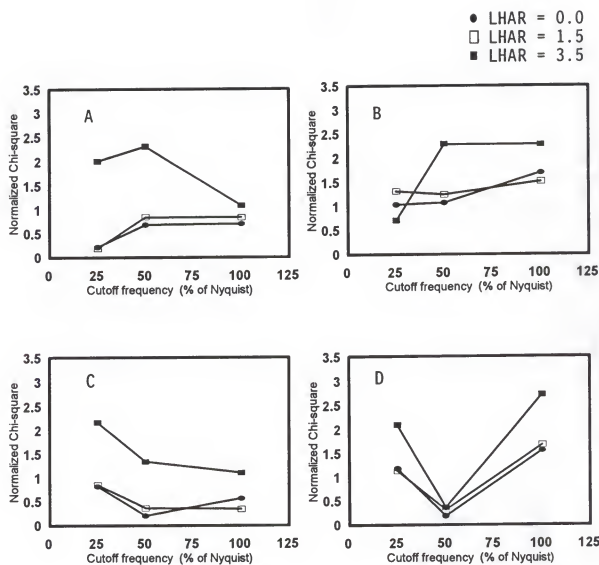


Figure 5-7. Normalized chi-square of bull's eye polar maps as a function of the liver-to-heart activity ratio (LHAR) and cutoff frequency for four different reconstruction protocols. A: No restoration and no window function. B: Multiresolution restoration including scatter and geometric correction with no window function. C: Hamming window function without multiresolution restoration. D: Multiresolution restoration including scatter and geometric correction with Hamming window function.

Table 5.6

Uniformity of bull's eye polar maps calculated using different reconstruction protocols. All reconstructions were corrected for attenuation. Data are expressed as mean number of counts (relative standard deviation).

Reconstruction	LHAR = 0	LHAR = 1.5	LHAR = 3.5
NR, ramp (f = 25% Nq)	90.7 (7.62%)	90.5 (8.01%)	77.5 (6.79%)
NR, ramp (f = 50% Nq)	86.4 (7.86%)	85.7 (9.50%)	62.9 (11.8%)
NR, ramp (f = 100% Nq)	85.9 (8.16%)	88.5 (8.22%)	85.3 (9.12%)
sgMR, ramp (f = 25% Nq)	86.3 (8.31%)	85.4 (10.9%)	85.7 (8.42%)
sgMR, ramp (f = 50% Nq)	79.7 (12.0%)	78.1 (13.1)	80.4 (12.8%)
sgMR, ramp (f = 100% Nq)	77.9 (13.4%)	80.4 (12.2%)	81.3 (12.6%)
NR, Hamm (f = 25% Nq)	80.0 (8.26%)	79.7 (9.92%)	75.6 (7.81%)
NR, Hamm (f = 50% Nq)	90.4 (5.03%)	91.6 (6.07%)	79.4 (5.10%)
NR, Hamm (f = 100% Nq)	86.2 (6.71%)	87.7 (6.85%)	82.2 (6.90%)
sgMR, Hamm (f = 0.25 Nq)	79.2 (9.6 %)	78.6 (9.9 %)	76.1 (7.7 %)
sgMR, Hamm (f = 0.5 Nq)	91.9 (7.4 %)	90.6 (6.1 %)	90.1 (6.18%)
sgMR, Hamm (f = 1.0 Nq)	81.2 (9.9 %)	76.3 (7.69%)	67.4 (11.3 %)

NR: No restoration. f: Cutoff frequency. Nq: Nyquist frequency. sgMR: Multiresolution restoration including corrections for scatter and detector geometric response. Hamm: Hamming window.

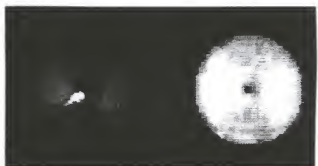


Figure 5-8. Bull's eye polar maps of the cardiac-liver insert ($LHAR = 3.5$) in water. Reconstructions were performed with attenuation correction but without restoration and window function. Left: Cutoff frequency of 25% of Nyquist; Right: Cutoff frequency of 100% of Nyquist.

(Figure 5-7c). Finally, multiresolution restoration in conjunction with Hamming window (cutoff frequency of 50% of Nyquist), significantly improved bull's eye uniformity for all $LHAR$ (Figure 5-7d). These results demonstrated that in order to eliminate the liver spillover artifact for any $LHAR$, a smoothing window function should be used in conjunction with multiresolution restoration.

Usually, the selection of SPECT window functions have been based on criteria of visually acceptable resolution and minimal noise in reconstructed images (Larsen, 1980; Germano et al., 1995). Filters commonly used in SPECT have demonstrated good performance in terms of lesion detectability when the dynamic range in image data is not very high. However, they seem to be the worst choice in cardiac SPECT with ^{99m}Tc -labeled compounds due to the high liver activity (Germano et al., 1995; Nuyts et al., 1995; Zeng et al., 1995). In order to eliminate liver

artifacts in cardiac SPECT, Germano et al. at. (1995) proposed that reconstructions would be performed by using ramp filter but without pre-filtering or smoothing of projection data. Results of Tables 5.5 and 5.6 and Figures 5-7 and 5-8 demonstrated, at least for the experimental conditions of this research, that the best solution is pre-reconstruction restoration and reconstruction with a smoothing window function.

It is known (Larssen, 1980) that the ramp filter maximizes spatial detail at the cost of maximizing noise effects and rim artifacts as well. The higher resolution achieved with the ramp filter could eliminate the liver spillover artifact, but at expenses of unacceptable noise increases (Figure 5-8). The high frequency filtering or denoising of projections performed by the multiresolution algorithm is not sufficient for compensating the artifacts introduced by ramp filtering (Chapter 2, p. 24 - 26). Rim artifacts around hot structures also have been observed in liver studies after Wiener restoration and FBP reconstructions with ramp filter (Glick et al., 1994). This artifact, that can be seen in low-pass Butterworth windows, although to a lesser degree (Glick et al., 1994), is due to the fast decrease of the filter amplitude from its peak value down toward zero as the frequency increases. The multiresolution analyzing functions used in this research are equivalent to band-pass filters in which there is not a smooth roll-off of the amplitude toward zero (Figure 4-2). Therefore, rim artifacts could be produced, such as those reported by Wang et al. (1995) in planar multiresolution restoration of Lena images. Rim artifacts introduced by multiresolution restoration (Figure 4-6) are amplified by the ramp filter producing noisy and distorted reconstructions (Figure 5-7b). A proper smoothing window function must

compensate this effect by slowing down the roll-off of analyzing functions amplitude toward zero during reconstruction.

Tables 5.5 and 5.6, and Figures 5-7 and 5-8 also demonstrated that the cutoff frequency dramatically affect reconstructed images. The frequency cutoff determines not only which spatial frequencies are retained in the reconstruction, but also their relative weight during the backprojection operation. Low cutoff frequencies (e.g., 25% of Nyquist) produced blurring of images and consequently the superposition of liver activity into the inferior myocardial wall when the LHAR was very high (Figure 5-8). In contrast, high cutoff frequencies (e.g., 100% of Nyquist), increased resolution and compensated the liver spillover artifact, but also increased noise (Figure 5-8). This is reflected in the significant nonuniformity of bull's eye polar maps (Tables 5.5 and 5.6 and Figure 5-8).

Comparison with Metz Restoration

In order to compare the multiresolution algorithm with conventional restoration, a Metz filter was implemented and optimized by trial-and-error. Table 5.7 shows the FWHM, FSD and contrast measurements computed in a midventricular short-axis slice of the cardiac insert in water (LHAR = 0) after Metz restoration with different power factors. The Metz filter included the MTF determined in water. Therefore, the influence of both scatter and detector geometric response were compensated by Metz filtering. At X = 11 contrast reached the ideal value of 100%, FWHM was closest to the actual value of 1.0 cm and the FSD was acceptable (Table 5.2). At X = 14 the amplification of high frequency components increased noise without advantages in contrast or FWHM (Table 5.7). In this case,

Table 5.7

Quantitative analysis of a midventricular short-axis slice of the cardiac insert in water without liver activity. Pre-reconstruction Metz filtering was performed with different power factors.

Power Factor	FWHM (cm)	FSD (%)	Contrast	Contrast/FSD
4	1.89	18.9	94	4.97
8	1.61	18.3	96	5.25
11	1.53	18.1	100	5.52
14	1.67	19.6	100	5.10

the amplification of frequency components was more pronounced in those ranges corresponding to noise than in those corresponding to real image details. Table 5.8 demonstrated good uniformity of bull's eye polar maps for power factors in the range between 11 and 14. However, because $X = 11$ produced less noisy images with better resolution (Table 5.7) this value was adopted for Metz filtering in this research.

Table 5.9 and Figure 5-9 show the normalized chi-square values for attenuation-corrected polar maps as a function of LHAR. It is evident that for LHAR greater than 1.5, the spillover of liver activity into the inferior myocardial wall significantly distorted polar maps (Figures 5-9 and 5-10). This artifact was significantly reduced by using either the Metz or multiresolution restoration (Table 5.9 and Figures 5-9 and 5-10). Notice that multiresolution restoration with the MTF in free air (only compensates geometric detector response) was not sufficient to provide acceptable uniformity (Table 5.9 and Figure 5-9). These data demonstrated

Table 5.8

Quantitative analysis of bull's eye polar maps of the cardiac-liver insert in water. Pre-reconstruction Metz filtering was performed with different power factors.

Power factor	LHAR	Normalized Chi-square	Mean	r.s.d. (%)
4	0.0	0.25	91.9	6.79
	1.5	0.15	92.7	7.33
	3.5	2.97	56.3	11.2
8	0.0	0.23	90.8	5.42
	1.5	0.19	92.3	6.30
	3.5	2.20	58.4	10.3
11	0.0	0.16	90.4	6.45
	1.5	0.31	89.5	6.37
	3.5	0.361	88.9	7.11
14	0.0	0.28	90.5	5.29
	1.5	0.31	90.6	9.14
	3.5	0.40	88.3	7.12

LHAR: Liver-to-heart activity ratio. r.s.d.: Relative standard deviation.

Table 5.9

Quantitative analysis of the effect of multiresolution restoration on the normalized chi-square of bull's eye polar maps for different liver-to heart activity ratio (LHAR) and reconstruction protocols.

Reconstruction protocol	LHAR = 0.0	LHAR = 1.5	LHAR = 2.5	LHAR = 3.5
AC only	0.191	0.369	1.43*	1.35*
AC + gMR	0.204	0.300	0.496	0.715
AC + sgMR	0.170	0.320	0.328	0.369
AC + MetzR	0.160	0.310	0.344	0.361

AC: Attenuation correction. gMR: Multiresolution restoration including only correction for the detector geometric response. sgMR: Multiresolution restoration including corrections for both scatter and geometric detector response. MetzR: Metz restoration (includes scatter and geometric detector response corrections).

* p < 0.05

that scatter has to be compensated in order to significantly reduce or even eliminate the liver spillover artifact.

Table 5.10 shows the uniformity values of polar maps. It is known that reconstructions without attenuation correction yielded significantly low mean count values (Table 5.1). However, attenuation-corrected polar maps without or with insufficient restoration shifted down mean counts for LHAR greater than 1.5 (Figure 5-9). This is due to the liver spillover activity that produced the highest number of counts (> 90) in a relatively small number of pixels localized in the inferior wall (Figure 5-10). Restoration methods including both scatter and geometric correction, compensated this artifact yielding a more uniform polar map similar to that of the standard reference (Figure 5-10).

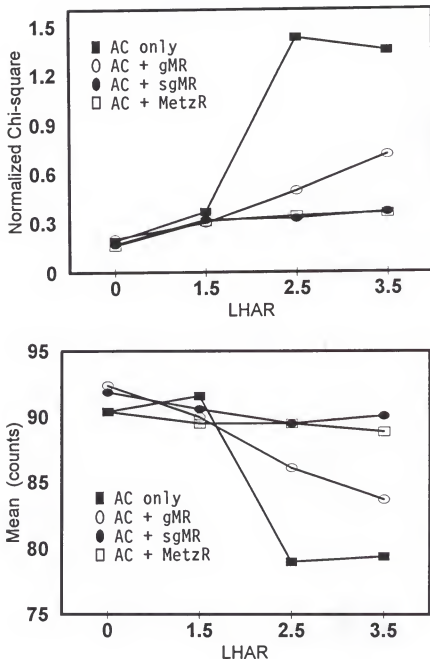


Figure 5-9. Graphs depicting the effect of restoration on uniformity of bull's eye polar maps as a function of the liver-to-heart activity ratio (LAR). AC: Attenuation correction; gMR: Multiresolution restoration including only geometric correction; sgMR: Multiresolution restoration including scatter and geometric correction; MetzR: Metz restoration including scatter and geometric correction.



Figure 5-10. Effect of restoration on bull's eye polar maps. Liver-to-heart activity ratio was 3.5. Left: Attenuation correction without restoration; Right: Attenuation correction and multiresolution restoration including scatter and geometric correction.

In this experiment there was no visual or quantitative difference between the performance of Metz filtering and multiresolution restoration. Although restoration methods could be based on different approaches, usually they produce similar results. Equivalent restored clinical SPECT images have been reported with Metz and Wiener filtering (King et al., 1984). Also, comparison between results with multiresolution-based restoration and conventional methods have not demonstrated significant differences (Wang et al., 1995; Qian and Clarke, 1996). Multiresolution representations by using wavelet decomposition have been recently applied to empirically segmentate noise from image details as a preprocessing algorithm for restoration (Wang et al., 1995; Qian and Clarke, 1996). Wang et al. (1995) used this strategy to expand by orthogonal wavelets both the linear degrading operator and the degraded image. The objective was to eliminate noise components and estimate the wavelet coefficients of the undegraded image by using a regularization approach. The restoration

Table 5.10

Quantitative analysis of the effect of multiresolution restoration on uniformity of bull's eye polar maps as a function of the liver-to-heart activity ratio (LHAR) for different reconstruction protocols. Data are expressed as mean number of counts (relative standard deviation).

Reconstruction Protocol	LHAR = 0.0	LHAR = 1.5	LHAR = 2.5	LHAR = 3.5
AC only	90.4 (5.03%)	91.6 (6.07%)	79.0 (5.94%)	79.4 (5.10%)
AC + gMR	92.4 (5.73%)	90.0 (6.29%)	86.1 (7.01%)	83.7 (7.62%)
AC + sgMR	91.9 (7.40%)	90.6 (6.10%)	89.5 (6.32%)	90.1 (6.18%)
AC + MetzR	90.4 (6.45%)	89.5 (6.37%)	89.5 (5.47%)	88.9 (7.11%)

AC: Attenuation correction. gMR: Multiresolution restoration including only geometric correction. sgMR: Multiresolution restoration including scatter and geometric correction. MetzR: Metz restoration including scatter and geometric correction.

method of Wang et al. (1995), which is similar to that used in this investigation, provided comparable results with those of the Wiener filter when both were applied to the Lena image degraded by a two-dimensional Gaussian function and additive Gaussian noise. Similarly, Qian and Clarke (1996), have proposed a wavelet-based neural network to remove noise while restoring images. Image deconvolution by a modified Hopfield neural network was carried out only in those sub-band images containing significant image details. The method was applied for imaging beta emitters (^{32}P and ^{90}Y) by bremsstrahlung detection using a gamma camera. They also found similar results with image restoration by using a previously reported order statistical neural network hybrid restoration filter. However, wavelet-based restoration demonstrated better performance for images with high noise levels (Qian and Clarke, 1996).

In this research, the main advantage of the multiresolution restoration over Metz filtering is that no optimization process is required. Multiresolution restoration states a more concise and straightforward approach to the restoration problem in which its automatic implementation is simple and does not require operator intervention.

Calculation of Defect Size

Infero-septal defect contrast measured in a short-axis is shown in Table 5.11 for different reconstruction protocols. The short-axis slice was chosen by selecting the slice where the left ventricular cavity was visible and the defect reached the maximum size by visual inspection. This was the eighth slice counted from the apex toward the base. Its distance from the apex was 2.8 cm. At this level, the liver activity still was

Table 5.11

Contrast of myocardial defect measured in a short-axis slice for different reconstruction protocols.

H in air	H in water LHAR = 3.5 NAC	H in water LHAR = 3.5 AC	H in air gMR	H in water LHAR = 3.5 AC + gMR	H in water LHAR = 3.5 AC + sgMR
62.8%	58.9%	53.5%	78.6%	64.8%	79.8%

H: Cardiac insert with myocardial defect. LHAR: Liver-to-heart activity ratio. NAC: No attenuation correction. AC: Attenuation correction. gMR: Multiresolution restoration including geometric correction. sgMR: Multiresolution restoration including scatter and geometric correction.

evident (Figure 5-11). Table 5.11 demonstrates the significant improvement in contrast due to restoration, as evident in Figure 5-11. The compensation of liver scattered photons improved contrast from 53.5% without restoration to 79.8% with multiresolution restoration. These findings are consistent with those of the cardiac blood pool contrast calculations with the cardiac insert free of myocardial defects.

Table 5.12 shows the results of the geometric calculation of true defect size from their projections on the polar map. The true defect size was calculated with a minimum error of 2.4%. Table 5.13 and Figure 5-12 show the defect size measured at various threshold cutoff levels ranging from 45% to 75% of the maximum number of counts per pixel.

The cardiac phantom in air, either with or without multiresolution geometric restoration demonstrated that a threshold value of 65% allows to estimate the defect size with relative errors below 2% (Table 5.13). At



A



B

Figure 5-11. Myocardial tomographic slices for the cardiac insert in water with apical and inferoseptal defects. A: With attenuation correction but without restoration. B: With attenuation correction and multiresolution restoration. The liver-to-heart activity ratio was 3.5. Upper left: Short-axis slice. Upper right: Vertical long-axis slice. Lower left: Horizontal long axis slice.

Table 5.12

Results of geometric calculation of true defect size on the bull's size polar map.

Polar map area (cm ²)	Apical defect area (cm ²)	Infero-septal defect area (cm ²)	Total defect area (cm ²)	Defect area in % of polar map area
196.3	3.14	13.19	16.33	8.32

Table 5.13

Defect size in percent of the polar map area calculated from the histogram of counts of bull's eye polar maps as a function of the threshold level. The liver-to-heart activity ratio was 3.5 when the cardiac insert was in air. There was no liver activity when the cardiac insert was in air (standard reference).

Threshold (%)	H in air	H in wat. (NC)	H in wat. (AC)	H in air (gMR)	H in wat. (AC + gMR)	H in wat. (AC + sgMR)
45	1.99	1.14	0.16	3.40	1.79	2.99
50	3.08	1.90	0.82	4.69	2.71	3.87
65	4.95	3.48	1.14	5.69	3.68	6.80
60	6.63	6.13	2.45	7.13	4.35	6.80
65	8.45	11.61	3.12	8.44	5.63	8.15
70	8.70	25.32	3.80	8.72	5.63	8.22
45	7.72	42.44	5.01	9.24	6.61	8.74

H: Cardiac insert. wat: Water. NC: No correction. AC: Attenuation correction. gMR: Multiresolution restoration including only geometric correction. sgMR: Multiresolution restoration including scatter and geometric correction.

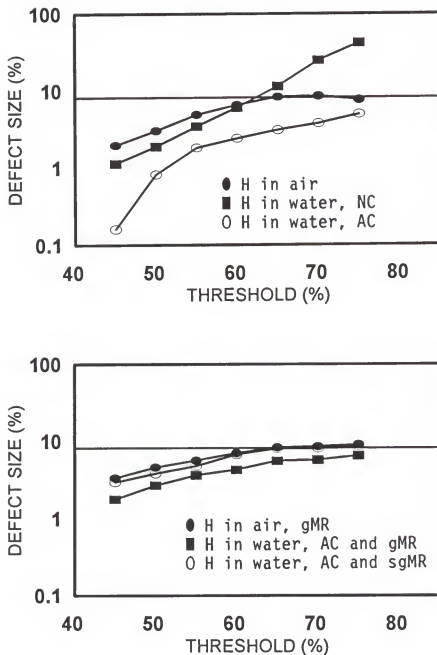


Figure 5-12. Graphs depicting the calculated defect size as a function of threshold level. The horizontal line represents the true defect size. Top graph: Reconstructions without restoration. Bottom graph: Reconstructions with restoration. H: Cardiac insert; NC: No correction; AC: Attenuation correction; gMR: Multiresolution restoration including geometric correction; sgMR: Multiresolution restoration including scatter and geometric correction.

this threshold level, the cardiac insert in water and with liver activity demonstrated a significantly higher defect size value (Table 5.13 and Figure 5-12). When attenuation was compensated the calculated defect size was lower due to the spillover effect on infero-septal and apical regions (Figure 5-12). Higher threshold levels did not improve the estimation for the attenuation-compensated SPECT reconstruction. When attenuation was uncorrected the spillover effect on the defect size was less evident but still affected the estimation. Higher threshold levels ($> 60\%$) included pixels of the inferior wall with low counts due to attenuation. Thus, the estimated defect size was artificially increased (Figure 5-12).

Multiresolution restoration compensated these artifacts and yielded a proper estimate of defect size at threshold levels between 65% and 75% (Table 5.13 and Figure 5-12). Notice that the defect size determination is relatively insensitive to variations in threshold values between 65% and 75% when attenuation is compensated and multiresolution restoration includes scatter and geometric correction (Figure 5-12). However, multiresolution restoration including only geometric correction was insufficient to compensate the liver activity and the estimated defect size was significantly lower (Figure 5-12). Multiresolution restoration including both scatter and geometric detector response compensations yielded relative errors of 2.04% and 1.20% in calculating defect size for threshold values of 65% and 70%, respectively. These errors are similar to that estimated in the geometric calculation of the true defect size. The geometric calculation of defect size only included the error in measuring the distance from apex to the infero-septal defect in the cardiac insert. Other errors, such as those due to statistical fluctuations of pixels with

low counts or involved in the polar map construction algorithm were not included because they were unknown. Therefore, it could be expected that the relative error of the true defect size is larger than 2.4%. These data demonstrate the high accuracy in determining defect size from the histogram of counts when projections are attenuation-corrected and restored using the multiresolution algorithm.

The optimal threshold value determined in this research with the cardiac insert in free air or in water after restoration, is similar to those reported by others (Table 5.14). Gibbons et al. (1989) found in cardiac phantom studies with ^{99m}Tc that a threshold value of 60% yielded the best agreement between the true defect size as a percentage of left ventricular volume and the measured defect size. The study of Gibbons et al. (1989) was performed without attenuation correction or scatter compensation. The same threshold value of 60% was used in a multicenter trial (O'Connor et al., 1995b) for determining defect sizes in cardiac phantoms with ^{99m}Tc . The study included twenty-two SPECT systems in 19 laboratories. Reconstructions were performed without attenuation and scatter compensation. The mean error in estimating defect size was below 5% (O'Connor et al., 1995b).

However, studies on the effect of attenuation and scattering artifacts on quantitation of defect size are scarce. Only the study of O'Connor et al. (1995a) addressed the scatter influence on defect size measurements. Nevertheless, this study (O'Connor et al., 1995a) did not include the effect of scattered activity from myocardial surrounding organs, such as liver or stomach. The cardiac-chest phantom used by O'Connor et al. (1995a) and others (Gibbons et al., 1989; O'Connor et al.,

Table 5.14

Threshold values for calculating defect size in cardiac SPECT.

Reference	Radionuclide	Corrections	Abdominal background	Optimal threshold
Gibbons et al., 1989	^{99m}Tc	No	No	60%
O'Connor et al., 1990	^{201}Tl	No	No	70%
O'Connor et al., 1995a	^{99m}Tc	Scatter compensation	No	55%
O'Connor et al., 1995b	^{99m}Tc and ^{201}Tl	No	No	60%
Manglos et al., 1993	^{99m}Tc	Attenuation correction	No	70% - 80%
This investigation	^{99m}Tc	Geometric restoration	No, cardiac insert in free air	65%
This investigation	^{99m}Tc	Attenuation correction, scatter and geometric restoration	Yes, LHAR = 3.5	70%

LHAR: Liver-to-heart activity ratio.

1995b) only included myocardium, lungs and background. O'Connor et al.(1995a) compared defect size calculations for both ^{99m}Tc and ^{201}Tl SPECT reconstructions with and without scatter correction using a multiple energy window method. It was found that for both ^{201}Tl and ^{99m}Tc , threshold values between 55% and 60% gave the lowest absolute error in estimating defect size. Scatter correction did not significantly modify the optimum threshold value but reduced the average absolute error from 2.1% to 0.8% for ^{99m}Tc and 1.4% for ^{201}Tl (O'Connor et al., 1995a). Following scatter correction, the optimum threshold for ^{99m}Tc was reduced from 60% to 55% (O'Connor et al., 1995a). Similarly, the optimal threshold for ^{201}Tl (higher scatter content) was 60%. This is a lower value compared with a previous threshold of 70% reported by the same group (O'Connor et al.,1990) for ^{201}Tl studies without scatter correction and using a lower resolution SPECT system.

The effect of attenuation on defect size measurements has been studied by Manglos et al. (1993) in a cardiac phantom with a realistic attenuating geometry. The physical phantom included lungs, bone (spine) and soft tissue. Lungs and spine were simulated with commercial materials while soft tissue with water. Defect size was calculated using bull's eye polar maps. Results demonstrated that attenuation compensation did not significantly affect the size of myocardial defects as long as the defect size was determined by comparison to a standard reference with similar attenuation properties. Defects in attenuation-compensated maps were generally lower than those in maps without compensation, but the effect was no significant. Also, optimal threshold levels for attenuation-compensated maps were larger than those for uncompensated maps (5%) and

dependent on the size and location of the defect. Finally, Manglos et al. (1993) concluded not only that attenuation compensation has little effect on defect size estimations, but that the attenuation itself has little effect. The study of Manglos et al. (1993) did not include background from other organs. Therefore, their conclusions can not be compared with those of this research. To our knowledge, an exhaustive analysis of the effect of scattered photons from other organs on quantitation of myocardial defect sizes has not been published. This research demonstrated the significant effect of scattered radiation on defect size calculations. Also, it was demonstrated how scatter and geometric restoration compensates this undesirable effect and gives an accurate estimation of defect size.

Conclusions

The realistic cardiac-chest model with a custom-made liver insert used in this experiment was able to reproduce the liver spillover artifact in attenuation-corrected cardiac SPECT scans. Reconstructions without attenuation correction demonstrated that photon attenuation is the main degrading effect in cardiac SPECT.

Prereconstruction multiresolution restoration with a stationary inverse MTF which includes the effects of scatter geometric detector response significantly reduced or even eliminated the liver spillover artifact. Experiments demonstrated that the multiresolution restoration algorithm is a computationally efficient method of compensating scatter and geometric detector response, at least with the accuracy required in clinical cardiac SPECT. Also contrast and quantitation of defect size were significantly improved by multiresolution restoration. Restoration of

geometric detector response alone was insufficient for compensating the liver spillover artifact. The determinant role of photon scattering in generating the overcounting artifact lead to include scatter compensation in the restoration algorithm.

Rim artifacts due to the fast decrease of the amplitude of multiresolution analyzing functions from their peak value to zero, were amplified by ramp filtering. This undesirable effect was eliminated by using a smoothing window function. The Hamming window (frequency cutoff = 50% of Nyquist) used in clinical studies demonstrated to be a proper option.

The optimal attenuation coefficient in this experiment was approximated by 0.12 cm^{-1} instead of the theoretical 0.15 cm^{-1} for narrow beam geometries. It is supposed that using a smaller value of the attenuation coefficient, such as 0.12 or 0.13 cm^{-1} , some compensation for scatter is achieved by undercorrecting attenuation. When some scatter and geometric detector correction has been applied, it is expected to use the narrow beam geometry coefficient of 0.15 cm^{-1} . In this experiment the larger 0.15 cm^{-1} value was no adequate to compensate the spillover artifact when LHAR was very high ($\text{LHAR} > 2.5$), even when restoration was applied. The explanation is that restoration does not completely compensate scattered photons. The assumptions included in the restoration model, such as scattering is independent on source distribution and position, introduce quantitative inaccuracies which made invalid the narrow beam geometry approximation.

Quantitative and qualitative results of multiresolution restoration were equivalent to those of conventional Metz restoration. This is an

additional demonstration of the good performance of the multiresolution algorithm. The advantage of the multiresolution method is that no optimization process was required. The algorithm was generated in an automatic way, taken only the information of the MTF, without intervention of the operator. This is a significant advantage over conventional restoration, such as Metz or Wiener, in which the selection of the optimal filter is image dependent and requires trial-and-error selections (Metz) or estimation of unknown power spectra (Wiener). Therefore, the multiresolution method could be easily incorporated in an automatic reconstruction algorithm.

CHAPTER 6 CONCLUSIONS AND FUTURE WORK

A wavelet-based multiresolution restoration algorithm has been developed for compensating scatter and detector geometric response in cardiac SPECT. The degrading effects of scatter and geometric detector response have been corrected by the technique of deconvolving the point spread function of the imaging system from each SPECT projection prior to tomographic reconstruction. In order to include the degradation effects due to both scatter and finite detector resolution, the point spread function was determined with radioactive sources immersed in a scattering medium. The multiresolution algorithm was used for denoising SPECT projections and regularization of the deconvolution operator. This is a new alternative to the restoration problem in SPECT in which projections are decomposed into frequency/resolution sub-band images. Then, high frequency noise is segmented from significant image features while deconvolution is performed only in dominant frequency/resolution sub-band images.

The multiresolution restoration method was able to correct the degrading effects of both scatter and detector geometric response in experiments performed with ^{99m}Tc in a realistic cardiac-chest phantom. This was demonstrated by calculating contrast and myocardial thickness in short-axis slices, defect size in bull's eye polar maps and by compensating the liver spillover artifact in attenuation-corrected SPECT

scans.

This research demonstrated the significant effect of scattered radiation on quantitation of myocardial inferior defect sizes in attenuation-corrected cardiac SPECT. It also demonstrated that multiresolution restoration is sufficient to yield an accurate estimation of defect size.

The main goal of this research was to develop a method, which could be implemented in the clinical setting, for compensating the liver spillover artifact in attenuation-corrected cardiac SPECT. Experimental results demonstrated that pre-reconstruction multiresolution restoration in conjunction with reconstruction using the FBP method and a smoothing window function compensated the artifact, at least with the accuracy required in clinical studies. The possibility of combining multiresolution restoration with the FBP technique allows the practical implementation of the method in clinical studies. In addition, multiresolution restoration approaches have usually been based on orthogonal wavelet series defined by Daubechies and image decomposition by wavelet inner products (Wang et al., 1995; Qian and Clarke, 1996). This research exploited the scalar frequency domain representation of the shift-invariant restoration problem in SPECT and used sub-band frequency filter functions and restoration in the frequency domain rather than wavelet inner products. This approach is easier and faster to implement in any SPECT computer platform by using discrete Fourier transform techniques.

Experiments with the realistic cardiac-chest phantom did not demonstrate qualitative or quantitative differences between the performance of multiresolution restoration and conventional Metz

filtering. However, the main advantage of the multiresolution method is that optimization processes by the intervention of an experienced operator are not required. It is known that this is a major disadvantage of Metz type filters, in which parameter optimization has to be accomplished by a trial and error method. The Wiener filter, which is the other classical restoration filter in nuclear medicine, requires the estimation of the power spectra of the object image and noise, which are unknown. In contrast, the multiresolution method provides a concise and straightforward approach to the restoration problem which is performed automatically without operator intervention. This is an additional advantage for its incorporation into clinical reconstruction protocols.

Other Potential Applications

The multiresolution restoration method is a general scatter and geometric detector response compensation procedure which is not limited to cardiac SPECT. It can be applied to other problems in SPECT and PET in which shift-invariant restoration have demonstrated good performance. For example, a current problem in nuclear medicine is the resolution recovery in imaging intratumoral uptake of radiolabeled monoclonal antibodies for tumor therapy. Conventional restoration filters have been investigated in this field to obtain high resolution images in ^{131}I pinhole SPECT of brain tumors (Smith et al., 1997) and for imaging the biodistribution of antibodies labeled with pure beta emitters by measuring their bremsstrahlung radiation with a gamma camera (Qian and Clarke, 1996). These two procedures are important tools in the *in vivo* management of antibody radiation therapy. Other potential applications of

multiresolution restoration are scatter compensation on small (< 1 cm) tumor detection in planar scintimammography (Buvat et al., 1997) and increased contrast and signal-to-noise ratio in PET studies (Varga et al., 1997).

In addition, the advantages of multiresolution restoration in denoising images while preserving significant image details could also be exploited. This can be used in denoising Comptom images for scatter compensation (Chapter 2, p. 43 - 44) and transmission data for attenuation correction in PET (Freedman et al., 1996). Comptom images for scatter compensation have been empirically smoothed in order to reduce noise propagation during the subtraction process (Haynor et al., 1995). However, empirical low-pass frequency filters can modify significant image features in Comptom images and introduce artifacts into the scatter compensation process. Similarly, transmission data used for attenuation correction in PET are count-limited, which introduces noisy data into the reconstruction process (Freedman et al., 1996). To compensate for this drawback, smoothing of transmission data by a low-pass frequency filter is commonly used. This smoothing introduces a well known mismatch in resolution between transmission and emission data and consequently errors in attenuation-corrected PET scans (Freedman et al., 1996). Segmentation of noise by multiresolution analysis should avoid the use of empirical low-pass frequency filters and keep significant image details in both Compton images and transmission data in PET. However, further study could be required to explore adaptation of the denoising criterion used in this research to other data sets with different trade-off between signal and noise.

Future Developments

Based on the results obtained with the realistic cardiac chest phantom, one could expect improved sensitivity and specificity for CAD with attenuation-corrected cardiac SPECT and multiresolution restoration. However, clinical validation in different patient populations is necessary to define the real diagnostic benefit of this method. This is needed because good performance in phantom experiments can not always be extended to patient studies. There are two main reasons for this. First, in phantom experiments radioactivity was strictly localized in the cardiac and liver insert, while in patient studies the radiotracer is distributed in several organs producing a very different scatter background. Second, the dimensions of the chest phantom were smaller than those of a normal adult patient. The larger body size of an adult patient means more scatter and photon attenuation. These two factors make the scatter compensation in human studies more difficult than in phantom experiments. In addition, any clinical validation has to include a nonuniform attenuation correction method rather than the uniform Chang's method in order to avoid artifacts due to the nonuniform density of thoracic tissues. However, in order to get an indication on how the multiresolution restoration algorithm works in clinical studies, three patients submitted for adenosine ^{201}Tl cardiac SPECT imaging at the Veteran Administration Medical Center (VAMC) in Gainesville were retrospectively studied.

Patients included in this study had previous myocardial infarction. Therefore, their cardiac SPECT images both at rest and stress had large radiotracer uptake defects that correspond to the necrotic areas (Chapter 2, p. 12). The standard procedure used in the Department of Nuclear

Medicine at VAMC was followed for visual interpretation of SPECT scans. It was performed by an experienced nuclear medicine physician and based on the short, horizontal long and vertical long-axis slices obtained without any correction. These results were compared with those of bull's eye polar map reconstructions without any correction (NC), with attenuation correction only (AC) and with attenuation correction and multiresolution restoration (AC + MR). The most relevant clinical data for the group of three patients are summarized in Table 6.1. Physician interpretation of uncorrected tomographic slices showed two patients with significant antero-lateral ischemia and one patient with no significant ischemia. This last patient had a history of episodes of chest pain but did not have coronary angiography data (Table 6.1). Physician interpretation of uncorrected slices agreed well with bull's eye polar maps of uncorrected and corrected SPECT scans of the first two patients. There were no practical differences between uncorrected and corrected bull's eye polar maps.

In the third patient bull's eye polar maps demonstrated significant differences between uncorrected and corrected SPECT scans (Figure 6-1). Figure 6-1a shows that uncorrected SPECT scans depicted equivalent bull's eye polar maps. These images indicated absence of ischemia induced by the pharmacological stress. Attenuation-corrected SPECT scans (Figure 6-1b) showed a different distribution of counts with an increased activity in the infero-septal region, probably due to the spillover artifact as consequence of attenuation correction. The artifact contribution to stress and rest polar maps look different because the source distribution is also different in nearby abdominal organs (Leppo, 1996; Orlandi, 1996).

Table 6.1

Data of the three patients included in a preliminary evaluation of the multiresolution restoration algorithm in attenuation-corrected cardiac SPECT scans.

Patient	Myocardial Infarction location	Coronary angiography	Physician interpretation of SPECT scans	Additional information
1	Anterior wall	LAD (prox) 95 %	Antero-lateral ischemia	-
2	Anterior wall	RCA (prox) 100% LAD (prox) 100% Cx (mid) 30%	Antero-lateral ischemia	-
3	Inferior wall	-	No significant ischemia	Episodes of chest pain

LAD: Left anterior descending. RCA: Right coronary artery. Cx: Circumflex artery. prox: Proximal. mid: Middle.

Finally, Figure 6-1c shows bull's eye polar maps of SPECT scans corrected for both attenuation and multiresolution restoration. In these images spillover artifact has dissapeared and a small but significant ischemic region is observed in the infero-lateral segment (Figure 6-1c). This result suggests the good performance of the multiresolution method in compensating scatter in real clinical situations and its potential utility in improving diagnostic accuracy in attenuation-corrected SPECT scans. However, a main limitation of this preliminary assessment of the multiresolution algorithm in clinical studies is that the Chang uniform attenuation correction method used in this research could introduce significant artifacts in patient studies. A rigorous demonstration of the clinical usefulness of the proposed method should require a clinical

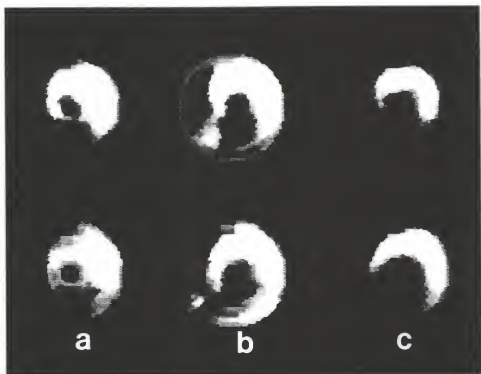


Figure 6-1. Bull's eye polar maps of patient number 3 (inferior myocardial infarction). Top row corresponds to adenosine stress images. Bottom row corresponds to rest images. a: No correction. b: Attenuation correction only. c: Attenuation correction and multiresolution restoration including scatter and geometric corrections. Uncorrected images (a) showed no significant ischemic defects. Attenuation-corrected images (b) are distorted by spillover artifacts, while Images corrected for attenuation and multiresolution restoration (c) exhibit an apparent infero-lateral ischemic defect and no spillover artifact.

research protocol including a non-uniform attenuation correction method.

An additional limitation of restoration by deconvolution with a point spread function is that no single function can describe the complete degrading processes in a SPECT system. Shift-invariant point spread functions have been used as a valid approximation in the clinical setting. This approach has demonstrated qualitative and quantitative improvement in the detection of tumors (Penney et al., 1990; King et al., 1991; Smith et al., 1997), deblurring of cardiac and brain SPECT scans (Frei and Tsui, 1995; Smith, 1995), imaging of beta emitters by bremsstrahlung radiation and improved resolution in PET (Bentourkia et al., 1996; Varga et al., 1997). Glick et al. (1991) demonstrated little difference between Wiener restoration with a shift-invariant point spread function and with a shift-variant correction model in imaging simulated liver spherical tumors (2.5 cm in diameter). However, it is known that the depth-dependence of the detector response function can result in geometrical distortions of small off-center objects and quantitative inaccuracies (Glick et al., 1994). Thus, the depth-dependence or shift variance of detector response function which could be irrelevant in some clinical studies may become an important source of artifacts in others.

Quantitation of myocardial wall thickening in gated SPECT/PET studies (Bartlett et al., 1996) is a current problem in which shift-variant resolution recovery seems to be critical. This is a relatively new procedure in which myocardial perfusion images are obtained at different times in the cardiac cycle, specifically at end-diastole (lowest thickness) and at end-systole (highest thickness). Clinical studies require quantitation of both thickness (Porenta et al., 1994; Bartlett et

al., 1995; 1996). The accuracy of these calculations is affected by the partial volume effect (Bartlett et al., 1995). This effect causes the activity concentration to be underestimated in a nonlinear relationship when the size of the object is less than double the FWHM of the point spread function of the imaging system (Bartlett et al., 1995; 1996). The FWHM of current SPECT/PET systems is depth-dependent and ranges from 7 mm to 16 mm while myocardial wall thickness is around 10 mm at end-diastole and 15 mm at end-systole. Several approaches have been proposed to overcome this drawback (Porenta et al., 1994; Bartlett et al., 1995; 1996), but the most direct and accurate is the correction of the depth-dependent detector response function. Results of this research demonstrated that restoration based on a shift-invariant model is not sufficient. The best estimations of myocardial wall thickness had relative errors larger than 50% with shift-invariant multiresolution restoration (Figure 5-4).

In theory, 3-D shift-variant restoration can be performed by using iterative reconstruction techniques (Chapter 2, p. 52 - 59), but so far these methods are not practical for clinical studies (Chapter 2, p. 57 - 59). Noniterative depth-dependent restorations have been performed on the 3-D sinogram (Chapter 2, p. 32) in the frequency domain using the frequency distance principle (FDP) and regularization by a modified Wiener filter (Glick et al., 1991; 1994). The FDP states that points in the object at a specific source-detector distance provide the most significant contribution to specific regions of the sinogram in the frequency domain. Thus, restoration of the sinogram in the frequency domain using a depth-dependent MTF may compensate the detector geometric response (Glick et

al., 1994). This method has been successfully applied in experimental and simulated data (Glick et al., 1991; 1994). Recently, another noniterative shift-variant restoration method has been proposed (Engdahl and Links, 1995). It combines inverse depth-dependent MTFs with a low-pass Butterworth filter. Projections are backprojected before filtering and then filtered row by row by using a different depth-dependent filter for each row. A major inconvenience of these methods is the filter optimization design. This drawback can be overcome by multiresolution restoration. In a shift-variant model, scatter could be compensated by a window-energy subtraction method, such as the dual-window energy (Chapter 2, p. 44) while shift-variant detector geometric response is corrected by multiresolution restoration. Problems to investigate are the optimal number of resolution levels, rim artifacts and continuity of the depth-dependent restoration algorithm. However, because of the advantages of multiresolution restoration and the encouraging results from this research, the extension of the method to 3-D corrections with shift-variant response functions seems worthy of further investigation.

APPENDIX A COMPUTER IMPLEMENTATION OF A METZ FILTER

All calculations and algorithms were implemented in MATLAB code. In order to simplify the notation mathematical formulations are represented by the same variables and expressions used in computer codes. The MATLAB function codes which appear below were developed specifically for this research.

A1. Calculation of MTF Parameters

Line spread function (LSF) experimental count data were represented by a Gaussian model (Nuyts et al., 1993) given by

$$y = c(1)*\exp(-\lambda(1)*t^2) + c(2)*\exp(-\lambda(2)*t^2),$$

where $c(2) = \lambda(2) = 0$ when the line source was in air. The non-linear terms $\lambda(1)$ and $\lambda(2)$ were fitted to experimental count data by using the Levenberg-Marquardt algorithm (Nuyts et al., 1993). Calculations were performed using the following MATLAB functions

```
data = lftlwa;
options = optleast;
lam = [0.0902 0.0034];
l = leastsq('fitfun2',lam,options,[],data);
c = lileast(f,data);
```

where *data* is the file containing the LSF count data to fit, *options* includes the variables containing fit options used in optimization routines in MATLAB, *lam* is a two-dimensional variable containing initial values of $\lambda(1)$ and $\lambda(2)$, *leastsq* implements the Levenberg-Marquardt

algorithm, fitfun2 includes the function to be fitted. When the source was in free air, the function fitgaus was used instead of fitfun2. Finally, lileast calculates c(1) and c(2) using the linear least squares method and the chi-square of the fit.

MATLAB Functions

a) fitfun2.m

```
function f = fitfun2(lam,data)
%
% Function definition to be used with LEASTSQ, non-linear
% least squares Levenberg-Marquardt algorithm.
%
% fitfun2 defines two Gaussians for fitting LSF data
%
%      y = c(1)*exp(-lam(1)*t^2) + c(2)*exp(-lam(2)*t^2)
%
t = data(:,1); y = data(:,2);
A = zeros(length(t),length(lam));
for j = 1:size(lam)
for i = 1:size(t)
A(i,j) = exp(-lam(j)*t(i)*t(i));
end
end
c = a\y;
z = a*c;
f = z-y;
```

b) fitgaus.m

```
function f = fitgaus(lam,data)
%
% Function definition to be used with LEASTSQ, non-linear
% least squares Levenberg-Marquardt algorithm.
%
% fitgaus defines a simple Gaussian for fitting LSF data in
% free air.
%
%      y = c*exp(-lam*t^2)
%
t = DATA(:,1); y = DATA(:,2);
A = zeros(length(t),1);
for i = 1:size(t)
A(i,1) = exp(-lam*t(i)*t(i));
end
c = a\y;
z = A*c;
f = z - y;
```

c) lileast.m

```
function c = lileast(lam,data)
%
% Fit of LSF data to a double Gaussian
% Calculation of linear coefficients and Chi-square
%
t = data(:,1);
y = data(:,2);
st = t.*t;
e1 = exp(-lam(1)*st);
e2 = exp(-lam(2)*st);
e12 = exp(-(lam(1)+lam(2))*st);
e21 = exp(-2*(lam(1)*st));
e22 = exp(-2*lam(2)*st);
DET = sum(e21)*sum(e22)-sum(e12)^2;
c(1) = (sum(y.*e1)*sum(e22) - sum(y.*e2)*sum(e12))/DET;
c(2) = (sum(y.*e2)*sum(e21) - sum(y.*e1)*sum(e12))/DET;
g = c(1)*exp(-lam(1)*st) + c(2)*exp(-lam(2)*st);
c(3) = sum((y-g).* (y-g)./(g.*g));
```

d) optleast.m

```
function options = optleast
%
% Definition of options for fitting LSF.
% Meaning of options is displayed by "help foptions"
%
OPTIONS(1) = 0;
OPTIONS(2) = 0.001;
OPTIONS(3) = 0.0001;
OPTIONS(4) = 0.0;
OPTIONS(5) = 0;
OPTIONS(6) = 0;
OPTIONS(7) = 1.0;
OPTIONS(8) = 0.1477;
OPTIONS(9) = 0;
OPTIONS(10) = 48.0;
OPTIONS(11) = 0;
OPTIONS(12) = 0;
OPTIONS(13) = 0;
OPTIONS(14) = 200.0;
OPTIONS(15) = 0;
OPTIONS(16) = 0.0;
OPTIONS(17) = 0.1;
OPTIONS(18) = 1.0;
```

e) lftcwa.m

```

function data = lftcwa
%
% Line spread data of Tc-99m source in water
% Arithmetic mean of counts in conjugate opposed projections
% Jaszczak phantom, central position
% Collimator: HRLE
% Frame: 128 x 128
% Pixel size: 0.356 cm
% Radius of rotation: 24 cm
% SPECT: TRIAD VAMC
% Date: July 8 1996
% Data = [pixel_position relative_counts]
%
DATA =...
[-27 11, -26 16, -25 12, -24 20, -23 20, -22 27, -21 24, -20 40, -19 55, -18 70, -17 78, -16 90, -15 99, -14 137, -12 154, -11 180, -10 215, -9 239, -8 248, -7 302, -6 383, -5 481 -4 778, -3 2303, -2 5768, -1 9738, 0 11290, 1 8429, 2 4327, 3 1494, 4 631, 5 444, 6 355, 7 318, 8 266, 9 243, 10 190, 11 173, 12 166, 13 131, 14 101, 15 96, 16 84, 17 70, 18 44, 19 49, 20 33, 21 36, 22 29, 23 21, 24 19, 25 16, 26 16, 17 15];

```

f) lftlai.m

```

function data = lftlai
%
% Line spread data of Tl-201 source in air
% Arithmetic mean of counts in conjugate opposed projections
% Jaszczak phantom, central position
% Collimator: LEGP
% Frame: 128 x 128
% Pixel size: 0.356 cm
% Radius of rotation: 24 cm
% SPECT: TRIAD VAMC
% Date: July 8 1996
% Data = [pixel_position relative_counts]
%
DATA =...
[-27 24, -27 12, -25 15, -24 6, -23 27, -22 21, -21 18, -20 6, -19 27, -18 24, -17 18, -16 6, -15 15, -14 21, -13 12, -12 21, -11 27, -10 39, -9 45, -8 66, -7 54, -6 99, -5 675, -4 1968, -3 3813, -2 5907, -1 7248, 0 8050, 1 7134, 2 5568, 3 3357, 4 1638, 5 498, 6 99, 7 30, 8 30, 9 42, 10 33, 11 21, 12 24, 13 21, 14 33, 15 24, 16 21, 17 15, 18 24, 19 9, 20 27, 21 6, 22 18, 23 24, 24 19, 25 27, 26 12, 27 21];

```

g) lftcai.m

```
function data = lftcai
%
% Line spread data of Tc-99m source in air
% Arithmetic mean of counts in conjugate opposed projections
% Jaszczak phantom, central position
% Collimator: HRLE
% Frame: 128 x 128
% Pixel size: 0.356 cm
% Radius of rotation: 24 cm
% SPECT: TRIAD VAMC
% Date: July 8 1996
% Data = [pixel_position relative_counts]
%
DATA =...
[-27 3, -26 4, -25 10, -24 4, -23 11, -22 9, -21 12, -20 15, -19 18, -18
27, -17 41, -16 30, -15 36, -14 44, -13 42, -12 47, -11 45, -10 56, -9 38,
-8 65, -7 56, -6 116, -5 198, -4 1032, -3 6433, -2 20391, -1 39405, 0
50433, 1 41832, 2 23037, 3 7358, 4 983, 5 186, 6 104, 7 72, 8 71, 9 51,
10 53, 11 38, 12 50, 13 33, 14 39, 15 32, 16 38, 17 21, 18 24, 19 17, 20
13, 21 16, 22 9, 23 11, 24 9, 25 6, 26 6, 27 5];
```

h) lftlwa.m

```
function data = lftlwa
%
% Line spread data of Tl-201 source in water
% Arithmetic mean of counts in conjugate opposed projections
% Jaszczak phantom, central position
% Collimator: LEGP
% Frame: 128 x 128
% Pixel size: 0.356 cm
% Radius of rotation: 24 cm
% SPECT: TRIAD VAMC
% Date: July 8 1996
% Data = [pixel_position relative_counts]
%
DATA =...
[-27 16, -26 21, -25 22, -24 19, -23 26, -22 30, -21 33, -20 34, -19 27, -18
22, -17 48, -16 42, -15, 52, -14 57, -13 89, -12 104, -11 76, -10 95, -9
95, -8 92, -7 125, -6 177, -5 257, -4 445, -3 761, -2 1098, -1 1338, 0
1458, 1 1233, 2 984, 3 668, 4 392, 5 183, 6 137, 7 119, 8 82, 9 78, 10 94,
11 58, 12 58, 13 48, 14 58, 15 42, 16 32, 17 38, 19 32, 20 25, 21 35, 22
19, 23 24, 24 13, 25 20, 26 21, 27 9];
```

A2. Simulation of a Cardiac - Liver Projection

Degraded projections were simulated in MATLAB as follows:

```
h = heart;
l = liver;
o = h+l;
k=psft;
h = conv2(k,o,'same');
h=noise(h);
```

where heart simulates the cardiac projection, liver simulates the liver, psftc generates the ^{99m}Tc -point spread function, conv2 is the MATLAB function which performs 2-D convolution between two images, and noise generates the additive noise.

MATLAB FUNCTIONS

a) heart.m

```
function h = heart
h = zeros(128,128);
a = 100;
for i = 1:128
for j = 1:128
h(i,j) = 0.15*a;
end
end
% Myocardium Outer Shell
for x = -23:0
y = round(81 - 0.096*x*x);
for y = 30:81
for i = 64+x:64-x
h(i,y)=a + h(i,y);
end
end
end
% Myocardium Inner Shell
for x = -17:0
y = round(75 - 0.096*x*x);
for y = 30:75
for i = 64+x:64-x
h(i,y) = h(i,y) - a;
end
end
end
```

b) liver.m

```
function l = liver
l = zeros(128,128);
a = 100;
r = 1.5;
yo = 6;
for i = 16:73
for j = 81 + yo:93+yo
l = r*a;
end
end
```

c) psftc.m

```
% Generate two-dimensional Point Spread Function for Tc source in water
% The matrix is in the spatial domain for use as a convolution mask
%
% Author: J.M. Franquiz
% Date: August 1996
k=zeros(128,128);
sum=0;
for i=1:28
for j=1:28
k(i,j)=2834.9*exp(-((i-14)^2+(j-14)^2)*0.2158);
k(i,j)=k(i,j)+19.525*exp(-((i-14)^2+(j-14)^2)*0.0066);
sum=sum+k(i,j);
end
end
for i=1:28
for j=1:28
k(i,j)=k(i,j)/sum;
end
end
```

d) noise.m

```
function n = noise(h)
n = zeros(128,128);
for i = 1:128
for j = 1:128
n(i,j) = h(i,j) + round(randn(1,1)*sqrt(h(i,j)));
if n(i,j) < 0
n(i,j) = 0;
end
end
```

A3. METZ FILTERING

Filtering operations were performed in the frequency domain. The sequence of operations is as follows

```
fil = tcmetz(128,128,x);
fil = ifft2(fft2(h).*fil);
nmse = nmse(o,fil);
```

where tcmetz defines the Metz filter and fft2 and ifft2 are the 2-D Fourier transform and its inverse, respectively. The normalized mean square error is calculated using nmse.

MATLAB FUNCTIONS

a) tcmetz.m

```
function fil = tcmetz(xc,yc,x)
% Generate two-dimensional Metz filter in the frequency domain
% using the representative MTF of the system.
% xc and yc: dimensions of the frame
% x: potential factor
% This function contains the MTF for Tc99m in water.
% Author: J.M. Franquiz
% Date: March 1996
fm = zeros(xc,xc);
A1 = 0.82;
A2 = 0.18;
lam(1) = 0.00279;
lam(2) = 0.09127;
    % First quadrant
for i = 1:xc/2
for j = 1:yc/2
aux = A1*exp(-lam(1)*((i-1)^2+(j-1)^2)) + A2*exp(-lam(2)*((i-1)^2+(j-1)^2));
fil(i,j) = (1 - (1-aux^2)^x)/aux;
end
end
    % Second quadrant
for i = xc/2+1:xc
for j = 1:yc/2
aux = A1*exp(-lam(1)*((i-xc)^2+(j-1)^2))+A2*exp(-lam(2)*((i-xc)^2+(j-1)^2));
fil(i,j) = (1 - (1-aux^2)^x)/aux;
end
end
    % Third quadrant
for i = 1:xc/2
for j = yc/2+1:yc
```

```
aux = A1*exp(-lam(1)*((i-1)^2+(j-yc)^2))+A2*exp(-lam(2)*((i-1)^2+(j-yc)^2));
fil(i,j)=(1-(1-aux^2)^x)/aux;
end
end
% Fourth quadrant
for i = xc/2+1:xc
for j = yc/2+1:yc
aux = A1*exp(-lam(1)*((i-xc/2)^2+(j-yc/2)^2))+A2*exp(-lam(2)*((i-xc/2)^2+(j-yc/2)^2));
fil(i,j)=(1-(1-aux^2)^x)/aux;
end
end
```

b) nmse.m

```
function n = nmse(o,h)
sum1=0;
sum2=0;
for i=35:83
for j=45:83
sum1=sum1+(o(i,j)-h(i,j))^2;
sum2=sum2+h(j,i)^2;
end
end
n=sum1*100/sum2;
```

APPENDIX B MULTIRESOLUTION DECOMPOSITION AND RESTORATION ALGORITHMS

Analyzing functions used in multiresolution decomposition and restoration of images are represented by grey_i and gl28_i for 128 x 64 and 128 x 128 pixels matrix, respectively. When i = 3 the function represents the coarse approximation. Index values of i = 2, 1, 0 and 11 represent pass-band filter functions. These functions were generated using the program mphis.c developed by Prof. Andrew Laine.

B1. Multiresolution Decomposition

Multiresolution image decomposition and calculation of the square ℓ_2 norm was performed by

```
res = decomp(x,y,filename);
```

where x and y are the number of pixels of the image in the X and Y coordinates respectively, and filename is the image to be decomposed. The output of this function is five 2-D wavelet coefficients or sub-band images imai (i = 3, 2, 1, 0, 11) and the square ℓ_2 norm of each sub-band image. The coarse approximation is given by ima3, while the last frequency sub-band image is given by imall.

MATLAB Function

decomp.m

```
function res = decomp(x, y, filename)
```

```
*****
%* MATLAB FILE: decomp.m *
%* PURPOSE: Wavelet decomposition and energy *
%* calculation of 128x64 or 128x128 frames *
%* using the FJT. *
%* USAGE: ima=decomp(x,y,'filename') *
%* (filename is UNIX file) *
%* DATE: October 1996 *
%* AUTHOR: J.M. Franquiz *
*****
ima=zeros(x,y);
res=zeros(x,y);
fid=fopen(filename,'r','b');
ima=fread(fid,[x,y],'float');
% 128 x 64 matrix:
if y==64
fid=fopen('grey_3','r');
g3=fread(fid,[128,64]);
fid=fopen('grey_2','r');
g2=fread(fid,[128,64]);
fid=fopen('grey_1','r');
g1=fread(fid,[128,64]);
fid=fopen('grey_0','r');
g0=fread(fid,[128,64]);
fid=fopen('grey_+1','r');
gll=fread(fid,[128,64]);
end
% 128 x 128 matrix:
if y==128
fid=fopen('g128_3','r');
g3=fread(fid,[128,128]);
fid=fopen('g128_2','r');
g2=fread(fid,[128,128]);
fid=fopen('g128_1','r');
g1=fread(fid,[128,128]);
fid=fopen('g128_0','r');
g0=fread(fid,[128,128]);
fid=fopen('g128+1','r');
gll=fread(fid,[128,128]);
end
g3=g3/255;
g2=g2/255;
g1=g1/255;
g0=g0/255;
gll=gll/255;
g3=g3.*g3;
g2=g2.*g2;
g1=g1.*g1;
g0=g0.*g0;
gll=gll.*gll;
g3=fftshift(g3);
g2=fftshift(g2);
```

```

g1=fftshift(g1);
g0=fftshift(g0);
g11=fftshift(g11);
% Components definition:
four=fft2(im1);
ima3=abs(ifft2(four.*g3));
ima2=abs(ifft2(four.*g2));
imal=abs(ifft2(four.*g1));
ima0=abs(ifft2(four.*g0));
imall=abs(ifft2(four.*g11));
sum(sum(ima))
pause
sum(sum(ima.*ima))
sum(sum(ima3.*ima3))
sum(sum(ima2.*ima2))
pause
sum(sum(imal.*imal))
sum(sum(ima0.*ima0))
sum(sum(imall.*imall))
% Storing components
res =ima3;
fid=fopen('ima3','w','b');
fwrite(fid,res,'float');
res=ima2;
fid=fopen('ima2','w','b');
fwrite(fid,res,'float');
res=imal;
fid=fopen('imal','w','b');
fwrite(fid,res,'float');
res=ima0;
fid=fopen('ima0','w','b');
fwrite(fid,res,'float');
res=imall;
fid=fopen('imall','w','b');
fwrite(fid,res,'float');

```

B2. Multiresolution Restoration

Multiresolution restoration algorithm was implemented by

```

q = cls(x,y,n);
i0 = fftshift(invtc(x,y,0,q));
i1 = fftshift(invtc(x,y,0.005,q));
fil = i0.* (g3+g2)+i1.*g1;

```

where `cls` generates the 2-D smoothness constraint operator (Chapter 3, p. 108), `fftshift` is a MATLAB operator which rearrange data in the frequency domain by moving the zero frequency component to the center of the array,

invtc generates the 2-D inverse MTF for ^{99m}Tc data. A similar function invtl exists for ^{201}Tl data. Finally, fil contains the 2-D restoration algorithm.

MATLAB FUNCTIONS

a) cls.m

```
function q=cls(xc,yc,n)
% Generate an exponential operator in the frequency domain for restoration
% operations using the constrained least squares (CLS) regularization
% approach (Gonzalez and Wintz, 1977, p. 214 - 216)
%
% xc and yc: dimensions of the frame
% n = exponent
%
%
% This function is used for SPECT image restoration using the Frazier
% Javerth Transform.
%
%
% Author: J.M. Franquiz
% Date: March 1996
q=zeros(xc,yc);
for i=1:xc
    for j=1:yc
        q(i,j)=exp(n*sqrt((i-xc/2)^2 + (j-yc/2)^2));
    end
end
```

b) invtc.m

```
function inv=invtc(xc,yc,lam,q)
% Generate two-dimensional inverse MTF in the frequency domain
% for Tc99m.
%
% xc and yc: dimensions of the frame
% lam: Regularization parameter
% q: Laplacian operator in the frequency domain
% This function is used for SPECT images restoration using the Frazier
% Javerth Transform.
%
%
% Author: J.M. Franquiz
% Date: March 1996
inv=zeros(xc,yc);
A1=2.5066283*10817*1.522;
A2=2.5066283*426*8.704;
A1=A1/(A1+A2);
A2=1-A1;
```

```
for i=1:xc
for j=1:yc
aux=A1*exp(-0.00279*((i-xc/2)^2+(j-yc/2)^2))
+A2*exp(-0.09127*((i-xc/2)^2+(j-yc/2)^2));
inv(i,j)=aux/(aux^2+lam*q(i,j)*q(i,j));
end
end
```

APPENDIX C MULTIRESOLUTION RESTORATION OF SPECT PROJECTIONS

C1. Restoration Programs

Restoration of SPECT projections, was performed by:

```
res = tomfilt('filename',fil);
```

where filename is the SPECT file and fil is the restoration algorithm.

MATLAB Function

```
function r = tomfilt(filename, filter)
%*****
%* MATLAB FILE: tomfilt.m
%* PURPOSE: Pre-reconstruction filtering of SPECT
%*           projections using a filter function
%*           defined in matlab by "filter".
%* USAGE: r = tomfilt('filename',filter)
%*           (filename is UNIX file)
%* DATE: October 1996
%* AUTHOR: J.M. Franquiz
%*****
fid=fopen(filename,'r','b');
s=fread(fid,[128,11520],'float');
r=zeros(128,11520);
% Reading of n-th image
for n=1:180
aux=zeros(128,64);
    for i=(n-1)*64+1:n*64
        for j=1:128
            aux(j,i-(n-1)*64) = s(j,i);
        end
    end
% Fourier filtering of the n-th image
    four=fft2(aux);
    aux=real(ifft2(four.*filter));
% Storing filtered image
    for i=1:64
        for j=1:128
            if aux(j,i)<0
                aux(j,i)=0;
            end
            r(j,i+(n-1)*64)=aux(j,i);
        end
    end
end
```

```

    end
    end
end
% writing filtered image
fid=fopen(filename,'w','b');
counts = fwrite(fid,r,'float')

```

Utility Programs

a) trigro.c

```

/****************************************************************************
 * PROGRAM: TRIGRO                                     */
/* PURPOSE: To transfer images from TRIAD to GROVE      */
/* DATE: Aug. 96                                         */
/* AUTHOR: J.M. Franquiz                                */
/* USAGE: TRIGRO xsize ysize triad_file                */
/*        OUTPUT: triad_file.GRO (data in FLOAT)          */
/* COMMENTS:                                              */
/****************************************************************************
 # include <stdio.h>
# include <string.h>
# include <sys/file.h>
# include <stdlib.h>
# include <math.h>
char *calloc();
main(argc,argv)
int argc;
char *argv[];
{
    int xsize, ysize, i;
    FILE *in, *out;
    char *infile[8], *outfile[8];
    float *float_buf;
    short *short_buf;
    xsize=atoi(argv[1]);
    ysize=atoi(argv[2]);
    short_buf=(short*)(calloc(xsize*ysize,sizeof(short)));
    float_buf=(float*)(calloc(xsize*ysize,sizeof(float)));
    strcpy(infile,argv[3]);
    strcpy(outfile,argv[3]);
    strcat(outfile,".gro");
    in=fopen(infile,"rb");
    fread(short_buf,sizeof(short),xsize*ysize,in);
    for(i=0;i<=xsize*ysize-1;i++)
    {
        float_buf[i]=short_buf[i];
    }
    out=fopen(outfile,"wb");
    fwrite(float_buf,sizeof(float),xsize*ysize,out);
    fclose(in);
}

```

```
    fclose(out);
}
```

b) grotri.c

```
*****
/*  PROGRAM: GROTRI                         */
/*  PURPOSE: To transfer images from GROVE to TRIAD   */
/*  DATE: Aug. 96                                */
/*  AUTHOR: J.M. Franquiz                         */
/*  USAGE: GROTRI xsize ysize grove_file        */
/*  OUTPUT: gove_file.TRI (data in SHORT)         */
/*  COMMENTS:                                     */
*****
```

```
# include <stdio.h>
# include <string.h>
# include <sys/file.h>
# include <stdlib.h>
# include <math.h>
char *calloc();
main(argc,argv)
int argc;
char *argv[];
{
    int xsize, ysize, i;
    FILE *in, *out;
    char *infile[8], *outfile[8];
    float *float_buf;
    short *short_buf;
    xsize=atoi(argv[1]);
    ysize=atoi(argv[2]);
    short_buf=(short*)(calloc(xsize*ysize,sizeof(short)));
    float_buf=(float*)(calloc(xsize*ysize,sizeof(float)));
    strcpy(infile,argv[3]);
    strcpy(outfile,argv[3]);
    strcat(outfile,".tri");
    in=fopen(infile,"rb");
    fread(float_buf,sizeof(short),xsize*ysize,in);
    for(i=0;i<=xsize*ysize-1;i++)
    {
        short_buf[i]=float_buf[i];
    }
    out=fopen(outfile,"wb");
    fwrite(float_buf,sizeof(float),xsize*ysize,out);
    fclose(in);
    fclose(out);
}
```

C2. Analysis Programs

a) fsd.c

```

/* PROGRAM: fsd*/
/* PURPOSE: To calculate fractional standard deviation in myocardial*/
/* SPECT slices*/
/* DATE: December 1996*/
/* AUTHOR: Juan M Franquiz*/
/* USAGE: fsd xsize ysize file*/
/* Output: FSD*/
# include <stdio.h>
# include <string.h>
# include <sys/file.h>
# include <stdlib.h>
# include <math.h>
char *calloc();
main(argc,argv)
int argc;
char *argv[];
{
    int xsize, ysize, i, m, n;
    FILE *in;
    char *infile[8];
    short *short_buf;
    float fsd, half,sum,sumsq;
    xsize = atoi(argv[1]);
    ysize = atoi(argv[2]);
    short_buf = (short*)(calloc(xsize*ysize,sizeof(short)));
    strcpy(infile,argv[3]);
    in = fopen(infile,"rb");
    fread(short_buf,sizeof(short),xsize*ysize,in);
    sumsq=0.0;
    sum=0.0;
    n=0;
    m = short_buf[1];
    for(i= 2; i<=xsize*ysize-1;i++)
    {
        if(m<short_buf[i])
        {
            m = short_buf[i];
        }
        half = m/2.0;
        for(i=0;i<=xsize*ysize-1;i++)
        {
            if (short_buf[i]>=half)
            {
                n = n+1;
                sum = sum +short_buf[i];
                sumsq = sumsq +short_buf[i]*short_buf[i];
            }
        }
    }
}

```

```

}
fsd = sumsq/(n-1) - sum*sum/(n*(n-1));
fsd= sqrt(fsd)*n/sum;
printf("%f", fsd);
getchar();
fclose(in);
}

```

b) chisqbe.c

```

/*********************************************
/*  PROGRAM: CHISQBE.C                      */
/*  PURPOSE: To calculate chi-square between two bullseye   */
/*          images                                */
/*  DATE: July 96                               */
/*  AUTHOR: J.M. Franquiz                         */
/*  USAGE: CHISBE OBJBE TESTBE                  */
/*          OBJBE: Object bullseye             */
/*          TESTBE: Test bullseye              */
/*  OUTPUT: Chi-square, number of data          */
/*  COMMENTS:                                     */
/*********************************************
# include <stdio.h>
# include <string.h>
# include <sys/file.h>
# include <math.h>
# include <stdlib.h>
char *calloc();
main(argc,argv)
int argc;
char *argv[];
{
    short *obj, *test;
    int xint, yint, i, coor;
    FILE *inobj, *intest;
    char *fobject[8], *ftest[8];
    float sumi, numi, serror;
    obj = (short*)(calloc(256*256,sizeof(short)));
    test = (short*)(calloc(256*256,sizeof(short)));
    strcpy(fobject,argv[1]);
    strcpy(ftest,argv[2]);
    inobj=fopen(fobject,"rb");
    fread(obj,sizeof(short),256*256,inobj);
    intest=fopen(ftest,"rb");
    fread(test,sizeof(short),256*256,intest);
    sumi=0.0;
    numi=0.0;
    serror=0.0;
    for (yint=0;yint<=255;yint++)
    {
        for (xint=1;xint<=255;xint++)

```

```

{
if ((xint-127)*(xint-127) + (yint-127)*(yint-127)<=5930)
{
    coor=yint*256+xint;
    numi=numi+1;
sumi=sumi+(obj[coor]-test[coor])*(obj[coor]-test[coor])/obj[coor];
serror=serror+(obj[coor]-test[coor])*(obj[coor]-test[coor]);
}
/* end IF (x-127)^2..... */
}
/* end for (y=0..... */
}
/* end for (x=0..... */
fclose(inobj);
fclose(intest);
serror=serror/numi;
printf("%f\n",sumi);
getchar();
printf("%f\n",serror);
getchar();
printf("%f",numi);
getchar();
}


```

c) histbe.c

```

/*********************************************
/* PROGRAM: HISTBE.C
/* PURPOSE: To calculate histogram, average and SD of
/*          Bullseye images
/*          DATE: July 96
/*          AUTHOR: J.M. Franquiz
/*          USAGE: HISTBE bulleye_file
/*          OUTPUT: infile.vec, one dimensional float vector
/*          containing the histogram (5% intervals, start
/*          in >95% and end in < 45%; 12 class), the average
/*          and the standard deviation
/* COMMENTS:
/*********************************************
# include <stdio.h>
# include <string.h>
# include <sys/file.h>
# include <math.h>
# include <stdlib.h>
char *calloc();
main(argc,argv)
int argc;
char *argv[];
{
    float *his;
    short *bul;
```

```

int xint, yint, i, coor;
FILE *in, *out;
char *infile[8], *outfile[8];
float sumi, sumsqi, numi;
bul = (short*)(calloc(256*256,sizeof(short)));
his = (float*)(calloc(14,sizeof(float)));
strcpy(infile,argv[1]);
strcpy(outfile,argv[1]);
strcat(outfile,".vec");
in=fopen(infile,"rb");
fread(bul,sizeof(short),256*256,in);
printf("%d",bul[16256]);
sumsqi=0.0;
sumi=0.0;
numi=0.0;
for(i=0;i<=13;i++)
{
    his[i]=0.0;
}
for (yint=0;yint<=255;yint++)
{
for (xint=1;xint<=255;xint++)
{
if ((xint-127)*(xint-127) + (yint-127)*(yint-127)<=5930)
{
coor=yint*256+xint;
numi=numi+1;
sumi=sumi+bul[coor];
sumsqi=sumsqi+bul[coor]*bul[coor];
if (bul[coor] <=45)
    his[11]=his[11]+1.0;
else if (bul[coor]>45 && bul[coor]<=50)
    his[10]=his[10]+1.0;
else if (bul[coor]>50 && bul[coor]<=55)
    his[9]=his[9]+1.0;
else if (bul[coor]>55 && bul[coor]<=60)
    his[8]=his[8]+1.0;
else if (bul[coor]>60 && bul[coor]<=65)
    his[7]=his[7]+1.0;
else if (bul[coor]>65 && bul[coor]<=70)
    his[6]=his[6]+1.0;
else if (bul[coor]>70 && bul[coor]<=75)
    his[5]=his[5]+1.0;
else if (bul[coor]>75 && bul[coor]<=80)
    his[4]=his[4]+1.0;
else if (bul[coor]>80 && bul[coor]<=85)
    his[3]=his[3]+1.0;
else if (bul[coor]>85 && bul[coor]<=90)
    his[2]=his[2]+1.0;
else if (bul[coor]>90 && bul[coor]<=95)
    his[1]=his[1]+1.0;
else
}
}
}

```

```
    his[0]= his[0]+1.0;
}
/* end IF (x-127)^2.....
}
/* end for (y=0.....
}
/* end for (x=0.....
his[12]=sumi/numi;
his[13] = (sumsqi-(sumi*sumi/numi))/(numi-1);
for(i=0;i<=13;i++)
{
printf("%f",his[i]);
getchar();
}

out=fopen(outfile,"wb");
fwrite(his,sizeof(float),14,out);
fclose(out);
}
```

REFERENCES

- Algazi VR, Ford GE and Chen H (1995), Linear filtering of images based on properties of vision. IEEE Trans. Ima. Proc. 4: 1460 - 1462.
- Andrew HC and Hunt H (1977), Digital Image restoration, Englewood Cliffs, Prentice Hall, NJ.
- Attix FH (1986), Introduction to Radiological Physics and Radiation Dosimetry, John Wiley & Sons, New York.
- Barbarisi MJ, Araujo LI, McClellan JR and Alavi A (1997), Attenuation correction improves the assessment of lateral wall perfusion defects on SPECT imaging. J. Nucl. Med. 38: 84P.
- Bartlett ML, Bacharach SL, Voipio-Pulkki LM and Dilsizian V (1995), Artifactual inhomogeneities in myocardial PET and SPECT scans in normal subjects. J. Nucl. Med. 36: 188 - 195.
- Bartlett ML, Buvat I, Vaquero JJ, Mok D, Dilsizian V and Bacharach SL (1996), Measurement of myocardial wall thickening from PET/SPECT images: Comparison of two methods. J. Comp. Ass. Tomog. 20: 437 - 481.
- Beekman FJ, Frey EC, Kamphuis C, Tsui BW and Viergever MA (1994), A new phantom for fast determination of the scatter response of a gamma camera. IEEE Trans. Nucl. Sci. 41: 1481 - 1488.
- Beller GA (1994), Myocardial perfusion imaging with thallium-201. J. Nucl. Med. 35: 674 - 680.
- Beller GA and Watson DD (1991), Physiological basis of myocardial perfusion imaging with the technetium 99m agents. Sem. Nucl. Med. 21: 173 - 181.
- Bellini S, Placentini M, Cafforio C and Roca F (1979), Compensation of tissue absorption in emission tomography. IEEE Trans. Accous. Speech and Signal Proc. 27: 213 - 218.
- Bentourkia M, Msaki P, Cadorette J and Lecomte R (1996), Nonstationary scatter subtraction-restoration in high-resolution PET. J. Nucl. Med. 37: 2040 - 2046.

- Berman DS, Kiat H, Van Train K, Garcia EV, Friedman J and Maddahi J (1991), Technetium 99m sestamibi in the assessment of chronic coronary artery disease. *Sem. Nucl. Med.* 21: 190 - 212.
- Beyer WH (1984), CRC Standard Mathematical Tables, 27 th Edition. CRC Press, Inc., Boca Raton, Florida.
- Borello JA, Clinthorne NH, Rogers WL, Thrall JH and Keyes JW (1981), Oblique-angle tomography: A restructuring algorithm for transaxial tomographic data. *J. Nucl. Med.* 22: 471 - 473.
- Boulfelfel D, Rangayyan RM, Hahn LJ and Kloiber R (1992), Prereconstruction restoration of myocardial single photon emission computed tomography images. *IEEE Trans. Med. Imag.* 11: 336 - 341.
- Braat SH, Leclercq B, Itti R, Lahiri A, Sridhara B and Rigo P (1994), Myocardial imaging with technetium-99m-tetrofosmin: Comparison of one-day and two-day protocols. *J. Nucl. Med.* 35: 1581 - 1585.
- Bunker SR, Handmaker H and Torre DM (1990), Pixel overflow artifacts in SPECT evaluation of the skeleton. *Radiology* 174: 229 - 232.
- Buvat I, Benali H, Todd-Pokropek A and Di Paola R (1994), Scatter correction in scintigraphy: The state of the art. *Eur. J. Nucl. Med.* 21: 675 - 694.
- Buvat I, De Sousa MC, Di Paola M, Lumbroso J, Ricard M and Aubert B (1997), Impact of scatter correction on tumordetection in planar scintimmamography: A phantom study. *J. Nucl. Med.* 38: 66P.
- Case JA, King MA, Dahlberg ST and Rabin MS (1996), Results of attenuation and scatter correction in clinical cardiac Tl-201 SPECT perfusion imaging. *J. Nucl. Med.* 37: 212P.
- Chang LT (1978), A method for attenuation correction in radionuclide tomography. *IEEE Trans. Nucl. Sci.* 25: 638 - 643.
- Cho Z, Jones JP and Singh M (1993), Foundations of Medical Imaging, John Wiley & Sons, Inc., New York.
- Chua T, Kiat H, Germano G, Takemoto K, Fernandez G, Biasio Y, Friedman J and Berman D (1993), Rapid back to back adenosine stress/rest technetium-99m teboroxime myocardial perfusion SPECT using a triple detector camera. *J. Nucl. Med.* 34: 1485 - 1493.
- Coleman M, King MA, Glick SJ, Knesarek K and Penney BC (1989), Investigation of the stationarity of the modulation transfer function and the scatter fraction in conjugate view SPECT restoration filtering. *IEEE Trans. Nucl. Sci.* 36: 969 - 972.

- Corbett JR, Karabajian MZ, Rose PZ and Ficaro EP (1997), The effect of attenuation correction on cardiac risk assessment using dual isotope myocardial perfusion imaging with rest Tl-201 and stress Tc-99m sestamibi. *J. Nucl. Med.* 38: 83P.
- Cullom SJ (1995), Principles of Cardiac SPECT, in *Cardiac SPECT Imaging*, DePuey EG, Berman DS and Garcia EV (editors), Raven Press, Ltd., New York.
- Cullom SJ, Hendel RC, Liu L, Garcia EV, White ML, Kiat H and Berman DS (1996), Diagnostic accuracy and image quality of a scatter, attenuation and resolution compensation method for Tc-99m sestamibi cardiac SPECT: Preliminary results. *J. Nucl. Med.* 37: 81P.
- Daubechies I (1992), *Ten Lectures on Wavelets*, SIAM, Capital City Press, Montpellier, Vermont.
- DePuey EG (1994), How to detect and avoid myocardial perfusion SPECT artifacts. *J. Nucl. Med.* 35: 699 - 702.
- DePuey EG and Garcia EV (1989), Optimal specificity of thallium-201 SPECT through recognition of imaging artifacts. *J. Nucl. Med.* 30: 441 - 449.
- Donoho DL (1993), Nonlinear wavelet methods for recovery of signals, densities, and spectra from indirect and noisy data. *Proc. Symp. Appl. Math.* 0: 173 - 205.
- Duderstadt JJ and Hamilton LJ (1976), *Nuclear Reactor Analysis*, Wiley, New York.
- Enghdal JC and Links JM (1995), A new approach to filtered backprojection (FBP) reconstruction which facilitates depth-dependent blur correction. *J. Nucl. Med.* 36: 29P.
- Evans RD (1985), *The Atomic Nucleus*, Krieger Publishing Company Malabar, Florida.
- Ficaro EP, Fessler JA, Shreve PD, Kritzman JN, Rose PA and Corbett JR (1996), Simultaneous transmission/emission myocardial perfusion tomography. Diagnostic accuracy of attenuation-corrected 99mTc-sestamibi single-photon emission computed tomography. *Circulation* 93: 463 - 473.
- Franquiz JM, Cardenas R and Garcia D (1983), A computerized method for quantitative analysis of ventricular phase distributions. *Eur. J. Nucl. Med.* 8: 375 - 380.
- Franquiz JM, Garcia D and Cardenas R (1982a), Measurement of right and left ventricular ejection fraction by gated equilibrium scintigraphy using Fourier functional images. *Nucl. Med.* 21: 131 - 137.

Franquiz JM, Garcia D, Lord E and Cardenas R (1982b), Measurement of right ventricular ejection fraction by equilibrium gated nuclear angiography. Comparison of two methods of preprocessing data. Proceedings of the Third World Congress of Nuclear Medicine and Biology, Paris, France, vol. II, 1415 - 1417.

Franquiz JM and Shukla S (1996), Artifacts in Tc-99m myocardial SPECT: Effects of scatter and attenuation compensation. *Med. Phys.* 23: 1179.

Freedman NM, Bacharach SL, Carson RE, Price JC and Dilsizian V (1996), Effect of smoothing during transmission processing on quantitative cardiac SPECT scans. *J. Nucl. Med.* 37: 690 - 694.

Frey EC, Ju ZW and Tsui BW (1993), A fast projector-backprojector pair modelling the asymmetric, spatially varying scatter response function for scatter compensation in SPECT imaging. *IEEE Trans. Nucl. Sci.* 40: 1192 - 1197.

Frey EC and Tsui BW (1990), Parameterization of the scatter response function in SPECT imaging using Monte Carlo simulation. *IEEE Trans. Nucl. Sci.* 37: 1308 - 1315.

Frey EC and Tsui BW (1991), Spatial properties of the scatter response function in SPECT. *IEEE Trans. Nucl. Sci.* 38: 789 - 794.

Frey EC and Tsui BW (1993), A practical method for incorporating scatter in a projector-backprojector for accurate scatter compensation in SPECT. *IEEE Trans. Nucl. Sci.* 40: 1107 - 1116.

Frey EC and Tsui BW (1994), Modeling the scatter response function in inhomogeneous scattering media for SPECT. *IEEE Trans. Nucl. Sci.* 41: 1585 - 1593.

Frey EC and Tsui BW (1995), The importance of combined scatter and attenuation compensation in Tl-201 cardiac SPECT. *J. Nucl. Med.* 35: 60P.

Galatsanos NP, Katsaggelos AK (1992), Methods for choosing the regularization parameter and estimating the noise variance in image restoration and their relation. *IEEE Trans. Imag. Proc.* 1: 322 - 328.

Galt JR (1994), New instrumentation for cardiovascular nuclear medicine. *J. Nucl. Med.* 35: 20N - 22N.

Galt JR and Germano G (1995), Advances in Instrumentation for Cardiac SPECT, in *Cardiac SPECT Imaging*, DePuey EG, Berman DS and Garcia EV (editors), Raven Press, Ltd., New York.

Garcia EV, Van Train K, Maddahi J, Prigent F, Friedman J, Areeda J, Waxman A and Berman DS (1985), Quantification of rotational thallium-201 myocardial tomography. *J. Nucl. Med.* 26: 17 - 26.

Gibbons M (1963), Experimental Statistics, National Bureau of Standards Handbook 91, US Department of Commerce, Washington, DC.

Gibbons R, Verani M, Behrenbeck T, Pellikka P, O'Connor M, Mahmarian J, Chesebro J, and Wackers F (1989), Feasibility of tomographic ^{99m}Tc -hexakis-2-methoxy-2-methylpropyl-isonitrile imaging for the assessment of myocardial area at risk and the effect of treatment in acute myocardial infarction. *Circulation* 80: 1277 - 1286.

Gilland DR, Tsui BM, McCartney WH, Perry JR and Berg J (1988), Determination of the optimum filter function for SPECT imaging. *J. Nucl. Med.* 29: 643 - 650.

Glick SJ, DeVries DJ, Luo DS and King MA (1994b), Distance-dependent restoration filtering of dual photopeak window scatter compensated SPECT images. *IEEE Trans. Nucl. Sci.* 41: 2787 - 2792.

Glick SJ, King MA and Penney BC (1989), Characterization of the modulation transfer function of discrete filtered backprojection. *IEEE Trans. Med. Imag.* 8: 203 - 213.

Glick SJ, Penney BC and King MA (1991), Filtering of SPECT reconstructions made using Bellini's Attenuation correction method: A comparison of three pre-reconstruction filters and a post-reconstruction Wiener filter. *IEEE Trans. Nucl. Sci.* 38: 663 - 669.

Glick SJ, Penney BC, King MA and Byrne CL (1994a), Noniterative compensation for the distance-dependent detector response and photon attenuation in SPECT imaging. *IEEE Trans. Med. Imag.* 13: 363 - 374.

Gonzalez R and Wintz P (1977), Digital Image Processing. Addison-Wesley Publishing Company, Inc., MA.

Gullberg GT and Budinger TF (1981), The use of filtering methods to compensate for constant attenuation in single-photon emission computed tomography. *IEEE Trans. Biomed. Eng.* 28: 142 - 157.

Hademenos GJ, King MA, Ljungberg M, Zubal G and Harrell CR (1993), A scatter correction method for TI-201 images: A Monte Carlo investigation. *IEEE Trans. Nucl. Sci.* 40: 1179 - 1186.

Haynor DR, Kaplan MS, Miyaoka RS and Lewellen TK (1996), Multiwindow scatter correction techniques in single-photon imaging. *Med. Phys.* 22: 2015 - 2024, 1996.

Healy DM, Lu J and Weaver JB (1995), Two applications of wavelets and related techniques in medical imaging. *Annals Biomed. Eng.* 23: 637 - 665.

Heo J, Iskandrian B and Cave V (1992), Single photon emission computed tomographic teboroxime imaging with a preprocessing masking technique. *Am. Heart J.* 124: 1603 - 1608.

- Johnson LL (1991), Clinical experience with technetium-99m teboroxime. Sem. Nucl. Med. 21: 182 - 189.
- Johnson LL (1994), Myocardial perfusion imaging with technetium-99m teboroxime. J. Nucl. Med. 35: 689 - 692.
- Keyes WI (1976), A practical approach to transverse-section gamma-ray imaging. Brit. J. Radiol. 49: 62 - 70.
- King MA, Coleman M, Penney BC and Glick SJ (1991), Activity quantitation in SPECT: A study of prereconstruction Metz filtering and use of the scatter degradation factor. Med. Phys. 18: 184 - 189.
- King MA, Doherty PW, Schwinger RB, Jacobs DA, Kidder RE and Miller T (1983), Fast-count dependent digital filtering of nuclear medicine images: Concise communication. J. Nucl. Med. 24: 1039 - 1045.
- King MA, Glick SJ and BC Penney (1991), Activity quantitation in SPECT: A comparison of three attenuation correction methods in combination with pre-reconstruction restoration filtering. IEEE Trans. Nucl. Sci. 38: 755 - 760.
- King MA, Glick SJ, Penney BC, Schwinger RB and Doherty W (1987), Interactive visual optimization of SPECT prereconstruction filtering. J. Nucl. Med. 28: 1192 - 1198.
- King MA, Schwinger RB, Doherty PW and Penney BC (1984), Two-dimensional filtering of SPECT imaging using the Metz and Wiener filter. J. Nucl. Med. 25: 1234 - 1240.
- King MA, Schwinger RB and Penney BC (1986), Variation of the count-dependent Metz filter with imaging system modulation transfer function. Med. Phys. 13: 139 - 149.
- King MA, Tsui BM, Tin-Su P, Glick S, and Soares EJ (1996), Attenuation compensation for cardiac single-photon emission computed tomographic imaging: Part 2. Attenuation compensation algorithms. J. Nucl. Cardiol. 3: 55 - 63.
- King MA, Xia W, DeVries DJ, Pan TS, Villegas BJ, Tsui BW, Ljunberg MH and Morgan HI (1995), A Monte Carlo investigation of artifacts caused by the liver in perfusion imaging. J. Nucl. Med. 36: 29P.
- Laine A, Fan J and Yang W (1995), Wavelets for contrast enhancement of digital mammography. IEEE Eng. Med. Biol. 4: 536 - 550.
- Laine A, Schuler S, Fan J and Huda W (1994), Mammographic features enhancement by multiscale analysis. IEEE Trans. Med. Imag. 13: 725 - 740.
- Larsen SA (1980), Gamma camera emission tomography. Acta Radiologica [suppl] 363: 32 - 48.

- Leppo JA (1996), Comparison of pharmacologic stress agents. *J. Nucl. Cardiol.* 6: 522 - 526.
- Li J, Jaszczak R, Greer K, Gilliland D, DeLong D and Coleman E (1995), Evaluation of SPECT quantification of radiopharmaceutical distribution in canine myocardium. *J. Nucl. Med.* 36: 278 - 286.
- Liu L, Cullom SJ, White ML (1996), A modified Wiener filter method for nonstationary resolution recovery with scatter and iterative attenuation correction for cardiac SPECT. *J. Nucl. Med.* 37: 210P.
- Ljunghberg M, King MA, Pan TS, DeVries DJ and Strand SE (1994), Scatter and attenuation correction in SPECT cardiac imaging: A comparison using Monte Carlo simulated homogeneous data. *J. Nucl. Med.* 35: 189P.
- Maddahi J and Czernin J (1996), Absolute quantitation of myocardial blood flow: The technical and clinical prospects for single photon emission computed tomography. *J. Nucl. Cardiol.* 6: 560 - 565.
- Madsen MT, Park CH (1985), Enhancement of SPECT images by Fourier filtering the projection image set. *J. Nucl. Med.* 26: 395 - 402.
- Mahmorian JJ, Pratt CM, Nishimura S, Abreu A and Verani MS (1993), Quantitative adenosine 201Tl single-photon emission computed tomography for the early assessment of patients surviving acute myocardial infarction. *Circulation* 87: 1197 - 1210.
- Mallat SG (1989), Multifrequency channel decompositions of images and wavelet models. *IEEE Trans. Acoust. Speech Signal Process.* 37: 2091 - 2110.
- Manglos SH, Jaszczak RJ, Floyd CE, Hahn LJ, Greer KL and Coleman RE (1987), Nonisotropic attenuation in SPECT: Phantom tests of quantitative effects and compensation techniques. *J. Nucl. Med.* 28: 1584 - 1591.
- Manglos SH, Thomas FD and Hellwig BJ (1993), The effect of non-uniform attenuation compensation on myocardial SPECT defect analysis. *Phys. Med. Biol.* 38: 897 - 907.
- Maniawski PJ, Miller SD and Morgan HT (1996), Combined attenuation and scatter correction significantly reduces the effect of extracardiac activity on Tl-201 myocardial perfusion SPECT. *J. Nucl. Med.* 37: 214P.
- Matsunari I, Fujino S, Taki J, Senma J, Aoyama T, Wakasugi T, Hirai J, Saga T, Tonami N and Hisada K (1996a), Comparison of defect size between thallium-201 and technetium-99m tetrofosmin myocardial single-photon emission computed tomography in patients with single-vessel coronary artery disease. *Am. J. Cardiol.* 77: 350 - 354.

Matsunari I, Tanishina Y, Taki J, Ono K, Nishide H, Fujino S, Matoba M, Ichiyangagi K and Tonami N (1996b), Early and delayed technetium-99m-tetrofosmin myocardial SPECT compared in normal volunteers. *J. Nucl. Med.* 37: 1622 - 1626.

McCartney WH, Tsui BW, Adams KF, Lewis DP, Lalush DS, Bujenovic LS, LaCroix KJ, Johnston RE, Perry JR, Lonn AH, Maniam S and Culp R (1996), Clinical evaluation of attenuation and scatter compensation in Tl-201 SPECT. *J. Nucl. Med.* 37: 80P

Middleton GV & Williams JH (1993), Significant gastric reflux of technetium-99m-MIBI in SPECT myocardial imaging. *J. Nucl. Med.* 35: 619 - 620.

Nichols KJ & Galt JR (1995), Quality Control for SPECT Imaging, in *Cardiac SPECT Imaging*, DePuey EG, Berman DS and Garcia EV (editors), Raven Press, Ltd., New York.

Nuyts J, Bosmans H, and Suetens P (1993), Analytical model for Compton scatter in a homogeneously attenuating medium. *IEEE Trans. Med. Imag.* 12: 421 - 429.

Nuyts J, DuPont P, Van den Maegdenbergh V, Vleugels S, Suetens P and Mortelmans L (1995), A study of the liver-heart artifact in emission tomography. *J. Nucl. Med.* 36: 133 - 139.

O'Connor MK, Caiati C, Christian TF and Gibbons RJ (1995a), Effects of scatter correction on the measurement of infarct size from SPECT cardiac phantom studies. *J. Nucl. Med.* 36: 2080 - 2086.

O'Connor MK, Gibbons RJ, Juni JE, O'Keefe J and Ali A (1995b), Quantitative myocardial SPECT for infarct sizing: Feasibility of a multicenter trial evaluated using a cardiac phantom. *J. Nucl. Med.* 36: 1130 - 1136.

O'Connor MK, Hammel T, and Gibbons RJ (1990), In vitro validation of a simple tomographic technique for estimation of percentage myocardium at risk using methoxyisobutyl isonitrile technetium-99m (sestamibi). *Eur. J. Nucl. Med.* 17: 69 - 76.

Orlandi S (1996), Pharmacology of coronary vasodilation: A brief review. *J. Nucl. Cardiol.* 3: 27 - 30.

Penney BC, Glick SJ and King MA (1990), Relative importance of the error sources in Wiener restoration of scintigrams. *IEEE Trans. Med. Imag.* 9: 66 - 70.

Porenta G, Kuhle W, Sinha S, Krivokapich J, Czernin J, Gambhir SS, Phelps ME (1994), Parameter estimation of cardiac geometry by ECG-gated PET imaging: Validation using magnetic resonance imaging and echocardiography. *J. Nucl. Med.* 36: 1123 - 1129.

Qian W and Clarke LP (1996), A restoration algorithm for P-32 and Y-90 bremsstrahlung emission nuclear imaging: A wavelet-neural network approach. *Med. Phys.* 23: 1309 - 1323.

Ramachandrian GN and Lakshminarayan AV (1971), Three-dimensional reconstruction from radiographs and electron micrographs: Application of convolutions instead of Fourier transforms. *Proc. Natl. Acad. Sci.* 68: 2236 - 2240.

Rogers WL & Clinthorne NH (1987), Single Photon Computed Tomography (SPECT), in *Nuclear Medical Physics*, vol. III, Williams LE (editor), CRC Press Inc, Boca Raton Fl.

Sahiner B and Yagle AE (1995), Reconstruction from projections under time-frequency constraints. *IEEE Trans. Med. Imag.* 14: 193 - 204.

Segal GM & Davis MJ (1989), Prone versus supine thallium myocardial SPECT: A method to decrease artifactual inferior wall defects. *J. Nucl. Med.* 30: 548 - 555.

Shepp LA and Vardi Y (1982), Maximum likelihood reconstruction for emission tomography. *IEEE Trans. Med. Imag.* 1: 113 - 122.

Shnier D, Saffer JR and Araujo LI (1997), Attenuation corrected SPECT imaging improves detection of small myocardial defects in a cardiac phantom. *J. Nucl. Med.* 38: 64P.

Smith MF, Jaszcak RJ and Coleman RE (1997), Use of an analytic model of pinhole aperture penetration for resolution recovery in I-131 pinhole SPECT. *J. Nucl. Med.* 38: 58P.

Tanaka E, Toyama H and Murayama H (1984), Convolutional image reconstruction for quantitative single photon emission computed tomography. *Phys. Med. Biol.* 29: 1489 - 1500.

Tretiak O & Metz C (1980), The exponential Radon transform. *SIAM J. Appl. Math.* 39: 341 - 354.

Tsui BW, Frey EC, Zhao X, Lalush DS, Jonhston RE and McCartney WH (1994b), The importance and implementation of accurate 3D compensation methods for quantitative SPECT. *Phys. Med. Biol.* 39: 509 - 530.

Tsui BW, Gullberg GT, Edgerton ER, Ballard JG, Perry JR, McCartney WH and Berg J (1989), Correction of nonuniform attenuation in cardiac SPECT imaging. *J. Nucl. Med.* 30: 497 - 507.

Tsui BW, Zhao X, Frey EC and McCartney WH (1994a), Quantitative single-photon emission computed tomography: Basis and clinical considerations. *Sem. Nucl. Med.* 24: 38 - 65.

- Van Train KF, Garcia EV, Maddahi J, Areeda J, Cooke CD, Kiat H, Silagan G, Folks R, Friedman J, Matzer L, Germano G, Bateman T, Ziffer J, DePuey EG, Fink-Bennet D, Cloninger K and Berman DS (1994), Multicenter trial validation for quantitative analysis of same-day rest-stress technetium-99m-sestamibi myocardial tomograms. *J. Nucl. Med.* 35: 609 - 618.
- Varga J, Bettinardi V, Gilardi MC, Ridell C, Castiglioni I, Rizzo G and Fazio F (1997), Evaluation of pre- and post-reconstruction count-dependent Metz filters for brain PET studies. *Med. Phys.* 24: 1431 - 1440.
- Verani M (1996), Risk assessment after myocardial infarction: Have the rules changed with thrombolytic therapy? *J. Nucl. Cardiol.* 3: 50 - 59.
- Wallis J, Miller TR and Koppel P (1995), Attenuation correction in cardiac SPECT without a transmission measurement. *J. Nucl. Med.* 36: 506 - 512.
- Wang G, Zhang J and Pan GW (1995), Solution of inverse problems in image processing by wavelet expansion. *IEEE Trans. Ima. Proc.* 4: 579 - 593.
- Welch A, Smith AM and Gullberg GT (1995), An investigation of the effect of finite system resolution and photon noise on the bias and precision of dynamic cardiac SPECT parameters. *Med. Phys.* 22: 1829 - 1836.
- Wornell G (1996), Signal Processing with Fractals: A Wavelet-based Approach. Prentice Hall, Upper Saddle River, NJ.
- Yanch JC, Irvine AT, Webb S, Flower MA (1988), Deconvolution of emission tomographic data: A clinical evaluation. *Br. J. Radiol.* 61: 221 - 225.
- Zanzonico P, Bigler RE, Sgouros G and Strauss A (1989), Quantitative SPECT in radiation dosimetry. *Sem. Nucl. Med.* 19: 47 - 61.
- Zeng L, Christian PE, Gullberg GR and Morgan HT (1995), A new window function that eliminates the artifactual decreased myocardial wall uptake. *J. Nucl. Med.* 36: 30P
- Zwillinger D (1996), CRC Standard Mathematical Tables and Formulae. CRC Press, 30th edition, Boca Raton.

BIOGRAPHICAL SKETCH

Juan M. Franquiz received his B.S. degree in physics from the University of Havana, Cuba. After graduation, he was awarded a two-year fellowship from the International Atomic Energy Agency for training in Medical Physics at the Institute of Clinical and Experimental Medicine in Prague, Czechoslovakia. From 1984 to 1991, he worked as a nuclear medicine physicist at the Institute of Cardiology in Havana, Cuba, and as instructor of applied physics at the University of Havana. In 1992 he emigrated to the United States and one year later became a full-time graduate student at the University of Florida.

I certify that I have read this study and that in my opinion it conforms to acceptable standards of scholarly presentation and is fully adequate, in scope and quality, as a dissertation for the degree of Doctor of Philosophy.

Shailendra Shukla
Shailendra Shukla, Chair
Research Associate Professor of Nuclear
and Radiological Engineering

I certify that I have read this study and that in my opinion it conforms to acceptable standards of scholarly presentation and is fully adequate, in scope and quality, as a dissertation for the degree of Doctor of Philosophy.

Wesley Boldn
Wesley Boldn
Associate Professor of Nuclear and
Radiological Engineering

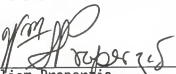
I certify that I have read this study and that in my opinion it conforms to acceptable standards of scholarly presentation and is fully adequate, in scope and quality, as a dissertation for the degree of Doctor of Philosophy.

Walter Drane
Walter Drane
Professor of Radiology

I certify that I have read this study and that in my opinion it conforms to acceptable standards of scholarly presentation and is fully adequate, in scope and quality, as a dissertation for the degree of Doctor of Philosophy.

Janice C Honeyman
Janice Honeyman
Associate Professor of Computer and
Information Sciences

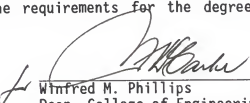
I certify that I have read this study and that in my opinion it conforms to acceptable standards of scholarly presentation and is fully adequate, in scope and quality, as a dissertation for the degree of Doctor of Philosophy.



William Properzio
Associate Professor of Nuclear and
Radiological Engineering

This dissertation was submitted to the Graduate Faculty of the College of Engineering and to the Graduate School and was accepted as partial fulfillment of the requirements for the degree of Doctor of Philosophy.

December 1997



Winfred M. Phillips
Dean, College of Engineering

Karen A. Holbrook
Dean, Graduate School